research report

Analytical Study on Rotational Restraint of Sheathing

RESEARCH REPORT RP08-2

2008

American Iron and Steel Institute

Steel Framing Alliance™

Steel. The Better Builder.

DISCLAIMER

The material contained herein has been developed by researchers based on their research findings and is for general information only. The information in it should not be used without first securing competent advice with respect to its suitability for any given application. The publication of the information is not intended as a representation or warranty on the part of the American Iron and Steel Institute, Steel Framing Alliance, or of any other person named herein, that the information is suitable for any general or particular use or of freedom from infringement of any patent or patents. Anyone making use of the information assumes all liability arising from such use.

PREFACE

This report is a supplement to the July 2007 report on *Experiments on Rotational Restraint of Sheathing* by Schafer, Sangree and Guan. The work reported herein was completed at The Johns Hopkins University. It employs finite element models of the previously conducted rotational restraint tests, and includes a small number of additional physical tests to investigate the role of fastener spacing in further detail.

It is anticipated that the AISI Committee on Framing Standards will consider the results of this study in the development of future standards and the Cold-Formed Steel Engineers Institute in the development of design aids. The American Iron and Steel Institute and Steel Framing Alliance wish to express their appreciation to the researchers and project sponsors for this report.

ANALYTICAL STUDY ON ROTATIONAL RESTRAINT OF SHEATHING

Guan, Y.
(Schafer, B.W. advisor)

FINAL REPORT

PROVIDED TO:

American Iron and Steel Institute – Committee on Framing Standards

July 2008

TABLE OF CONTENTS:

ABSTRACT:

Building upon a previous set of experiments performed to determine connection rotational restraint provided by sheathing in cold-formed steel floor joists, this study investigates the reliability of reported connection rotational stiffness values. Key assumptions made by the experimental researchers during testing and post processing of experimental data are explored. Effects observed but not measured during testing, including fastener pullout failure and construction flaws, are also examined.

By modeling the experimental setup in Mastan and ABAQUS, frame and shell finite element analysis are used to examine and determine the validity and limitations of experimental assumptions made to approximate complex nonlinear behavior. In conjunction with additional experimentation, these methods also provide clarification of local deformations leading to quantification of failure mode forces and construction flaw effects on connection rotational stiffness.

Findings ultimately support the reliability of reported values with high agreement between experimental assumptions and behavior predicted by structural mechanics. Results also provide new data on allowable fastener pullout deformation along with preliminaries for a new method to estimate fastener pullout failure force based on moment. Finally, observed construction flaws are shown to have a small impact on average connection rotational stiffness values.

1 INTRODUCTION

1.1 Background of experiments and analysis

Cold-formed steel joists, when employed in sub-flooring, are susceptible to a distortional buckling failure mode. This distinct failure mode is characterized by rotation of the joist compression flange at the flange web interface and local web bending. Restraint against this distortional buckling rotational deformation is typically provided by connecting joists to sheathing using fasteners. This rotational restraint, k_ϕ, is necessary when determining joist capacity in sub-flooring design. With a lack of existing studies on k_ϕ for cold-formed steel framing an initial set of experiments was carried out and presented in an initial AISI report (Schafer 2007).

Within these tests, cantilevered sub-flooring models were constructed and subject to deformation consistent with distortional buckling with connection rotational stiffness values notated as $k_{\phi c2}$ measured and reported for each test. The initial experimental study focused on measuring four main rotational stiffness values. These four rotational stiffness values included $k_{\phi 2}$ or total rotational stiffness measured as a function of sheathing, joist, and fastener rotation. Sheathing rotational stiffness or $k_{\phi w}$ was measured as a function of sheathing rotation. Connection rotational stiffness reported as $k_{\phi c2}$ was measured as a function of fastener and joist rotation or joist bending effects. An attempt was also made to calculate pure connection rotational stiffness, $k_{\phi c}$, rotational stiffness measured as a function of fastener rotation only. Key future work suggested by the initial report's findings is carried out in this study by modeling and additional testing for validation and exploration of the report's various k_ϕ values for use in design.

By testing assumptions made in extracting $k_{\phi c2}$ values from the original report, the reliability of reported values and understanding of failure modes observed, such as fastener pull-out failure, is explored within this study. These assumptions dealt with the impact of P-delta effects on the measured applied moment, joist bending effects on $k_{\phi c2}$, and small angle approximations used for $k_{\phi w}$. Initial experimental trends of $k_{\phi c2}$ values due to fastener spacing from the report are also assessed in this study, as it was found that tighter fastener spacing seemed to have a beneficial impact on $k_{\phi c2}$. Validation of the assumptions using existing experimental measurements was not possible during the initial set of experiments due to difficulty in rotational decomposition as discussed in the report. In particular, as experimentally measured $k_{\phi c2}$ values included joist bending and fastener rotations, an effort to remove joist bending effects within this study potentially leads to more efficient and useful $k_{\phi c}$, rotational stiffness values due to the fastener connection alone. With modeling, a new computational mechanics approach is provided within this study for validating these assumptions and for greater understanding of $k_{\phi c2}$ complementing the existing experimental approach.

An initial approach is taken to model the experiments with frame analysis (Mastan) and truss elements. Through these truss elements, experimentally observed moment couple effects resulting from fastener pullout and joist bearing are represented. Using second order analysis with the model subject to equivalent experimental displacements, decomposition of the rotations due to sheathing, fastener, and joist bending, is conducted resulting in an assessment of joist bending significance. Mastan frame analysis is also used to quantify P-Δ effects through subjecting cantilevered sheathing models to an equivalent experimental moment in one case while applying an equivalent experimental axial force and moment in another case. By comparing the resulting moments from the two cases, P-delta effects on moment as defined in Schafer's report are found. Small angle approximations used in the original report (Schafer 2007) are also explored using the Mastan models through comparing

calculated rotations found using the report's small angle elastic beam mechanics expressions and nodal rotations yielded by Mastan from a second order analysis.

ABAQUS modeling with shell elements is also employed to assess fastener spacing along with out of plane interaction and deformation effects on $k_{\phi c2}$. The experimental setup is modeled in ABAQUS using S9R5 shell elements for the sheathing and joist with boundary conditions representative of the cantilevered setup. Joist bearing is modeled with frictionless contact defined in the model between the sheathing and joist surfaces. Fasteners are modeled as connected spring elements with stiffness defined in all six directions. Through subjecting the ABAQUS models to equivalent experimental displacements, model $k_{\phi c}$ values are compared to experimentally reported $k_{\phi c2}$ values for model validation within the linear range. This allows for accurate rotational decomposition with quantification of joist bending effects for each experimental test. Fastener spacing effects are also modeled in ABAQUS through varying fastener spacing from 3 inches o.c. to 24 inches o.c. between models with comparisons of resulting ABAQUS and experimental connection rotational stiffness values made after rotational decomposition for model validation.

Additional experimental testing is conducted with OSB sheathing and fastener spacing at 3, 6, 12, and 24 inches o.c. to verify if any beneficial effects of tighter fastener spacing on $k_{\phi c2}$ exist through comparison of measured $k_{\phi c2}$ values between tests. During testing, axial pull out failure and sheathing fracture failure were both observed leading to additional modeling analysis. Recognizing the importance of these failure modes in design, attempts to quantify fastener axial pullout and sheathing fracture force were made by varying axial stiffness in models to yield model $k_{\phi c}$ values equivalent to new experimental $k_{\phi c2}$ values. Within Mastan, this occurred by varying the area of the fastener truss element resulting in differences in axial stiffness based on beam mechanics. In ABAQUS, this was carried out by varying the axial stiffness of the connector spring elements and measuring the resulting rotational stiffness until convergence to experimental connection stiffness response was achieved.

As noted in the original report and encountered again during additional testing, the impact of construction flaws on $k_{\phi c2}$ has to be considered. A parameter study on the two most commonly found construction flaws, fastener offset and overdriven fasteners, is conducted in this report. From experimental measurements, random variable distributions are created for both flaws and implemented in ABAQUS models. A Monte Carlo approach is taken with 100 ABAQUS models created with construction flaws generated as part of the mesh, with the resulting $k_{\phi c2}$ distribution calculated and reported. A less computationally intensive 2k+1 point estimate approach with 31 ABAQUS models generated with construction flaws is also done with the resulting $k_{\phi c2}$ distribution also reported and compared to the Monte Carlo results. Using the 2k+1 results, a nonlinear closed form expression for $k_{\phi c2}$ is also generated using taylor series expansion.

2 FASTENER MODELING

In modeling the cantilevered sub-flooring experimental setup carried out in the first AISI report in Mastan and ABAQUS, various approaches were taken and refined to effectively capture the localized deformation effects observed. In Mastan, the fastener was initially modeled as a beam element but was eventually modeled as a truss element to reflect observed moment couple effects. Within ABAQUS, a similar initial approach was also taken with a series of spring elements that collectively was analogous to a beam element. Refinement of this approach came in the form of contact modeling resulting in better representation of fastener pullout effects.

2.1 Mastan modeling of experimental testing

2.1.1 Connector modeled as beam element

The fastener was initially modeled as a beam with fixed connections as shown in Figure 1 for a 362S162-68 joist, with shear and moment carried by the fastener during loading. Additionally, the joist was modeled using nominal cross sectional dimensions with a material modulus of elasticity equal to 29500 ksi while the sheathing was modeled using experimental dimensions with either 24 or 12 in. cantilevered lengths and a material modulus of elasticity back calculated from experimental $k_{\phi w}$ measurements. All joists experimentally tested which included 362S162-33, 362S162-68, 800S200-54, 800S200-97, 1200S200-54, and 1200S200-97 were modeled with either OSB or plywood sheathing based on experiments using fixed boundary conditions reflecting the cantilevered setup.

By varying the moment of inertia and consequently the bending stiffness of the beam (i.e., the beam which is modeling the fastener), it was possible to explore effects on joist bending and rotational stiffness. This was done through measuring resulting deformation displacement after subjecting the joist's right flange to six inches of vertical displacement, consistent with the experimental procedure. While the model is also ostensibly similar in appearance to the experimental setup shown in the original report (Schafer 2007), the model falls short of representing fastener pullout and joist bearing moment couple effects.

In assessing rotational stiffness response within the Mastan model using second order elastic analysis, there was no quantifiable change in rotation as a function of varying the beam/fastener area and the beam/fastener axial stiffness, as shown in Figure 2 for an example in which only measurement of the sheathing response occurred. This response was consistent across all joists modeled. In short, there is no axial force modeled within the beam suggesting a lack of joist bearing and an absence of the observed moment couple response. This refutes the usefulness of using a beam approach towards modeling the fastener as the model cannot be accurately used to decompose moment couple effects into corresponding axial stiffness and axial pullout forces. Ultimately, this shortcoming leads to a truss based approach towards modeling the experiment in Mastan to include present axial forces.

Figure 1 Mastan model with fastener beam element

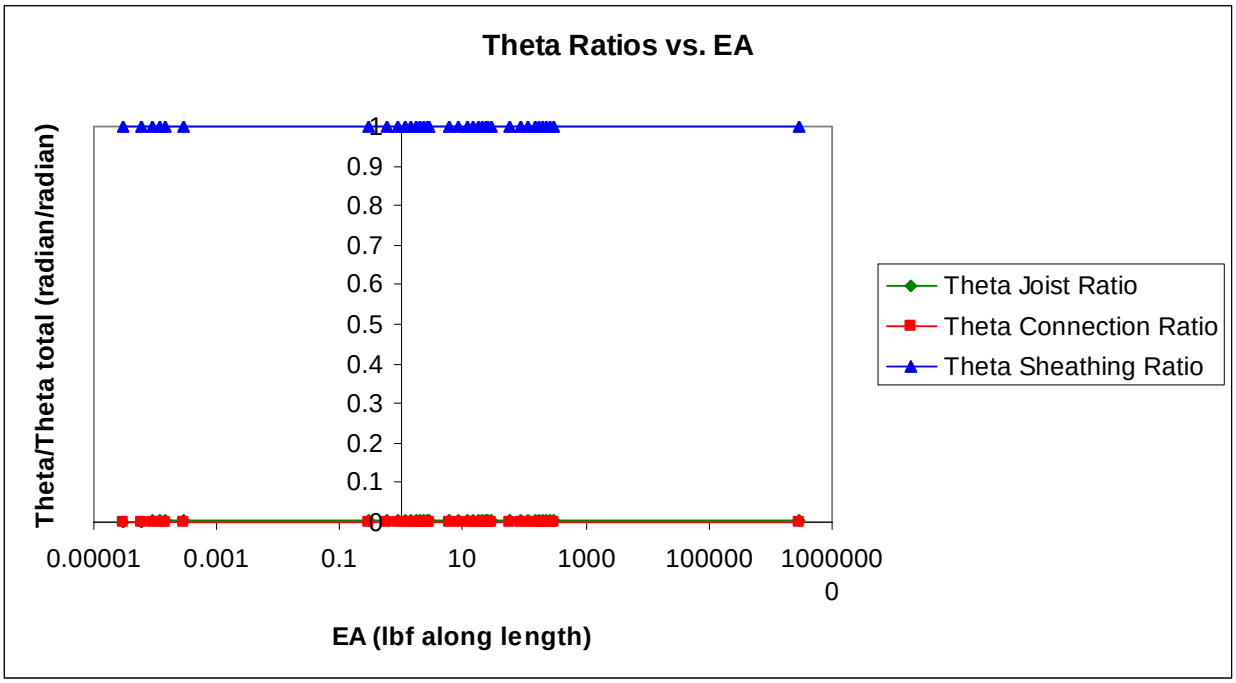

Figure 2 Plot of Mastan rotation outputs as a function of axial stiffness for a fastener modeled as beam approach

2.1.2 Connector and joist bearing modeled using trusses

The results of section 2.1.1 necessitated a different approach towards modeling the experiment resulting in the modified approach using truss elements in Mastan as depicted in Figure 3 with a close up shown in Figure 4 using the same 362S162-68 joist. The model consists of three pin connected truss elements which carry axial forces. The top horizontal truss element or element 1 in Figure 4 is the fastener which experiences axial force consistent with axial pull out during deformation. The diagonal truss element or element 2 in Figure 4 is responsible for carrying shear axial forces experienced by the fastener during loading. The bottom truss element which connects the sheathing to the flange web intersection of the joist or element 3 in Figure 4 is the joist bearing component of the system and contains high axial stiffness to effectively model the rigid joist bearing effects experienced by the setup during deformation. The model assumes joist bearing effects are present from initial deformation onward which is consistent with experimental observations of joist bearing onset soon after loading.

With the moment couple effect in place, there is now a response in rotational stiffness due to changing the axial stiffness of the fastener element through varying the area of element 1 in Figure 4, as shown in Figure 5 with sheathing, fastener, and joist bending rotational ratios plotted as a function of fastener axial stiffness. By modeling the experiment using this approach in Mastan, it becomes possible to decompose the local rotations resulting in plots such as Figure 5.

Three key nodes in Mastan shown in Figure 4 govern these rotations. Sheathing rotation is taken from the sheathing node (of Figure 4). Connector rotation is taken as the difference in rotations between the Connector and Sheathing nodes of the fastener element. Finally, joist rotation is taken as the difference between rotation at the Total Rotation node and the Connector node. Using these rotational decompositions as a function of fastener axial stiffness within this model allows for a more accurate assessment of joist bending effect significance and the relationship between fastener axial forces and fastener rotational stiffness as detailed in sections 3.3 and 4.1.1 respectively.

Figure 3 Mastan model of fastener and joist bearing using trusses

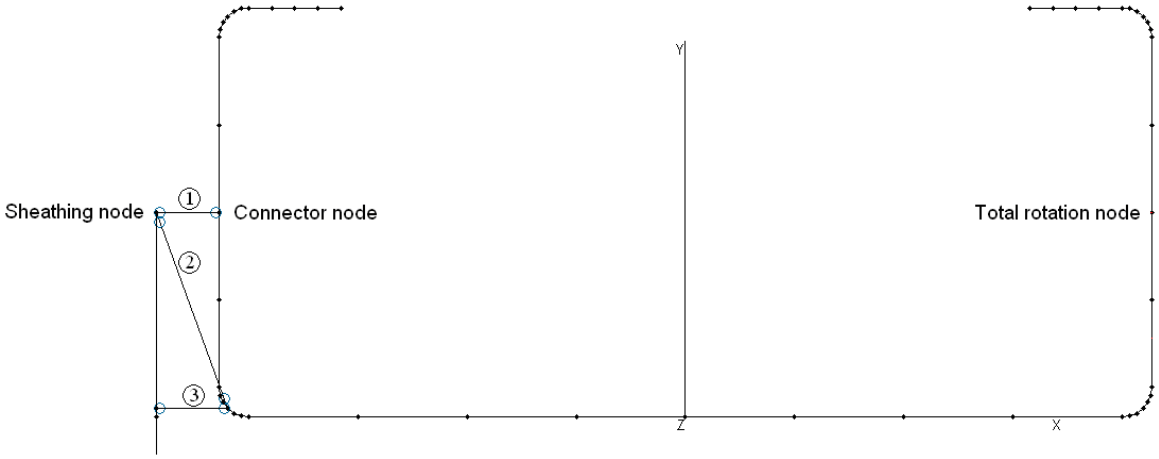

Figure 4 Close up of truss system and Mastan nodes used for rotational decomposition

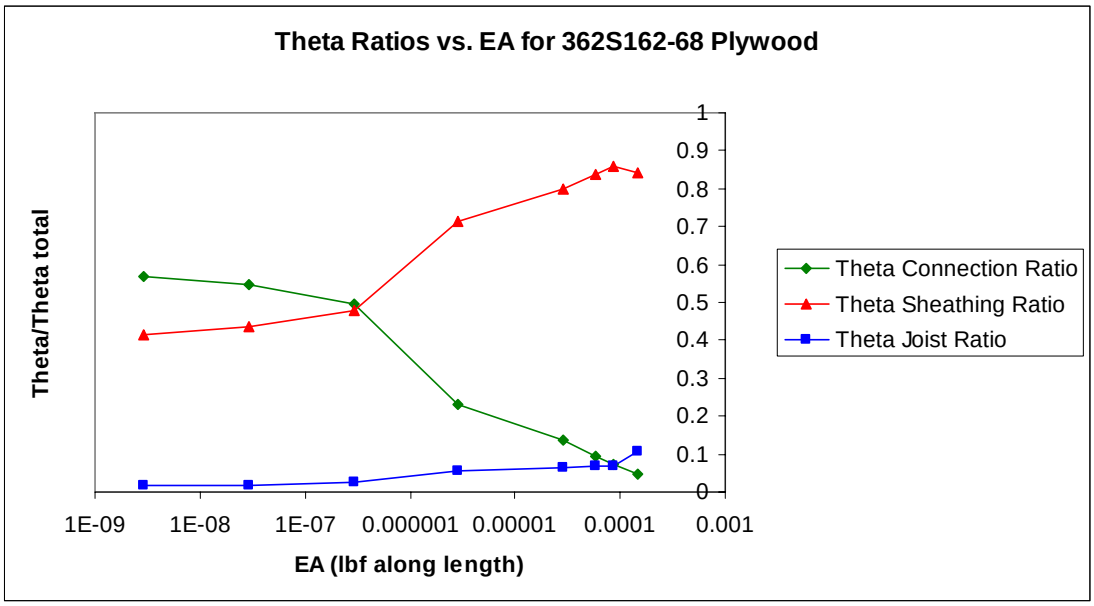

Figure 5 Mastan output rotations for truss model as a function of axial stiffness

From the exploration of fastener axial stiffness impact on rotational decomposition shown in Figure 5, total rotation is comprised mainly of connection rotation and sheathing rotation when the fastener is considered flexible with low axial stiffness,. However, it is interesting to note the plot also indicates the existence of joist bending that cannot be removed as there is still some joist bending contribution even when the fastener is flexible. When fastener axial stiffness is increased resulting in greater fastener rigidity, joist bending and sheathing components of total rotation are amplified due to fastener rotation being minimized. Even with artificially high axial stiffness however, the plot suggests the fastener cannot be made perfectly rigid as residual fastener rotation contribution towards total rotation still exists. Plots similar to Figure 5 for each joist and sheathing combination are shown and explored further in section 3.3.

2.2 ABAQUS modeling of experimental testing

2.2.1 Contact modeling and spring elements as fasteners

S9R5 shell elements adherent to a maximum 8 to 1 aspect ratio are used to model the joist and sheathing from the experimental setup, as shown in Figure 6. The fasteners are modeled using Spring2 elements as depicted in Figure 7 with stiffness defined in six directions for each fastener according to section 2.2.2 given below.

The key component within this model, similar to Mastan, is the axial stiffness of the fastener springs. It was found initially that modeling the fastener as a series of springs akin to the single beam approach in Mastan did not engage any axial forces in the system rendering the axial springs useless. It was also found that without a limit on joist bearing, the joist would bear through the sheathing giving inaccurate model deformation displacements as shown in Figure 8.

Instead of using the truss approach outlined in section 2.1.2 to include joist bearing, a similar but more accurate approach was taken with the inclusion of contact modeling. As per the initial report (Schafer 2007), a better approximation of observed effects would be to model the fasteners as springs and the joist bearing effects as a roller against the sheathing. Contact was therefore defined with the joist and sheathing as two distinct surfaces. Interaction between the two surfaces was limited to frictionless sliding and joist bearing initiation dependent on surface penetration by the joist into the sheathing as shown in Figure 9. It was apparent that moment couple effects were being modeled as subsequent changes to fastener axial stiffness had a direct effect on connection rotation.

Using this ABAQUS model and nonlinear elastic deformation analysis (second order analysis), it becomes possible to decompose rotations, quantify joist bending effects, and determine accurate axial forces inherent in each fastener, all in relation to fastener spacing in order to model individual experimental tests. These approaches are detailed in sections 3.3 and 4.1.2 respectively.

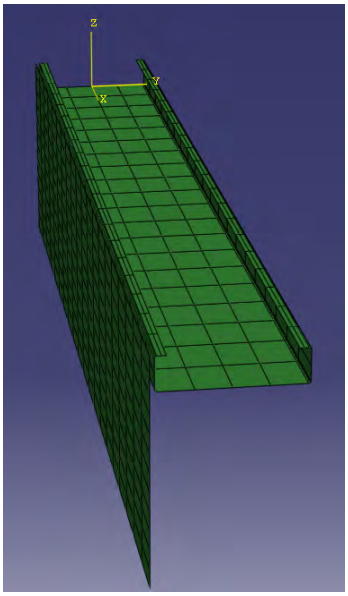

Figure 6 ABAQUS model of experiment using SR95 shells

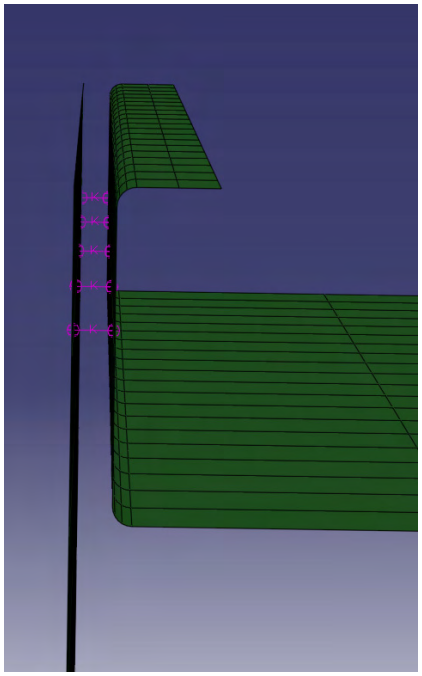

Figure 7 ABAQUS Spring2 elements used to model connection fasteners

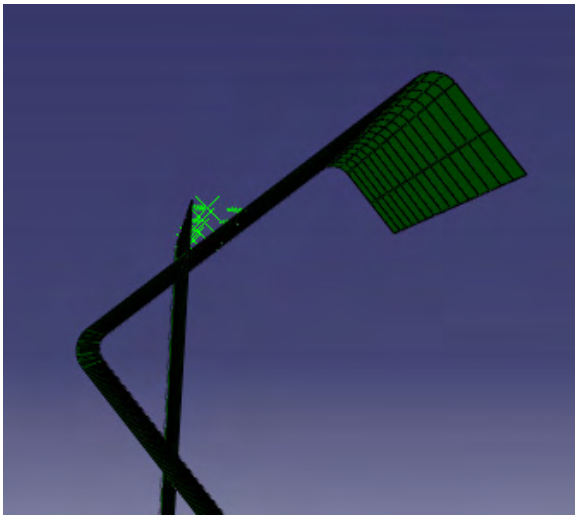

Figure 8 ABAQUS Joist Bearing Before Contact Modeling

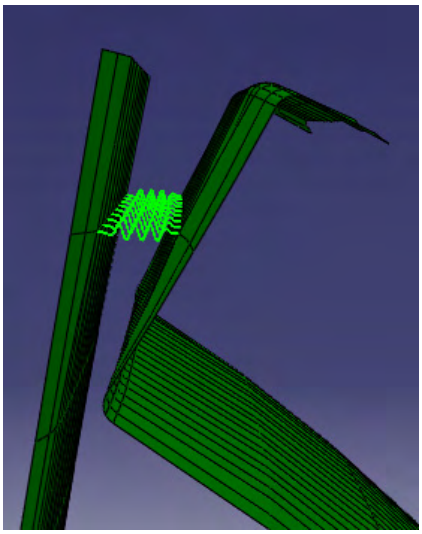

Figure 9 ABAQUS Joist Bearing After Contact Modeling

2.2.2 Fastener Spring Stiffness Definitions

The axial and rotational springs used to model the fastener behavior in ABAQUS are defined in six directions. Three local axes govern the axial spring inputs with the y axis along the length of the fastener accounting for fastener axial deformation, a transverse z axis governing fastener shear deformation, and an out of plane x axis allowing for lateral out of plane fastener deformation as shown in Figure 10. The three corresponding rotational axes include torsion with rotation around the local y axis, out of plane bending or rotation around the z axis, and in plane bending or rotation around the x axis.

Axial and rotational spring stiffness input values were chosen for consistency with experimental observations and previously derived relationships. As there was no out of plane bending around the local z axis resulting in lateral displacement of the fastener along the x axis observed during testing, out of plane axial and rotational stiffness in ABAQUS were made artificially rigid. Similarly, there was no torsional deformation resulting in fastener twisting around the local y axis witnessed leading to the torsional spring rotational stiffness also made artificially rigid.

While there was also no fastener shear deformation along the local z axis observed, fastener shear stiffness input was believed to be governed by fastener block shear and calculated as EA/L with A and L as the block shear fracture dimensions of sheathing above each fastener. These inputs result in the removal of both unreasonable rotational contributions in the out of plane and torsional directions, and deformation displacement contributions in the lateral out of plane and shear directions inconsistent with experimental observations.

As axial pullout failure was observed in some tests and in plane system rotation observed in all tests, fastener axial spring stiffness input in the y direction and fastener in plane rotational spring stiffness input around the local x axis cannot be taken as rigid. Rotational spring stiffness inputs for each fastener were therefore calculated as the product of experimentally measured total rotational stiffness, $k_{\phi 2}$, and tributary width between fasteners. The calculation of fastener axial spring stiffness using experimental measurements is explained in section 4.1.2. Ultimately, axial spring stiffness has the greatest impact on local deformations and system behavior as it governs the important moment couple effect.

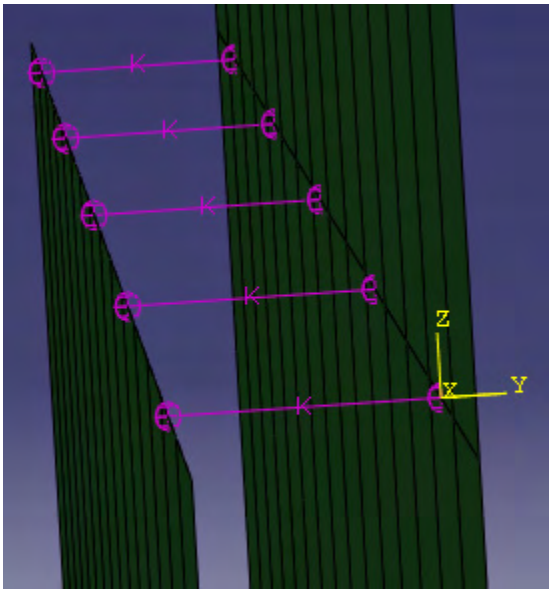

Figure 10 Local Axes Referenced At Fastener

2.2.3 Validity of ABAQUS models

Upon first glance, comparative resulting plots obtained from ABAQUS such as Figure 11, which include ABAQUS and experimental results for a 800S200-54 joist with 3 inch fastener spacing, indicate strong deviation from experimental results. However, it is important to realize that total rotation within each ABAQUS model contains excess model joist bending effects in addition to actual experimental joist bending effects resulting in this discrepancy. Model axial stiffness inputs as explained in section 4.1.2 are based upon experimental $k_{\phi c2}$ values, which include experimental joist bending effects and fastener rotation. Isolated ABAQUS fastener rotation and not total rotation should therefore capture only experimental joist bending and fastener rotation effects. Proper validation of the ABAQUS models occurs when ABAQUS $k_{\phi c}$ values are equivalent to experimental $k_{\phi c2}$ values as $k_{\phi c}$ in ABAQUS effectively excludes model joist bending effects.

Assessing ABAQUS $k_{\phi c}$ with removal of ABAQUS joist bending effects is done by running nonlinear elastic analysis in ABAQUS with a high model joist modulus of elasticity value resulting in strong joist rigidity, high bending stiffness, and isolation of connection and sheathing response. As shown in Figure 12, there is strong agreement between ABAQUS and experimental output within the linear region when ABAQUS joist bending effects are removed. Consistent with analysis methods from the original report used to extract predicted rotational stiffness values, ABAQUS $k_{\phi c}$ and $k_{\phi w}$ are close in magnitude to experimental $k_{\phi c2}$ and $k_{\phi w}$ values across all models. This highlights the significance of joist bending effects and the importance of its quantification in isolating ABAQUS $k_{\phi c}$ and eventually experimental $k_{\phi c}$ values. Further exploration of these relationships along with plots like Figure 12 for all additional experiments modeled is presented in section 5.2.

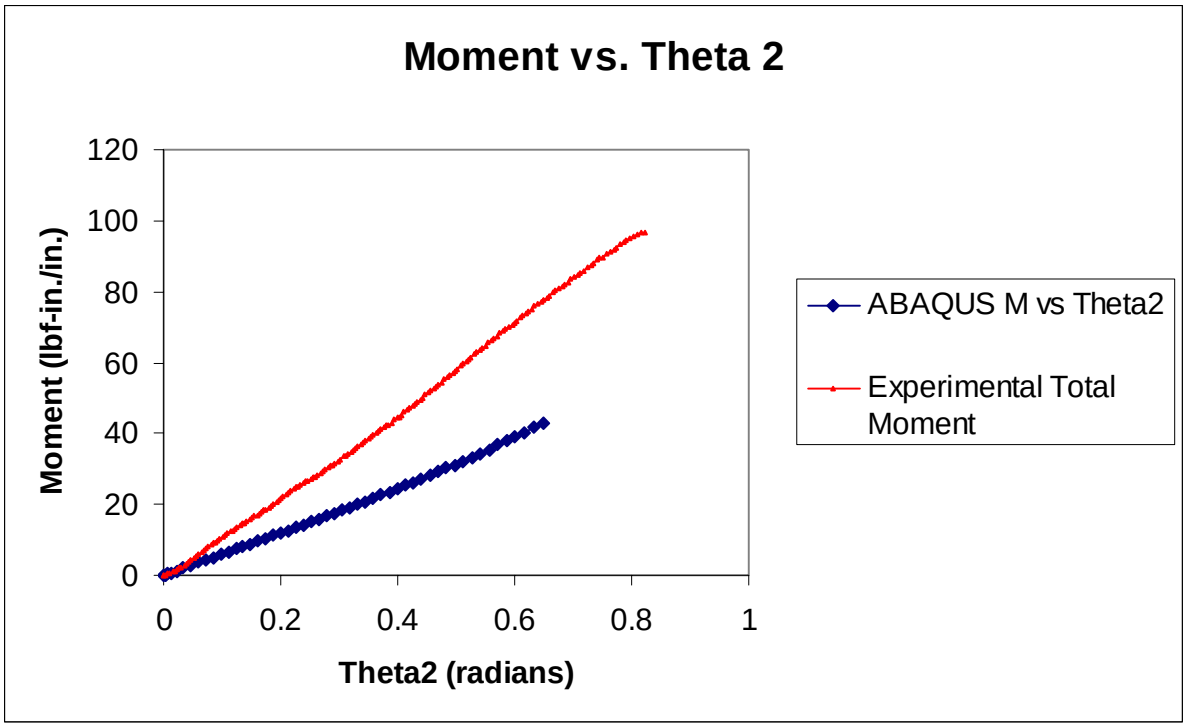

Figure 11 Plot of ABAQUS output vs. Experimental output

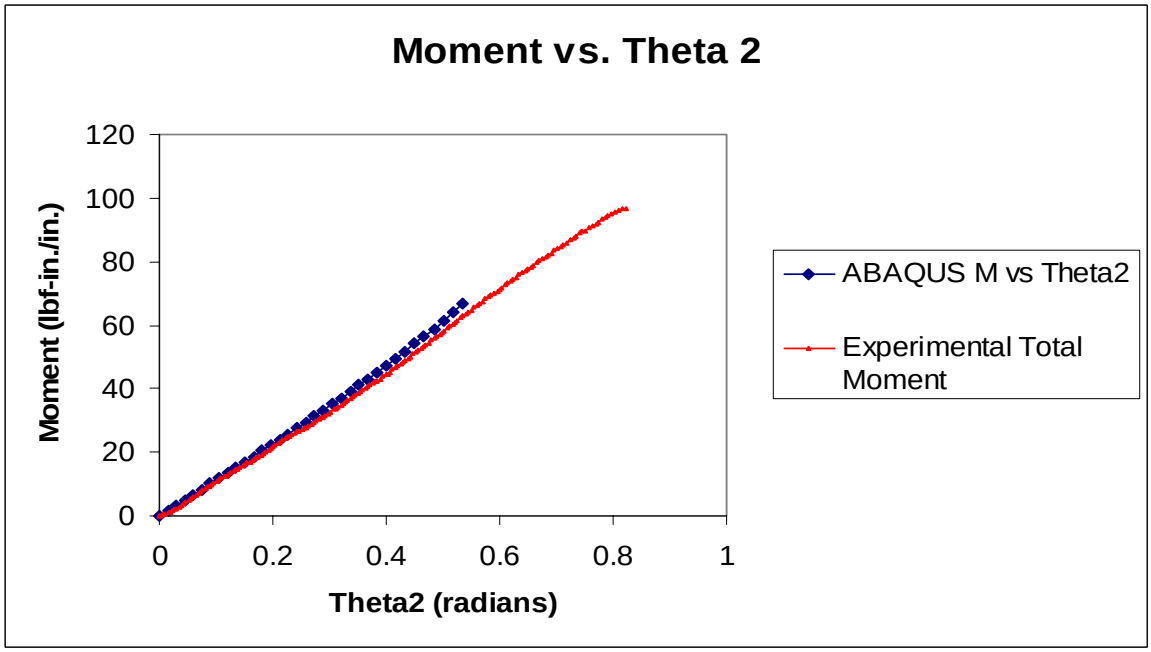

Figure 12 Plot of ABAQUS output vs. Experimental output with Rigid Joist

3 STUDY OF EXPERIMENTAL ASSUMPTIONS

With the experimental setup depicted in Figure 13 from the initial AISI report (Schafer 2007), key assumptions and observations were noted to facilitate extraction of rotational stiffness values using experimental load and displacement measurements resulting in summary plots such as Figure 14 from the same report.

In converting plots of vertical load measured by the load cell, P, vs. vertical deflection, Δ_v to plots of Moment vs. θ, as shown in Figure 14, moment per unit width at the connection, M, for simplicity was approximated as $M=(P/w)h_o$. With a constant moment arm of h_o. This approximation assumes nonlinear P-Δ effects are not significant, which is explored in section 3.2. Secondly, using beam mechanics and relating sheathing bending stiffness to sheathing lateral deflection, an approximation of sheathing rotation, $\theta_w = 2\Delta_h / L$, is used to calculate sheathing rotational stiffness, $k_{\phi w}$.

The validity of this sheathing rotation expression in relation to plywood and OSB sheathing is explored through comparison to modeled sheathing deformation rotations in section 3.1. Finally, an attempt in the original report was made to isolate and remove joist bending effects through approximating the joist deflection as cantilevered web deflection, $\Delta_s \approx Ph_o^3/3E_sI_s$, and removing this term from total rotation resulting in $\theta_1 = \tan^{-1}\left((\Delta_v - \Delta_s)/h_o\right)$, a quantity equivalent to $\theta_w+\theta_c$. Based on experimental observations and analysis of assumptions used in this derivation of joist bending removal however, it was suggested in the original report that joist bending effects may be less significant than quantified due to torsional resistance and minor axis bending. An assessment of this assumption with greater exploration of joist bending decomposition and quantification is made in section 3.3.

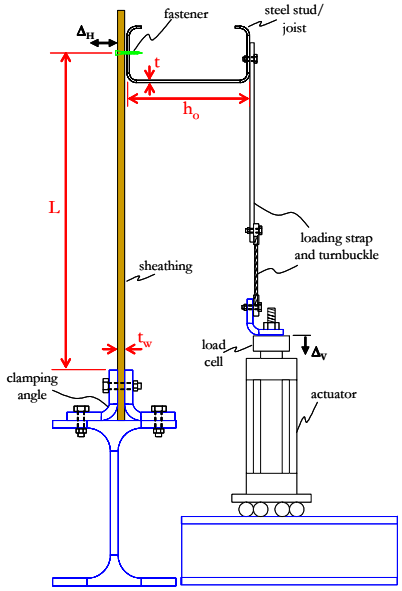

Figure 13-Experimental Setup from Initial AISI Report
Source: Experiments on Rotational Restraint of Sheathing, 2007

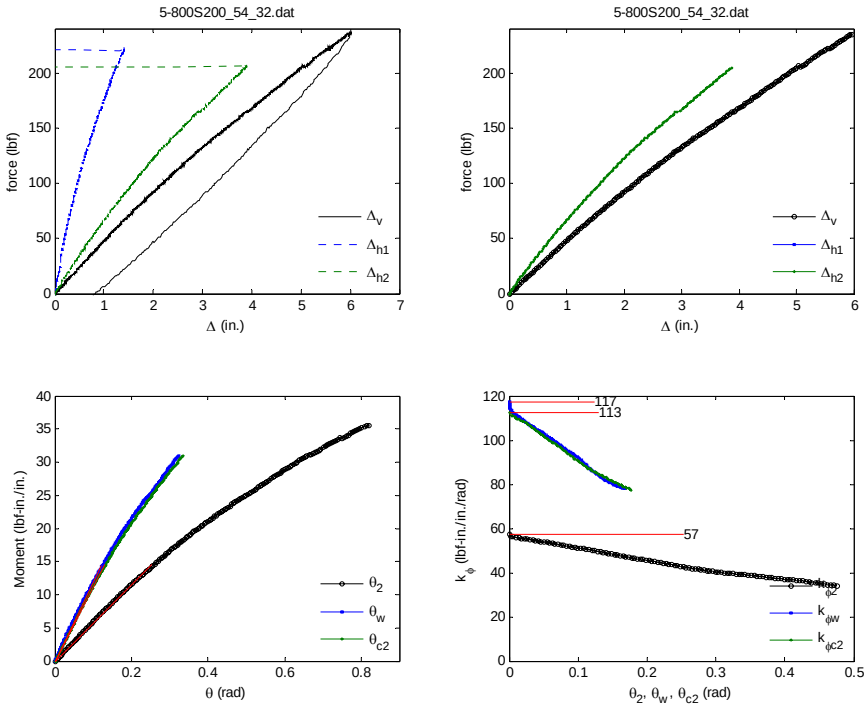

Figure 14-Plots used to calculate rotational stiffness values
Source: Experiments on Rotational Restraint of Sheathing, 2007

3.1 Large angle and small angle effects

By using the analytical model shown in Figure 15 from the original report and using elastic beam theory, sheathing bending stiffness, $EI_w/L = M/\theta_w$, can be related to sheathing lateral deflection, $\Delta_h = ML^2/2EI_w$, to arrive at an expression for sheathing rotation. This approximate expression for sheathing rotation, $\theta_w = 2\Delta_h/L$, where L is the cantilevered sheathing length, is calculated by using experimental measurements of sheathing lateral deflection obtained from displacement transducers attached to the sheathing during loading. The reliability of this expression is pivotal towards validation of extracted rotational stiffness values for sheathing, $k_{\phi w,}$ and connection rotational stiffness, $k_{\phi c2}$, as both are directly dependent on sheathing rotation.

This expression is based upon small angle approximations however, a condition that is violated by plywood sheathing subject to substantial rotational deformation. To explore the relevance of this approximation, comparative plots as shown in Figure 16 and Figure 17 are created using Mastan in which sheathing rotations calculated using the expression and Mastan sheathing lateral deflection are compared to nodal rotations yielded by Mastan second order elastic analysis. Vertical lines within each plot indicate actual and doubled rotations within the linear range in which rotational stiffness values were calculated using linear regression during experimental post processing. In this case, OSB is modeled and compared in addition to plywood to provide a reliable baseline control condition. Gypsum is not analyzed however as sheathing rotation was minimized due to axial pull out failure occurring early within each gypsum test.

From the plots and the summary table presented in Table 1, it can be observed that the derived sheathing rotation expression yields a slightly less conservative value of sheathing rotation, θ_w, and consequently sheathing rotational stiffness, $k_{\phi w}$ also, due to underestimating sheathing rotation for both OSB and plywood. Nonetheless, large divergence between the sheathing rotation expression plot and Mastan plot does not occur even late into testing deformation. This is supported by the percent errors of 1.70% and .86% for plywood and OSB respectively at twice the actual rotations used to calculate experimental rotation stiffness values, validating the accuracy of the derived expression in calculating sheathing rotation within the early linear range of deformation despite large rotations exhibited by plywood sheathing.

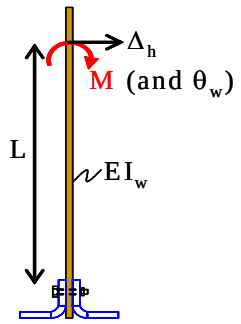

Figure 15 Analytical model used for sheathing rotation derivation
Source: Experiments on Rotational Restraint of Sheathing, 2007

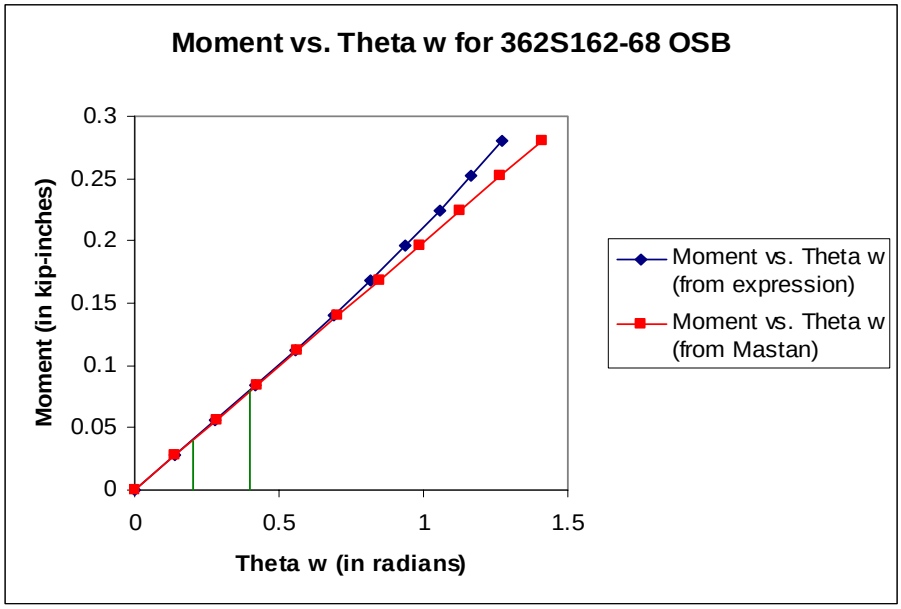

Figure 16 Plot of Moment at Fastener vs. OSB Sheathing Rotation using Mastan nodal rotation and derived sheathing rotation expression

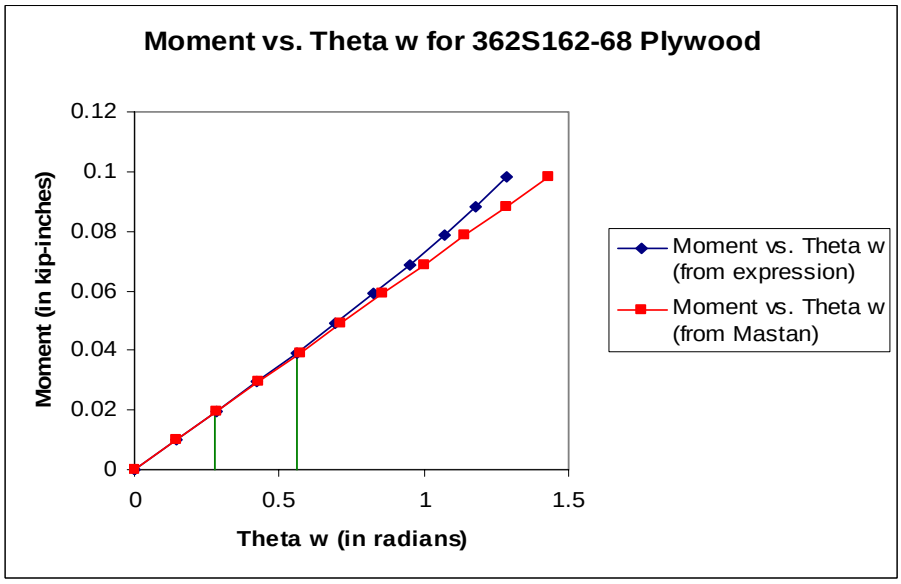

Figure 17 Plot of Moment at Fastener vs. Plywood Sheathing Rotation using Mastan nodal rotation and derived sheathing rotation expression

Table 1 Summary of Comparative Sheathing Rotation Results

Sheathing Modeled	Percent Error at Rotation	Percent Error at Twice Rotation
Plywood	.00	1.70
OSB	.29	.86

3.2 P-Delta effects

In creating plots corresponding to Figure 14 for each experimental test, raw load and vertical displacement data is converted into moment and rotation. For simplicity, moment per unit width at the connection, M, is found using the expression $M=(P/w)h_o$ where P is the measured load, w is the sheathing transverse width, and h_o is the joist depth. During experimental testing, the presence of a changing moment arm due to deformation was acknowledged but the present moment expression was used nonetheless due to simplicity and means of using available measurements. Using this expression assumes the changing moment arm during testing is close in magnitude to h_o and that other P-Δ effects due to geometry do not significantly affect the $M=(P/w)h_o$ approximation.

These effects were originally presented in an analytical figure from the first AISI report (Schafer 2007) that is reproduced in Figure 18. In Figure 18d, the moment taking into account due to the changing moment arm is calculated as $M=Ph_o\cos\alpha$ where α is the angle between the flange where load is applied and the vertical. Calculating moment as $M=Ph_o$ assumes this angle α is negligible however. To explore this nonlinear moment effect due to the changing moment arm, Mastan models similar to Figure 3 are used by comparing moment calculated as $M=Ph_0$ to actual Mastan moment at the fastener connection node shown in Figure 4. Comparative plots demonstrating the this changing moment arm effect are presented from Figure 20 to Figure 29 and summarized in Table 2.

Also evident from Figure 18, P-Δ effects come into play due to the axial load P acting eccentrically to the sheathing centroid as shown in Figure 18b and Figure 18c. Therefore to assess the P-Δ effects, the deformation response of an equivalent cantilevered sheathing model subject to axial load, P, and moment, Ph_o, as shown in Figure 19a can be compared to the deformation response of a cantilevered sheathing model subject to moment, Ph_o, but without an axial load, P as shown in Figure 19b. By comparing these cantilevered sheathing models using second order elastic analysis in Mastan, the P-Δ effects due to the eccentric axial load alone are assessed as shown from Figure 30 to Figure 39 with a summary in Table 3.

Vertical lines within these plots displayed from Figure 20 to Figure 39 denote actual rotations in which rotational stiffness values were calculated within the linear range of experimental data and a second rotation at double this value. This allows for the quantification of both moment arm and P-Δ nonlinear effects early and far into the linear range of Moment vs. Theta behavior.

From Figure 24 to Figure 29, it can be observed with the closeness between the Mastan at the fastener node and $M=Ph_0$ curves, the effect of the changing moment arm on approximating Moment as $M=Ph_o$ with a constant moment arm are minimal. Figure 20 to Figure 23 do however indicate that the changing moment arm can have a significant effect on ultimate strength through degradation of moment and rotational stiffness. However, this does not occur within the linear range in which rotational stiffness values are however as evidenced by a maximum percent error of 8.14% in Table 2 Summary of Moment Arm Effects, indicating moment arm effects are still relatively small even at twice the rotation at which rotational stiffness values are calculated .

P-Δ effects in contrast are dependent on the setup with 362S joists plots such as Figures Figure 22 and Figure 23 showing greater significance compared to 1200S joists in plots such as Figure 24 and Figure 25. The results are generally consistent with expectations accompanying deflections. There are less P-Δ effects present within tests with 1200S joists as there is less eccentricity experienced by the axial load due to smaller sheathing lateral deflections in contrast to tests with 362S joists. Due to this, the present expression used to calculate moment is generally very accurate for tests involving

1200S joists as evident by the closeness of Mastan cantilever output curves with and without an eccentric axial load. For trials with 362S joists with higher sheathing deflections and rotations, there is greater divergence between the Mastan cantilever curves suggesting greater P-Δ effects. This is supported in Table 3 Summary of P-Δ Effectswith a maximum percent error of 14.17% among tests with 362S joists compared to a maximum percent error of 7.89% among tests with 1200S joists at actual rotations used to calculate rotational stiffness values.

Table 3 also shows amplification of P-Δ effects and large deviation between Mastan cantilever curves with and without the axial load is significant at larger rotations. At twice the actual rotation used to calculate rotational stiffness values, a significantly higher maximum percent error of 26.38% is observed. As rotational stiffness values were extracted from experimental measurements early within the linear range however, the maximum discrepancy between calculated and actual moment at actual rotations used however is lower at 14.17% for a 1200S joist test.

While P-Δ effects have the potential to increase both moment and rotation during deformation, it is evident that P-Δ effects within these tests contribute more towards rotation as displayed by the lower slope presented by cantilever curves containing the eccentric axial load compared to cantilever output curves without the axial load P-Δ effect. Moment calculated as $M=(P/w)h_o$ as impacted by P-Δ effects should therefore slightly underestimate actual moment due to larger P-Δ effects affecting rotation instead.

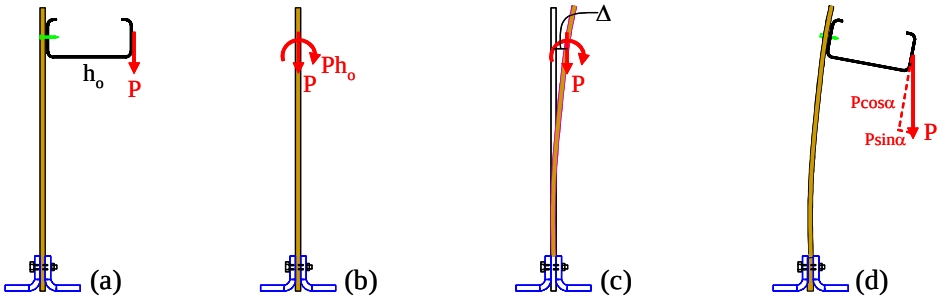

Figure 18 Analytical Models demonstrating nonlinear P-Δ effects
Source: Experiments on Rotational Restraint of Sheathing, 2007

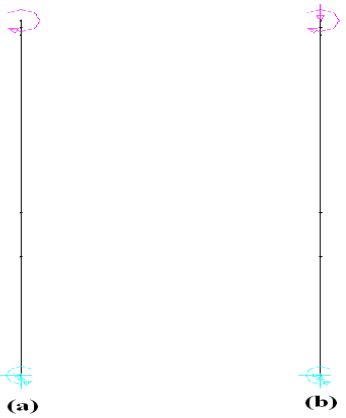

Figure 19 Mastan cantilever models used for assessing P-Δ effects

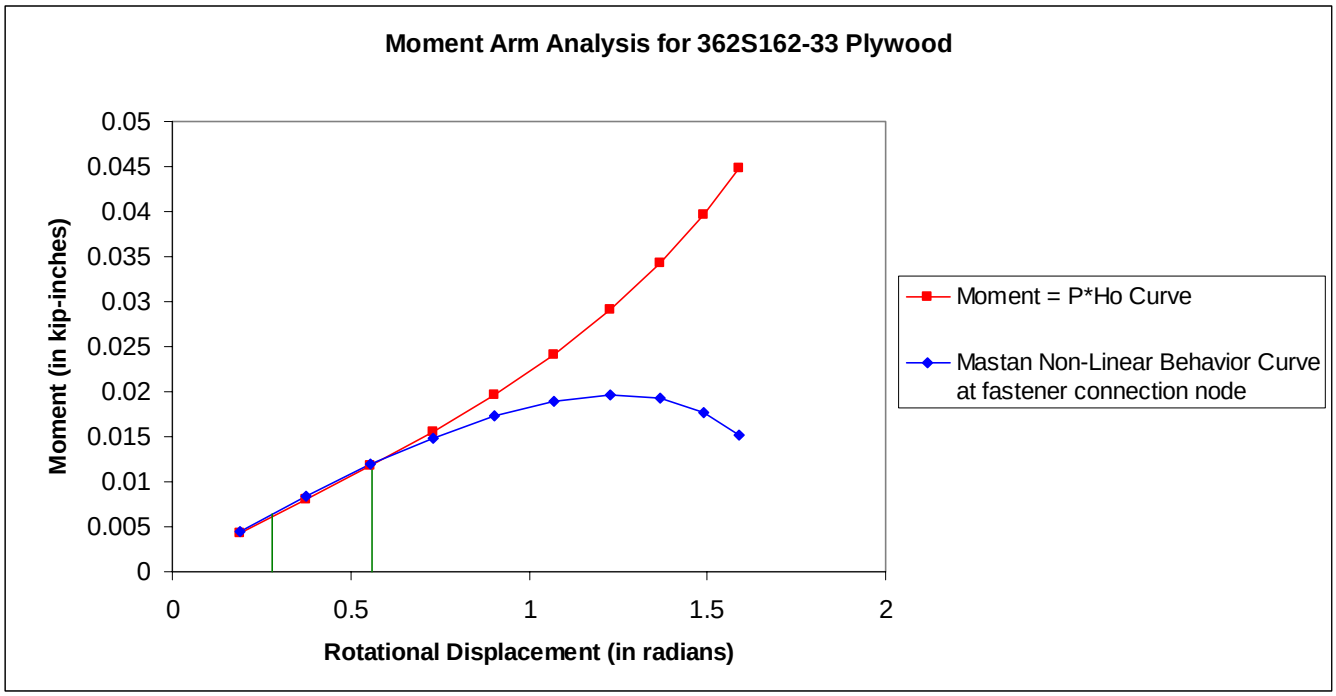

Figure 20 Plot of differential moment arm effects in Mastan For 362S162-33 Joist with Plywood Sheathing

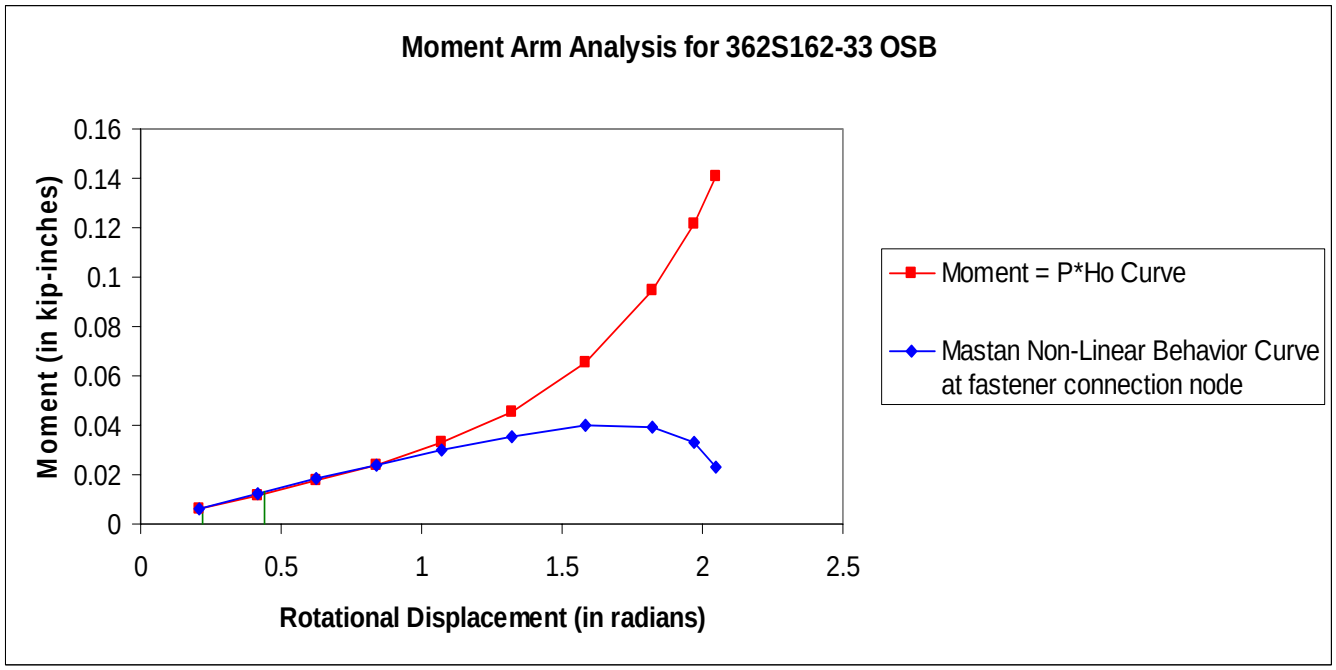

Figure 21 Plot of differential moment arm effects in Mastan For 362S162-33 Joist with OSB Sheathing

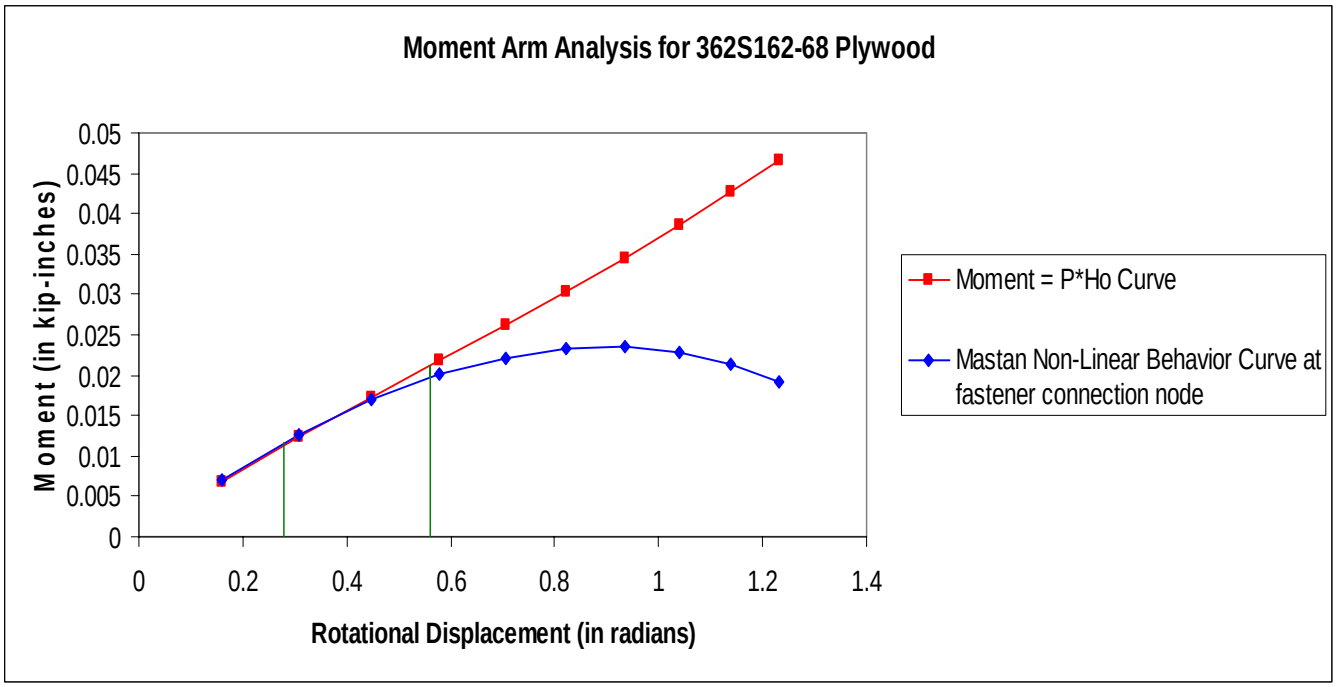

Figure 22 Plot of differential moment arm effects in Mastan For a 362S162-68 Joist with Plywood Sheathing

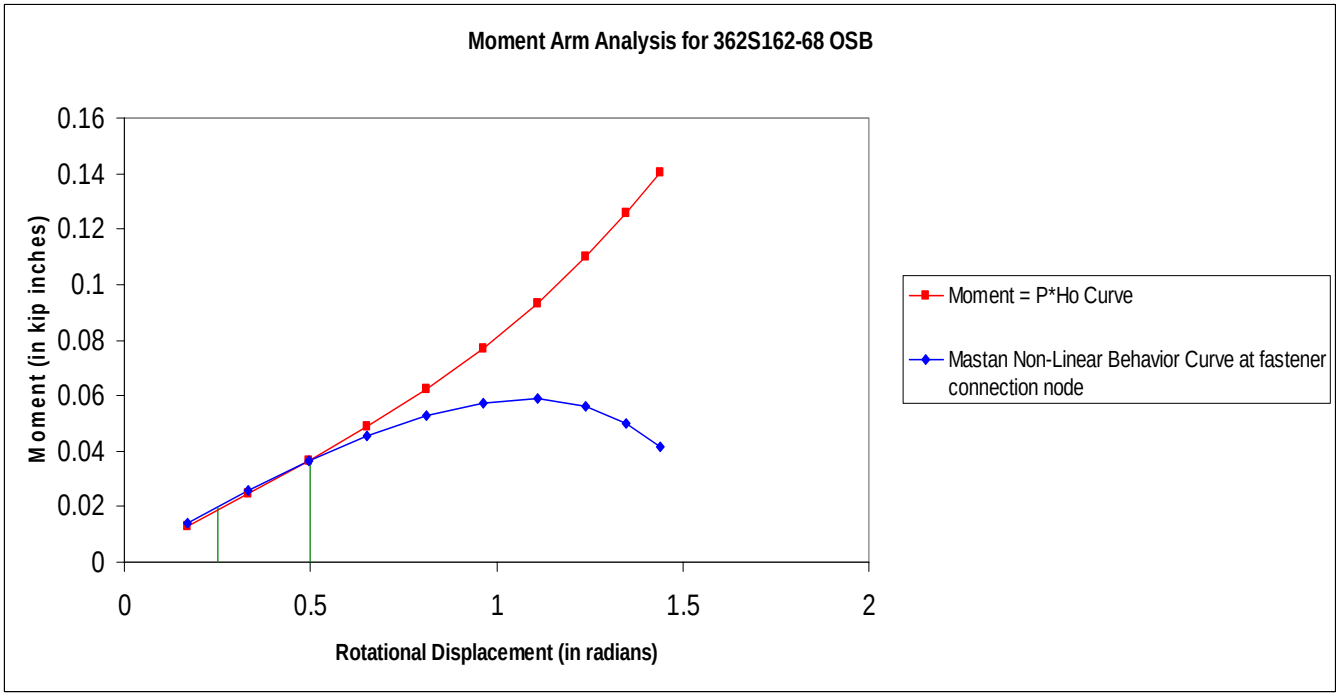

Figure 23 Plot of differential moment arm effects in Mastan For a 362S162-68 Joist with OSB Sheathing

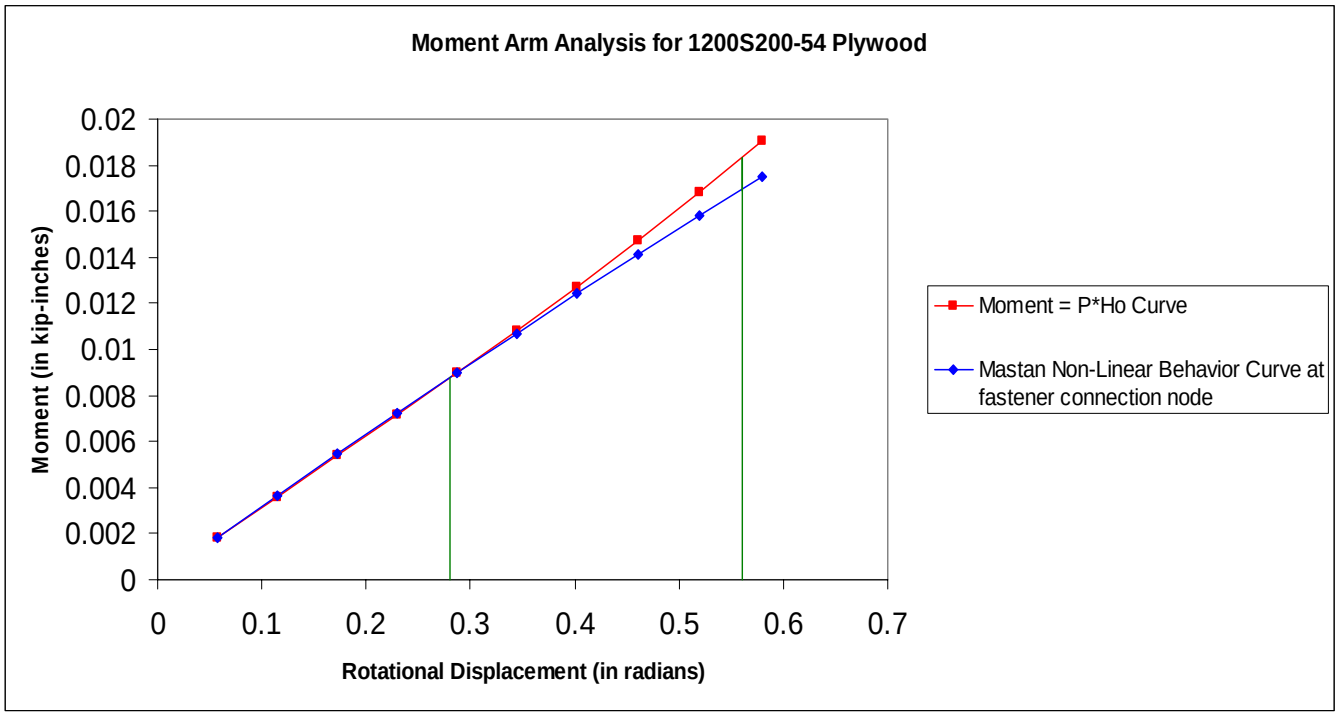

Figure 24 Plot of differential moment arm effects in Mastan For a 1200S200-54 Joist with Plywood Sheathing

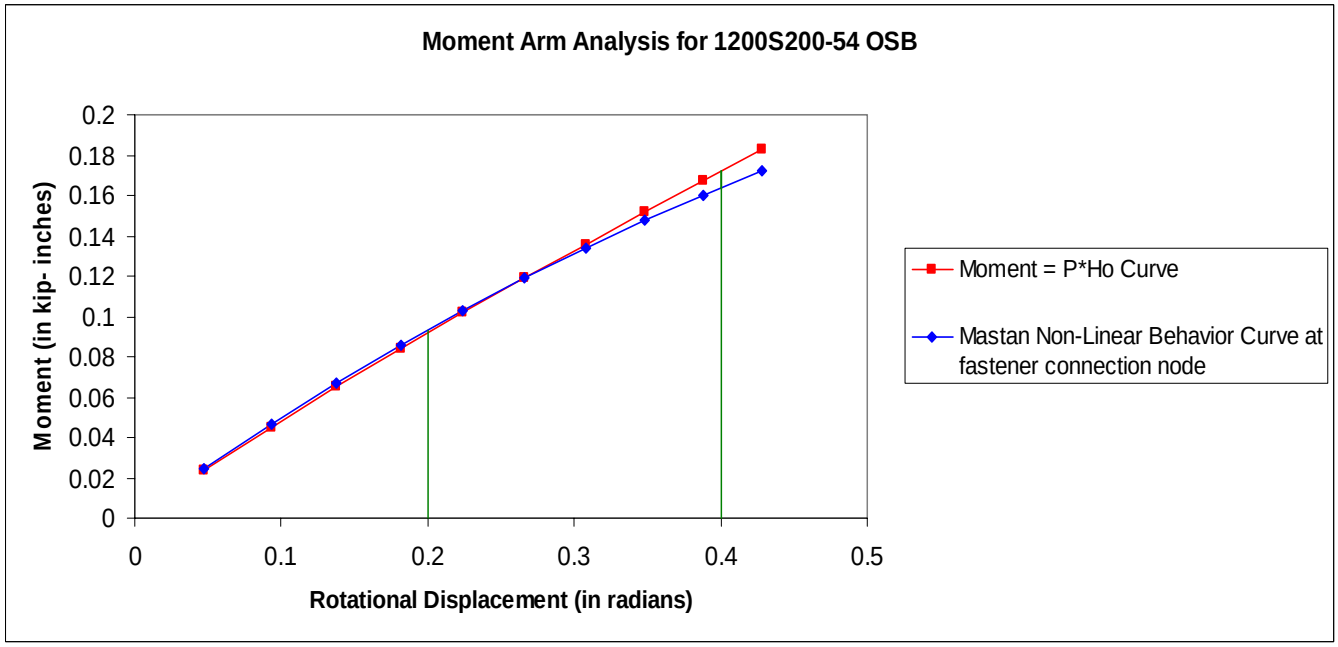

Figure 25 Plot of differential moment arm effects in Mastan For a 1200S200-54 Joist with OSB Sheathing

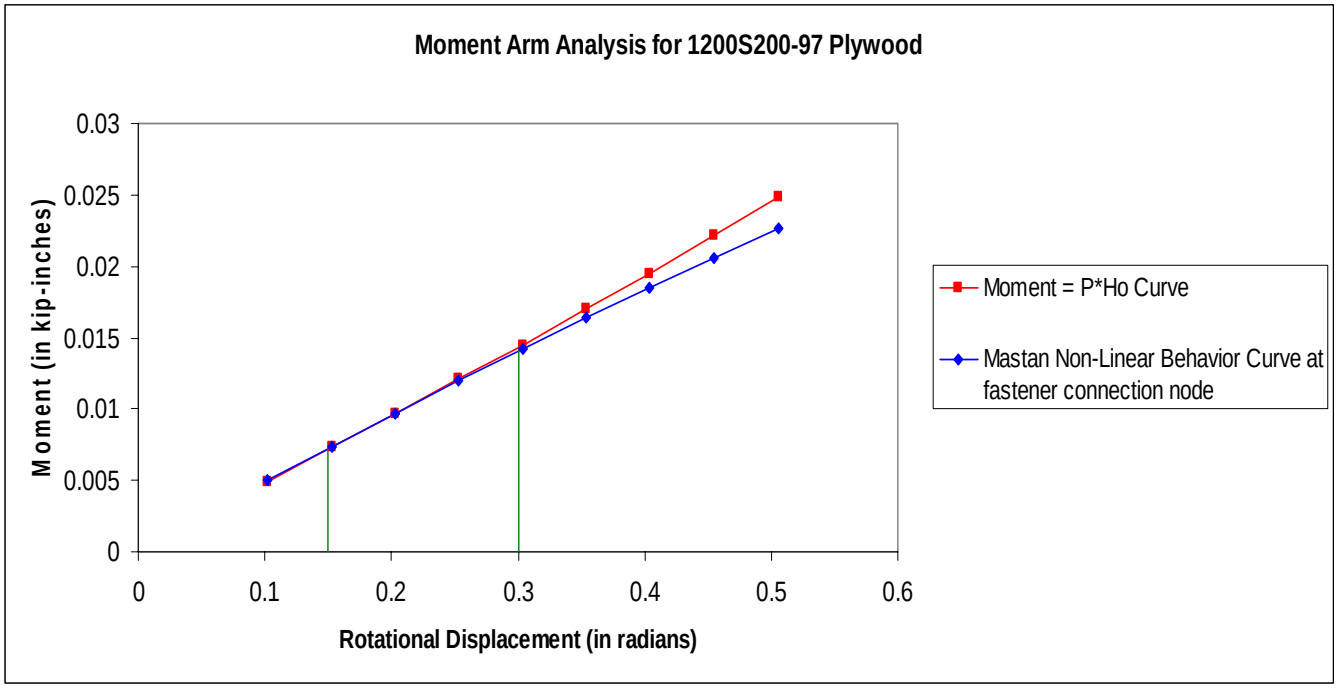

Figure 26 Plot of differential moment arm effects in Mastan For a 1200S200-97 Joist with Plywood Sheathing

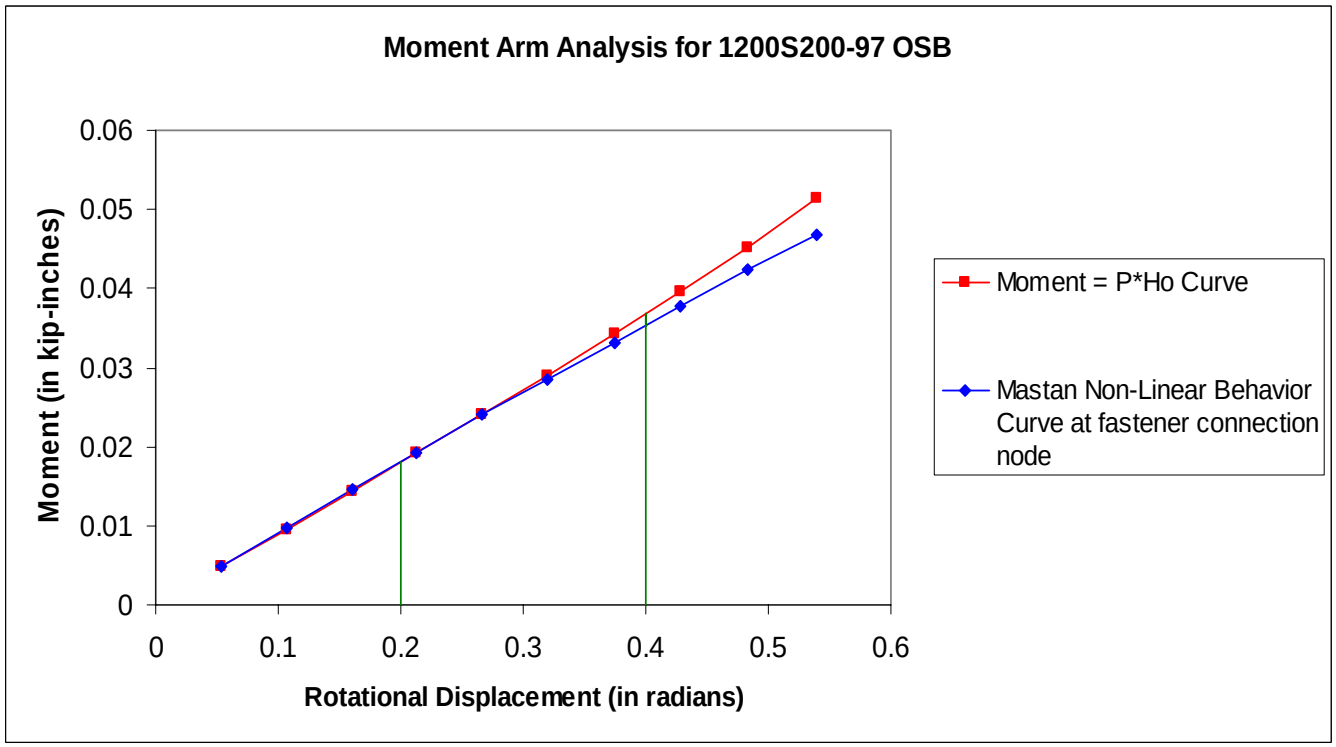

Figure 27 Plot of differential moment arm effects in Mastan For a 1200S200-97 Joist with OSB Sheathing

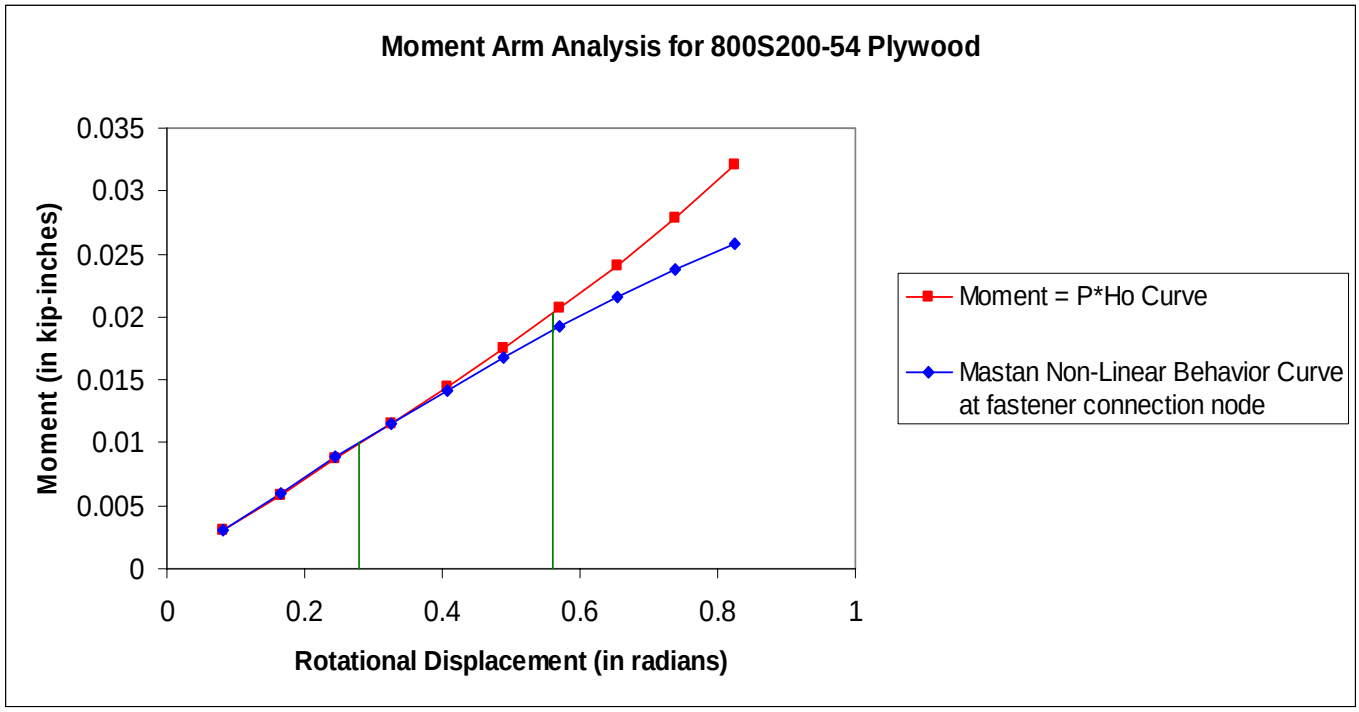

Figure 28 Plot of differential moment arm effects in Mastan
For a 800S200-54 Joist with OSB Sheathing

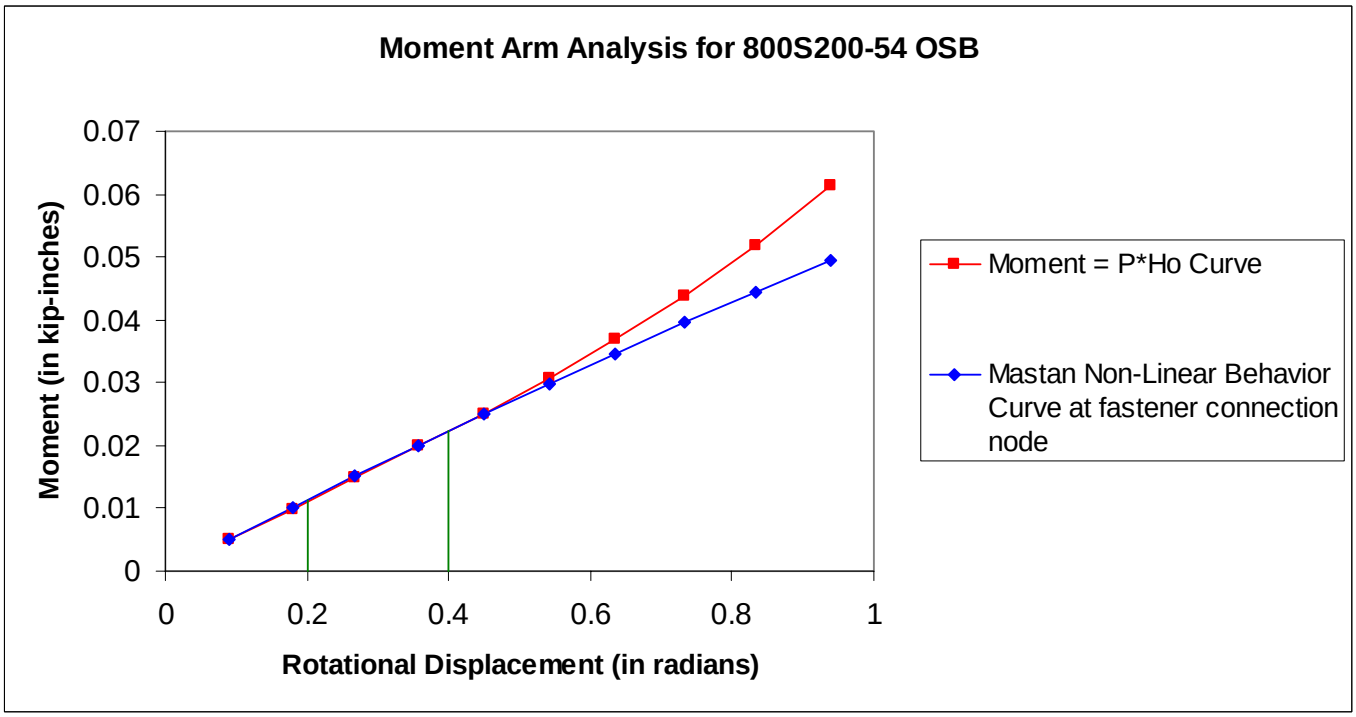

Figure 29 Plot of differential moment arm effects in Mastan
For a 800S200-54 Joist with OSB Sheathing

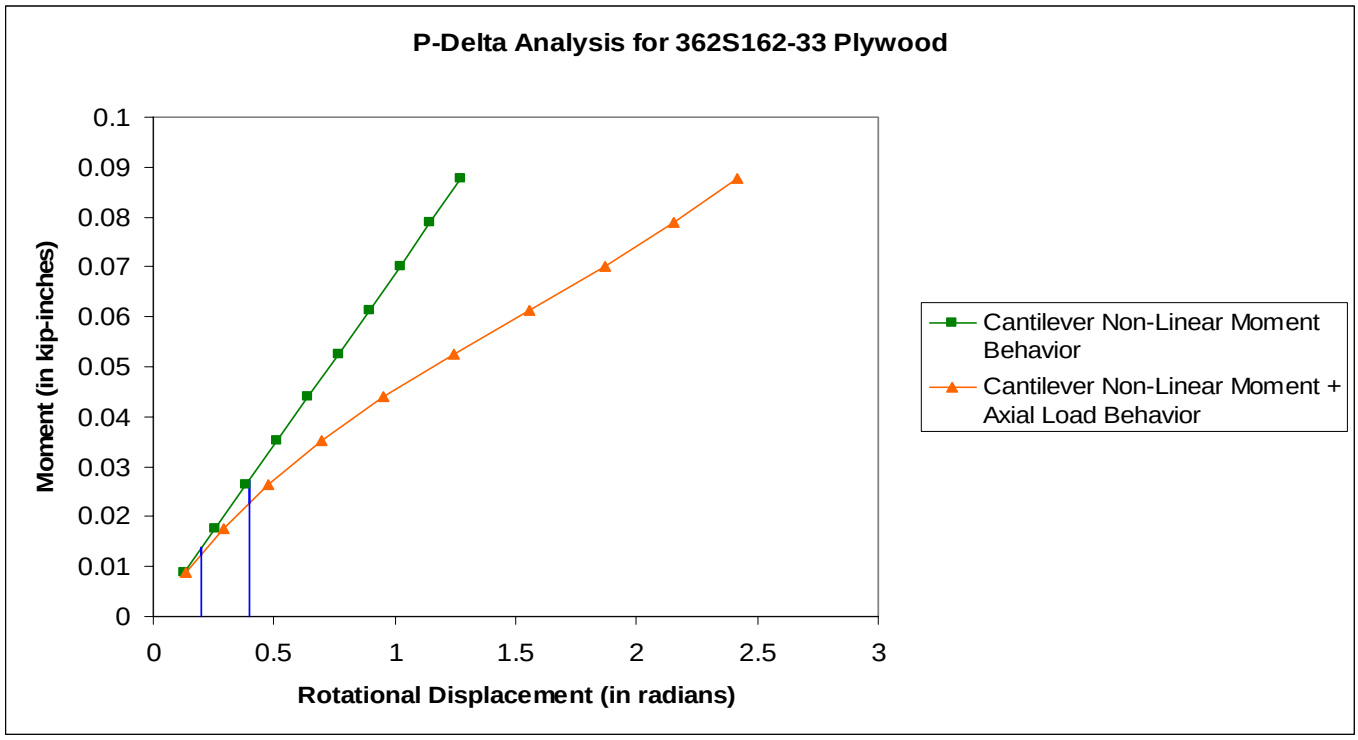

Figure 30 Plot of P-Δ effects in Mastan
For a 362S162-33 Joist with Plywood Sheathing

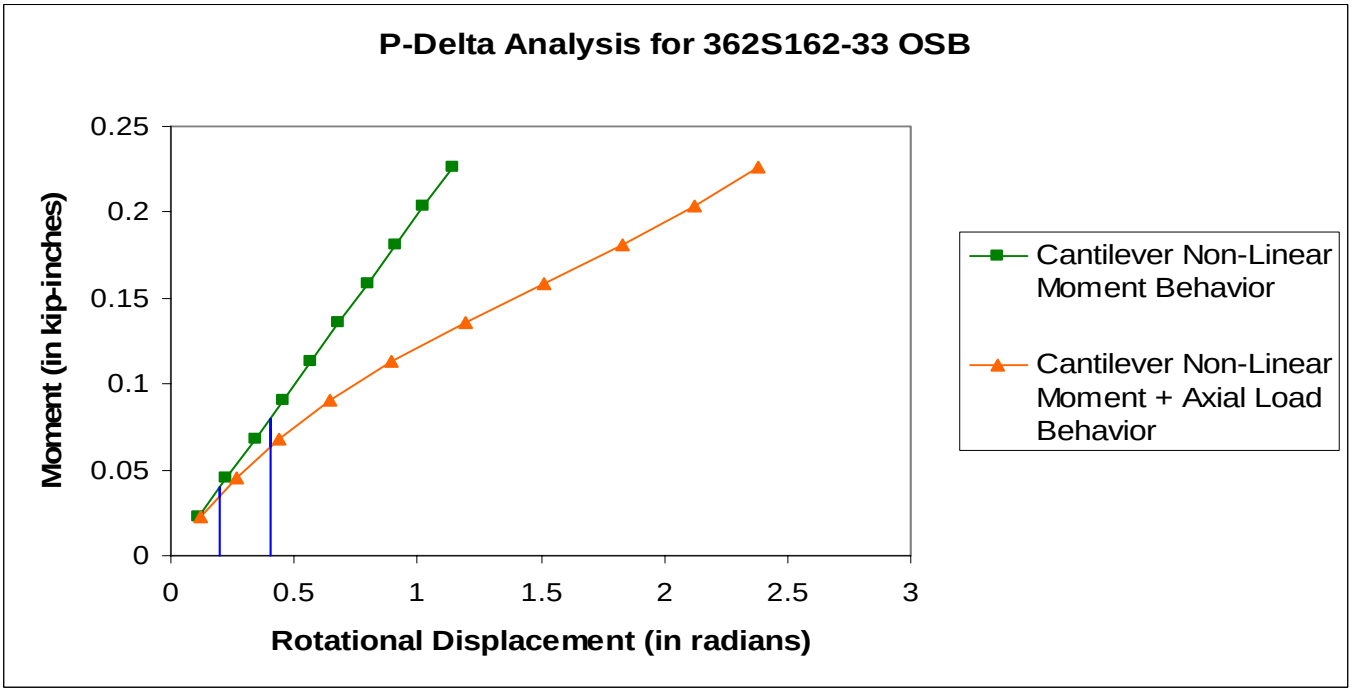

Figure 31 Plot of P-Δ effects in Mastan
For a 362S162-33 Joist with OSB Sheathing

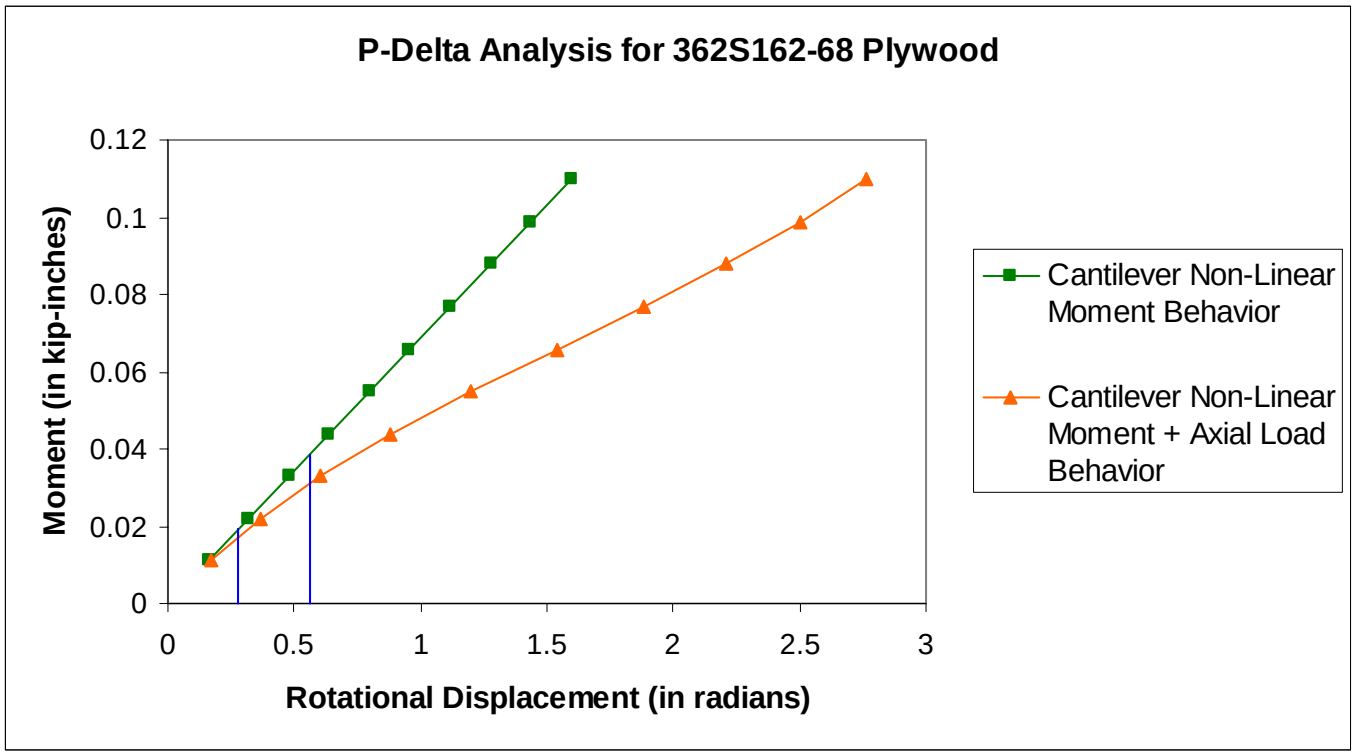

Figure 32 Plot of P-Δ effects in Mastan
For a 362S162-68 Joist with Plywood Sheathing

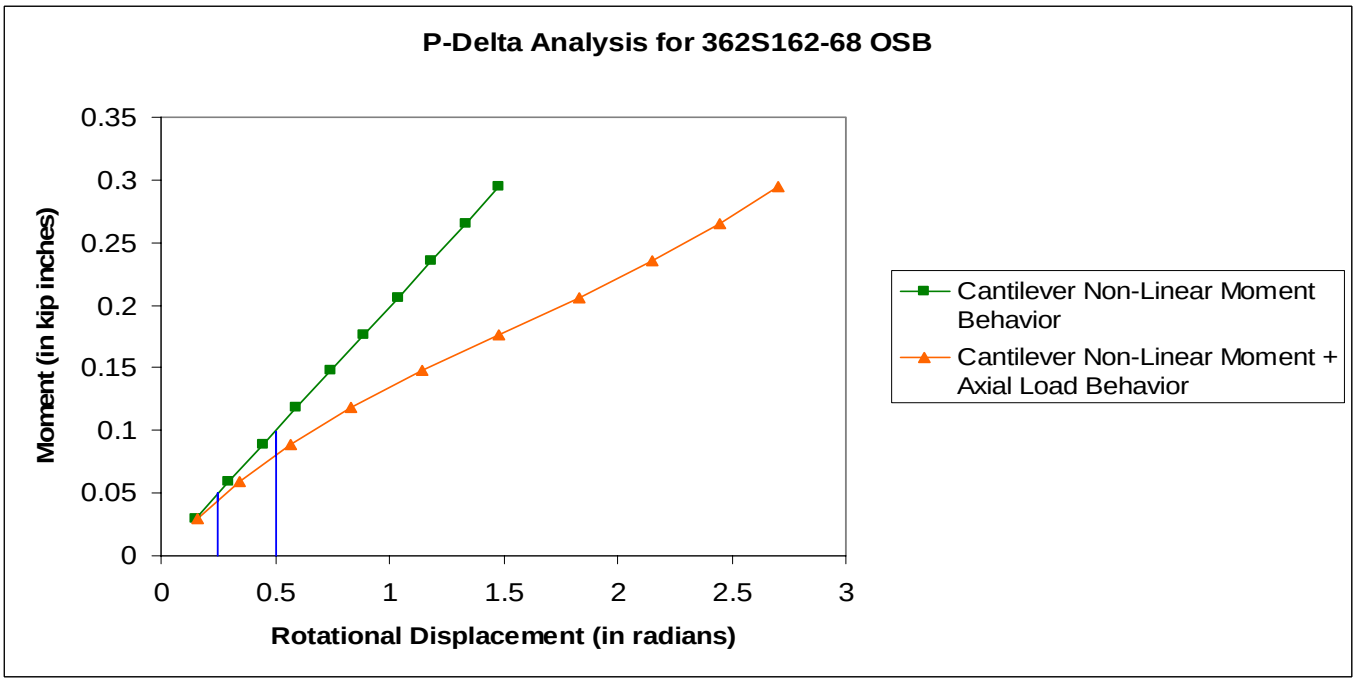

Figure 33 Plot of P-Δ effects in Mastan
For a 362S162-68 Joist with OSB Sheathing

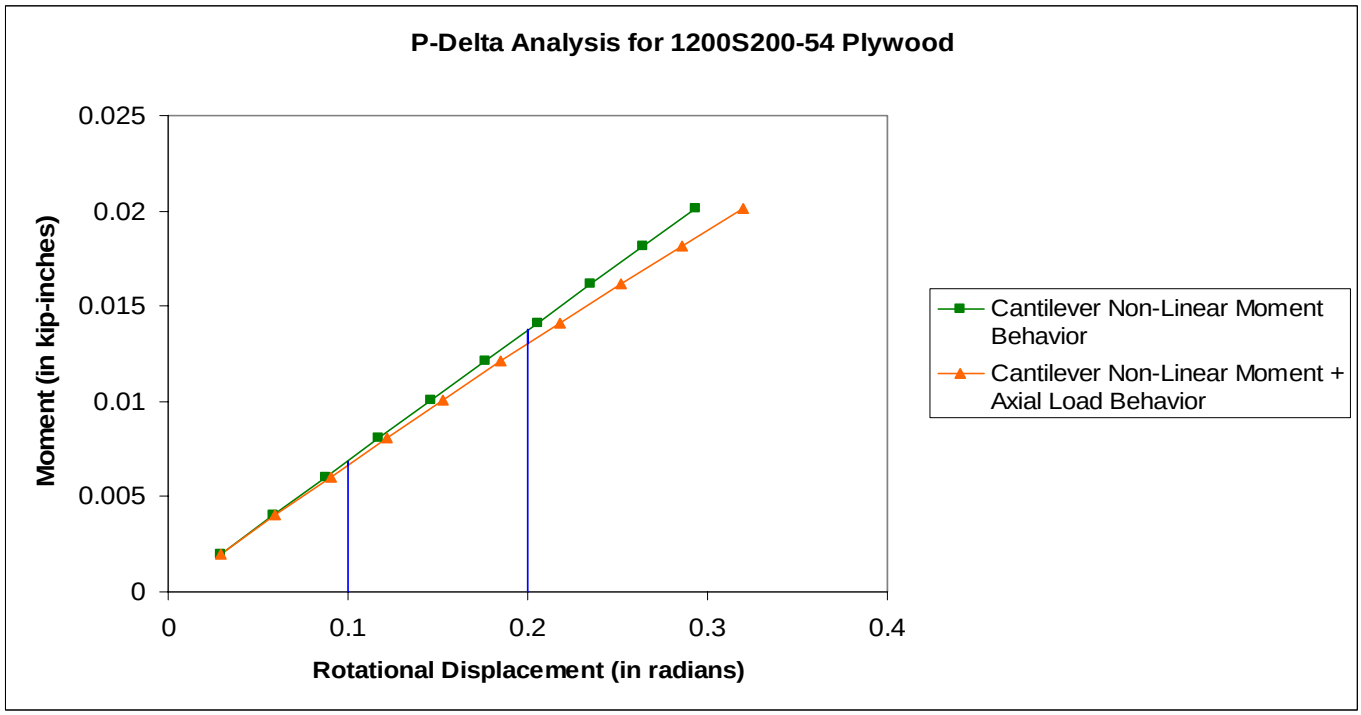

Figure 34 Plot of P-Δ effects in Mastan
For a 1200S200-54 Joist with Plywood Sheathing

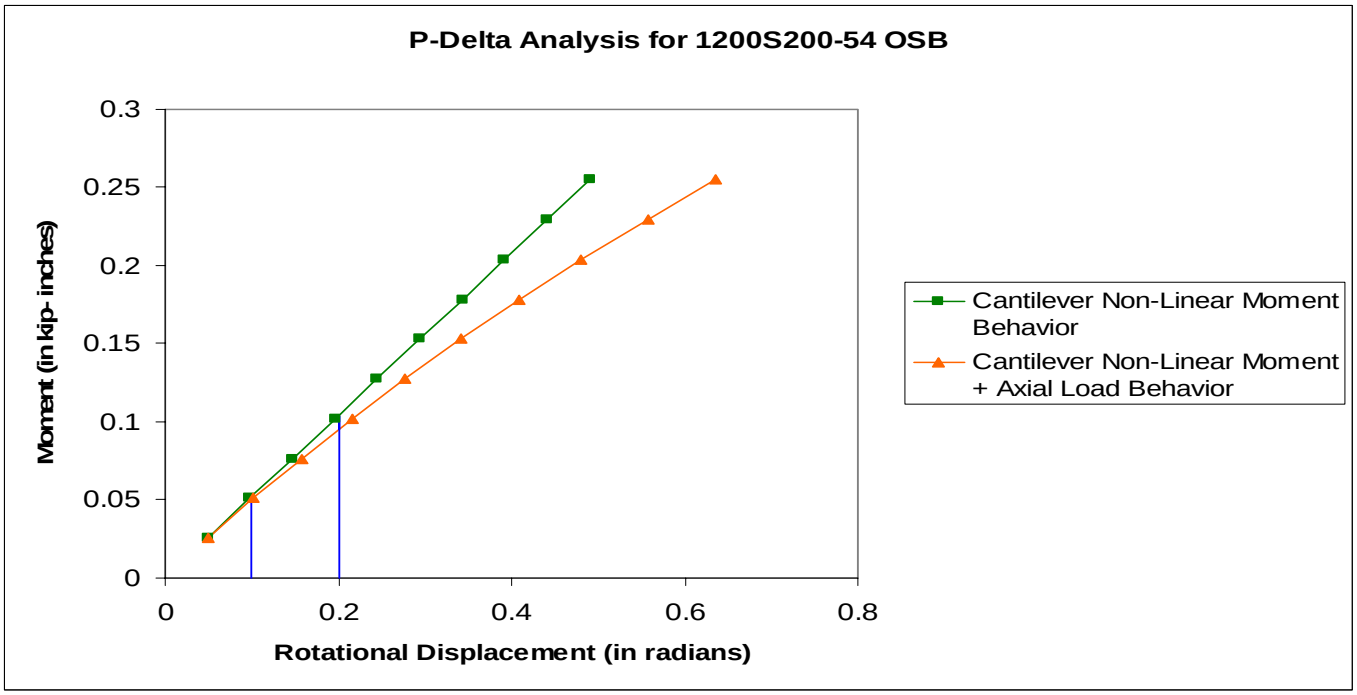

Figure 35 Plot of P-Δ effects in Mastan
For a 1200S200-54 Joist with OSB Sheathing

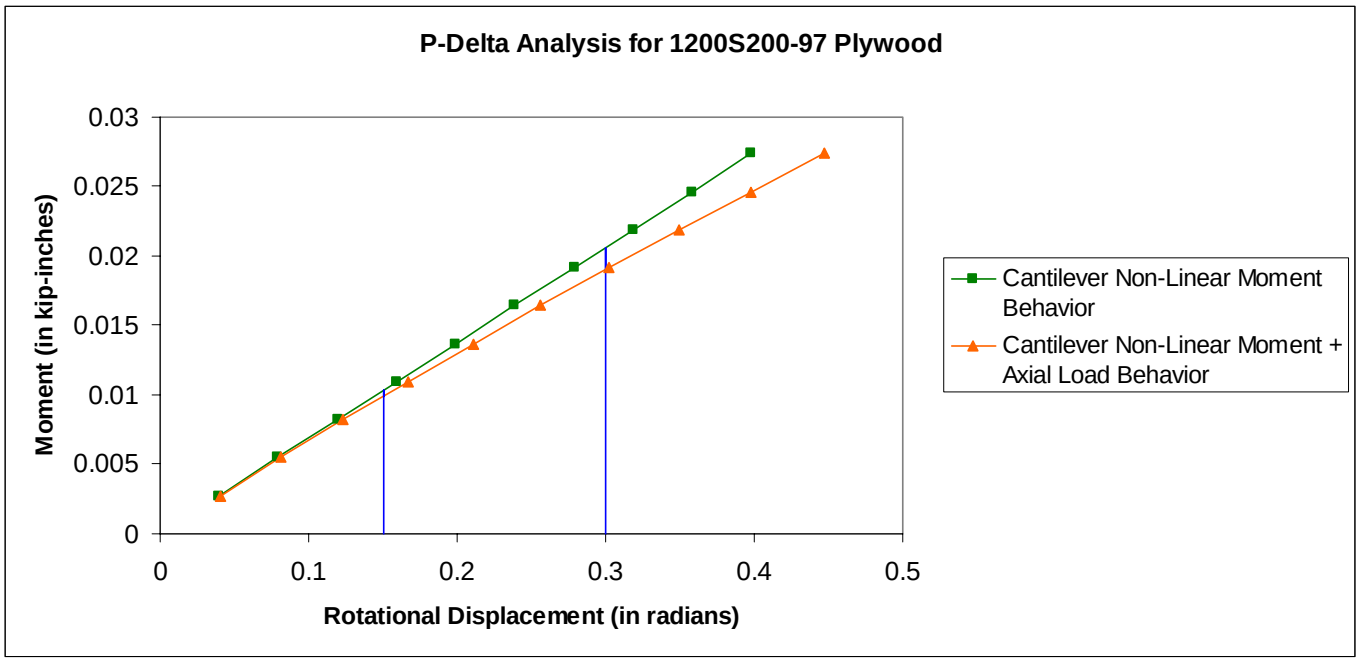

Figure 36 Plot of P-Δ effects in Mastan
For a 1200S200-97 Joist with Plywood Sheathing

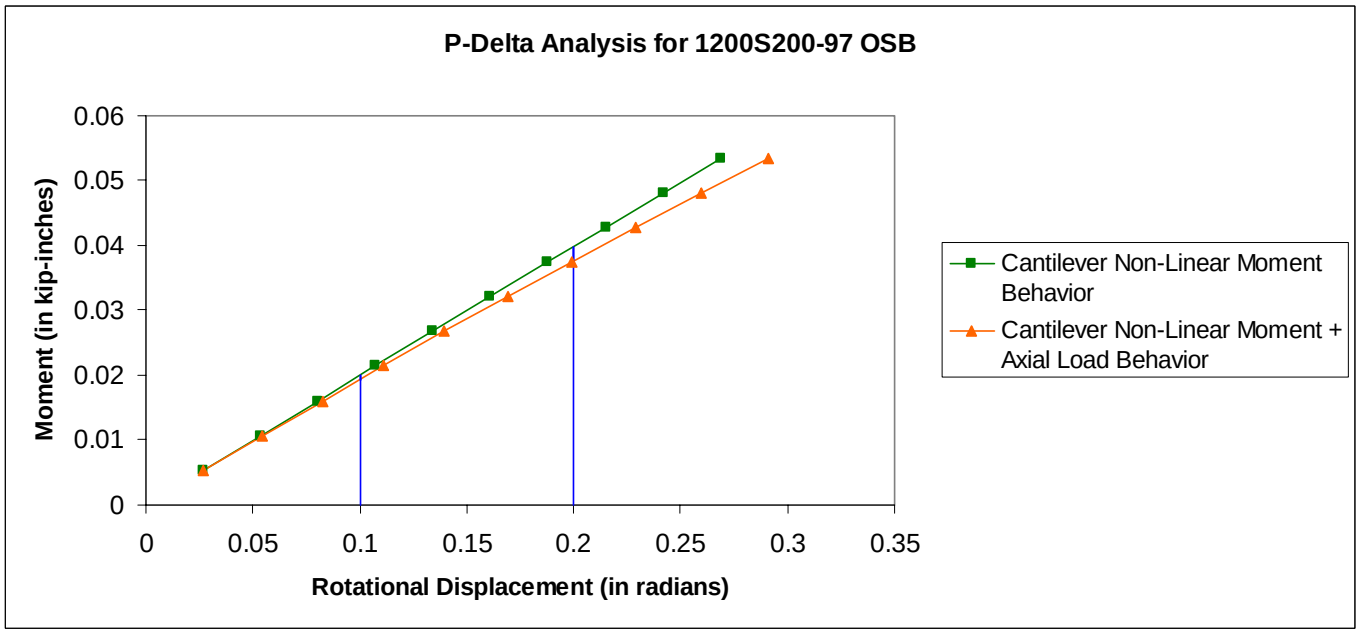

Figure 37 Plot of P-Δ effects in Mastan
For a 1200S200-97 Joist with OSB Sheathing

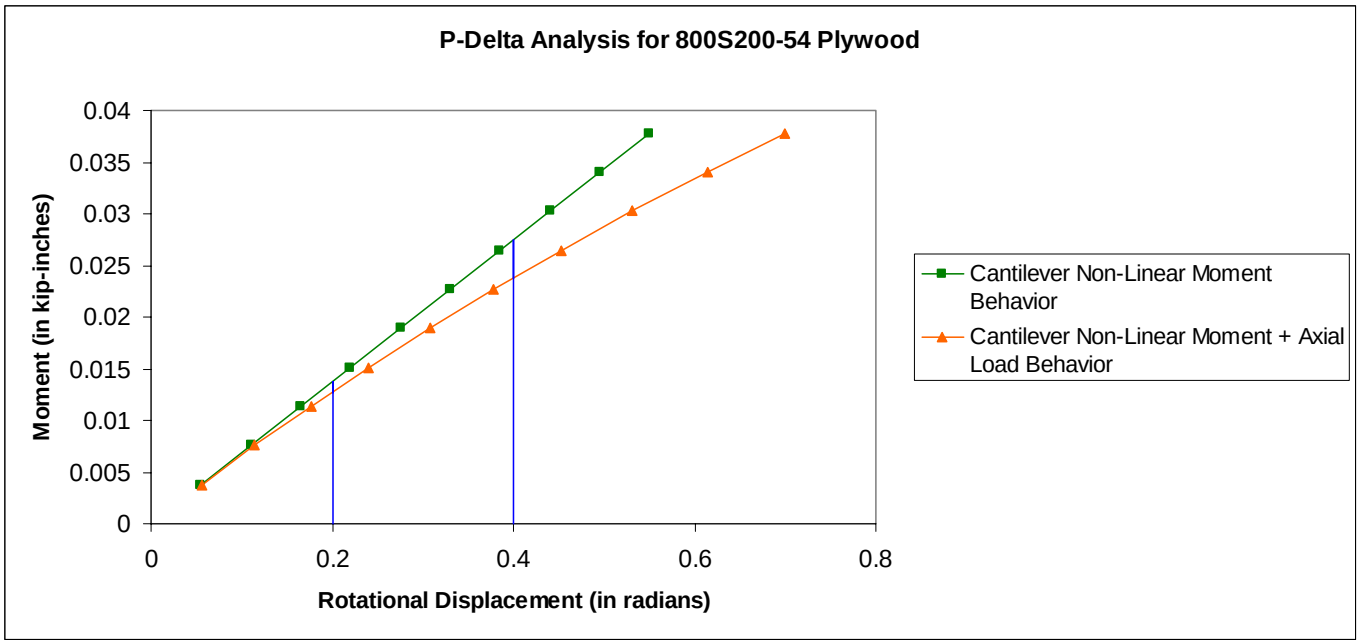

Figure 38 Plot of P-Δ effects in Mastan
For a 800S200-54 Joist with Plywood Sheathing

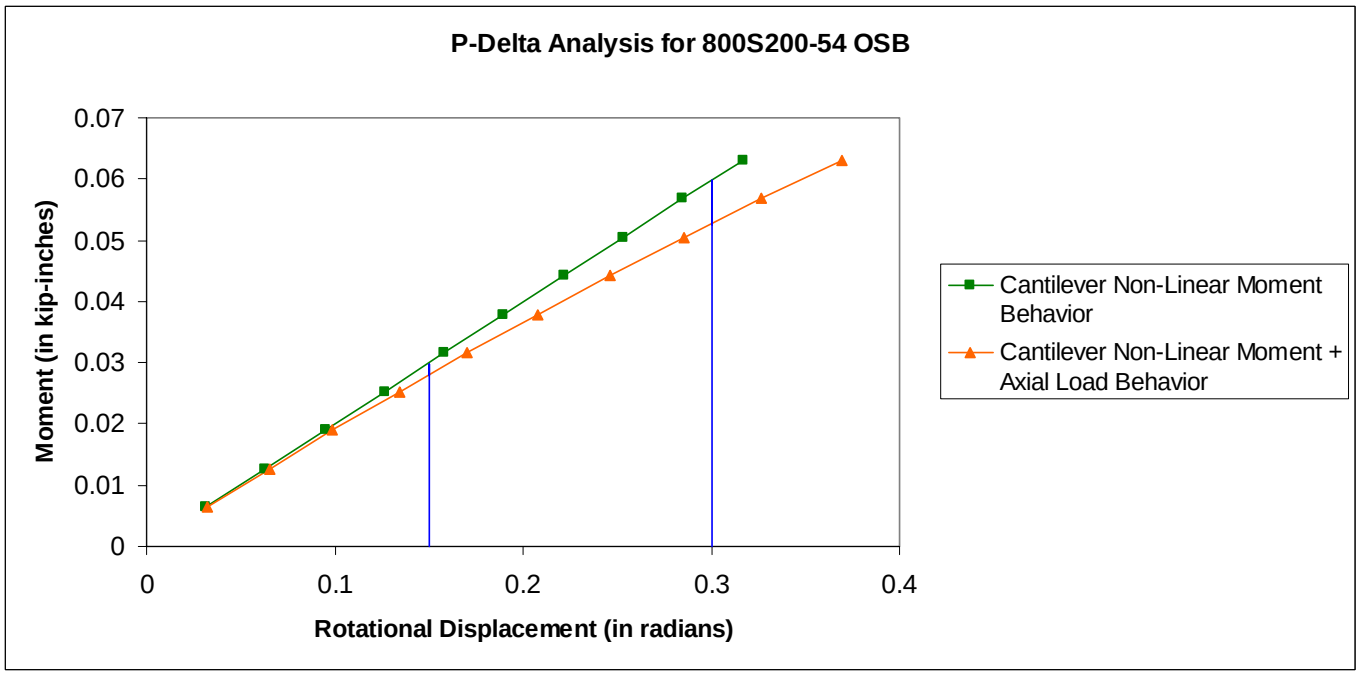

Figure 39 Plot of P-Δ effects in Mastan
For a 800S200-54 Joist with OSB Sheathing

Table 2 Summary of Moment Arm Effects

Setup Modeled	Percent Error at Rotation	Percent Error at Twice Rotation
362S162-33 Plywood	5.42	1.49
362S162-33 OSB	7.39	6.66
362S162-68 Plywood	2.11	8.14
362S162-68 OSB	4.47	0.43
1200S200-54 Plywood	0.05	8.23
1200S200-54 OSB	1.16	5.16
1200S200-97 Plywood	.46	4.06
1200S200-97 OSB	.67	2.10
800S200-54 Plywood	.78	7.46
800S200-54 OSB	2.51	.06

Table 3 Summary of P-Δ Effects

Setup Modeled	Percent Error at Rotation	Percent Error at Twice Rotation
362S162-33 Plywood	14.17	26.38
362S162-33 OSB	11.76	21.87
362S162-68 Plywood	9.53	17.86
362S162-68 OSB	13.67	25.32
1200S200-54 Plywood	2.91	5.76
1200S200-54 OSB	4.55	9.41
1200S200-97 Plywood	2.98	5.82
1200S200-97 OSB	4.20	8.29
800S200-54 Plywood	7.89	15.70
800S200-54 OSB	6.71	13.47

3.3 Joist bending effects

As presented in the original report, and based on Figure 13, total rotation, $\theta_2 = \tan^{-1}(\Delta_v/h_o)$ where Δ_v is vertical displacement and h_o is the joist web depth. This rotation includes sheathing rotation, fastener rotation, and joist bending. Within the original report, sheathing rotation, was defined as $\theta_w = 2\Delta_h/L$ while connection rotation was defined as $\theta_{c2} = \theta_2 - \theta_w$.. Reported connection rotational stiffness, $k_{\phi c2}$, therefore includes rotation of the fastener, θ_c, and rotation due to joist bending, θ_s. However, less conservative but more efficient connection stiffness values, $k_{\phi c}=M/\theta_c$, without added flexibility due to joist bending and based on fastener rotation alone, may prove to be more useful to designers.

An attempt to decompose $k_{\phi c2}$ values into $k_{\phi c}$ involved using beam mechanics and assuming joist deformation behaved as cantilevered web bending resulting in deflection of the joist web quantified as $\Delta_s \approx Ph_o^3/3E_sI_s$. Joist bending rotation, θ_s, under this assumption could be found using $\theta_s = \tan^{-1}(\Delta_s/h_o)$ and removed from θ_{c2} resulting in isolating connection rotation, θ_c, and ultimately connection stiffness, $k_{\phi c}$. However, analysis of isolated $k_{\phi c}$ values using this approach led to $k_{\phi c}$ values which stiffened with rotation, rendering this approach towards isolating and removing θ_s invalid. Actual θ_s values based on experimental observations were believed to be smaller than calculated, rendering $k_{\phi c}$ values found using simplistic beam mechanics to be overly conservative. Short of using additional displacement transducers at the connection; however, there was also no way to accurately quantify θ_s using available experimental measurements during testing. These conclusions ultimately lead to the use of $k_{\phi c2}$ within the original report.

Using Mastan to model combinations of sheathing and joists experimentally tested; however, it is possible to assess the significance of joist bending by looking at nodal rotations resulting from Mastan analysis. By creating Mastan models using the truss approach depicted in Figure 3 and using decomposed nodal rotations shown in Figure 4 for each model, the significance of joist bending, in addition to sheathing and fastener rotation can be found in relation to total rotation. With joist bending defined as the difference in rotations between the total rotation node and connector node shown in Figure 4, joist bending effects for each sheathing and joist combination can be explored as a function of the fastener axial stiffness of each model.

As fastener axial stiffness, EA/L, within Mastan is increased; the fastener becomes more rigid allowing for an accurate assessment of the maximum joist bending contributions. Plots of Mastan analysis output using this approach detailing joist bending contribution as a fraction of total rotation based on varying axial stiffness created for each sheathing and joist combination are shown from Figure 40 to Figure 49. Tables summarizing rotational decompositions for a flexible and rigid fastener are presented in Table 4 and Table 5.

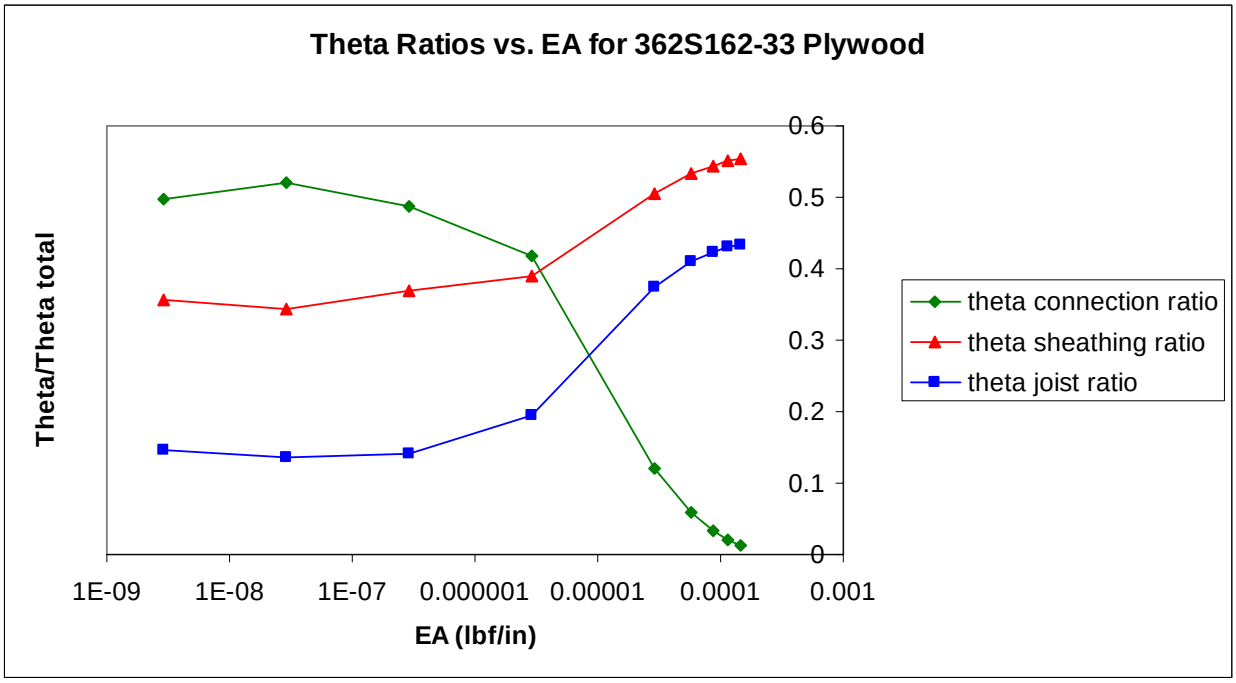

Figure 40 Plot of Mastan output of decomposed rotational contributions For a 362S162-33 Joist with Plywood Sheathing

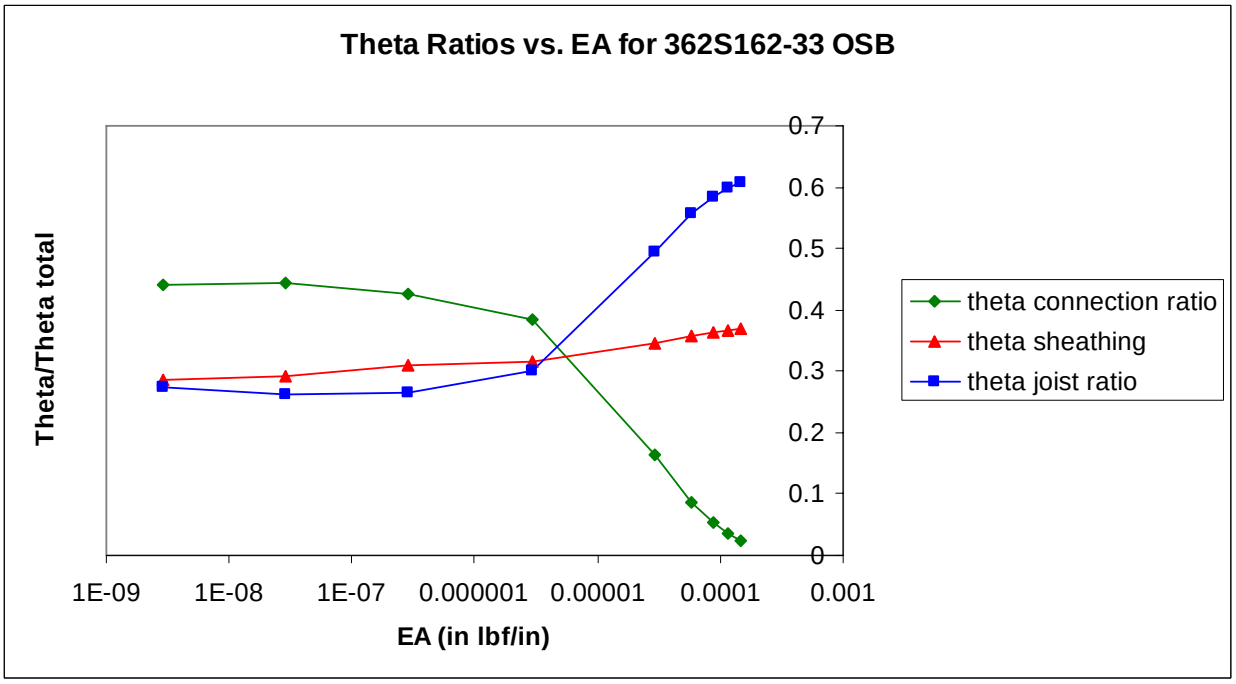

Figure 41 Plot of Mastan output of decomposed rotational contributions For a 362S162-33 Joist with OSB Sheathing

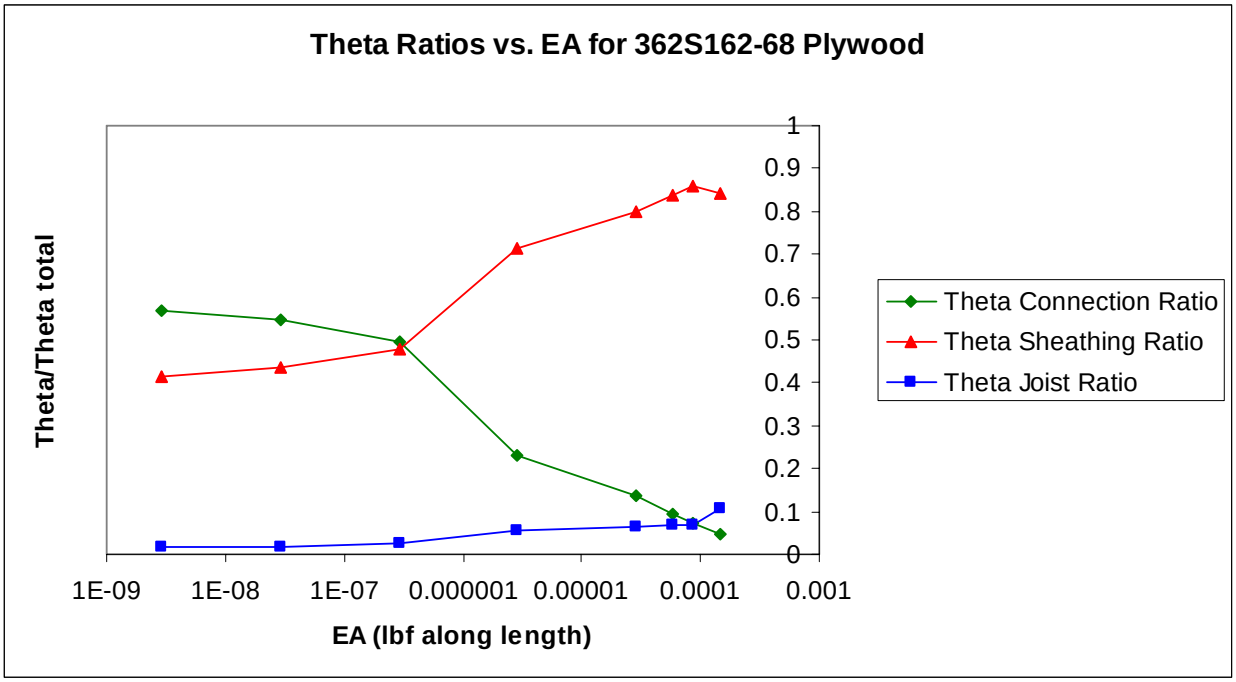

Figure 42 Plot of Mastan output of decomposed rotational contributions For a 362S162-68 Joist with Plywood Sheathing

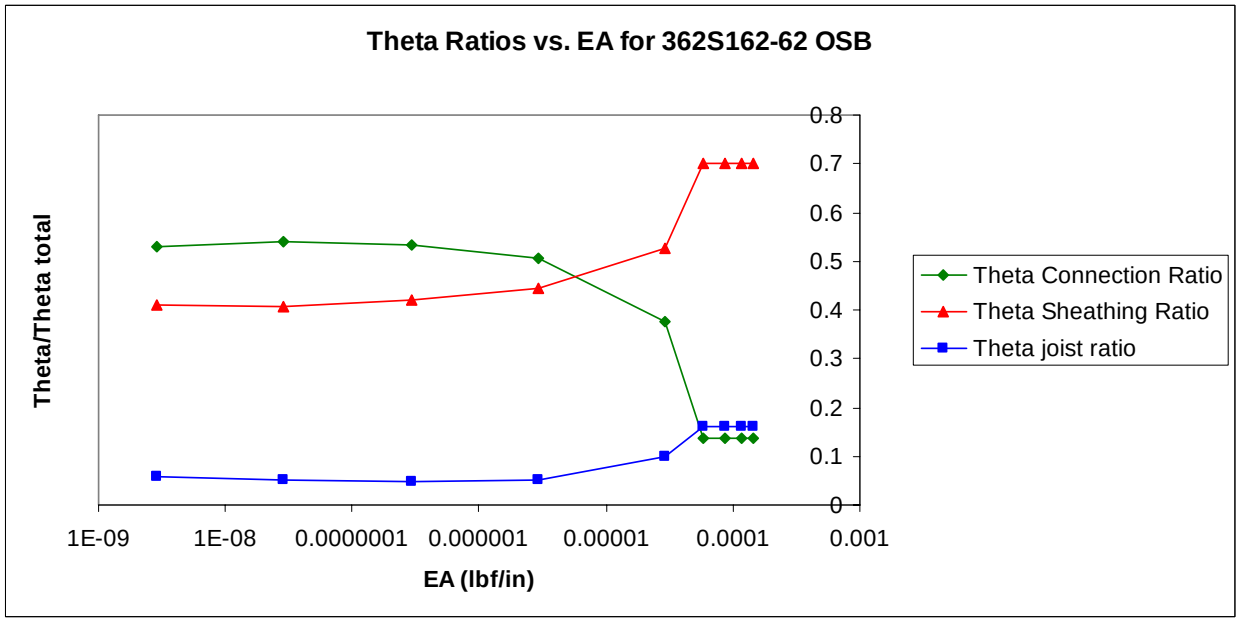

Figure 43 Plot of Mastan output of decomposed rotational contributions For a 362S162-62 Joist with OSB Sheathing

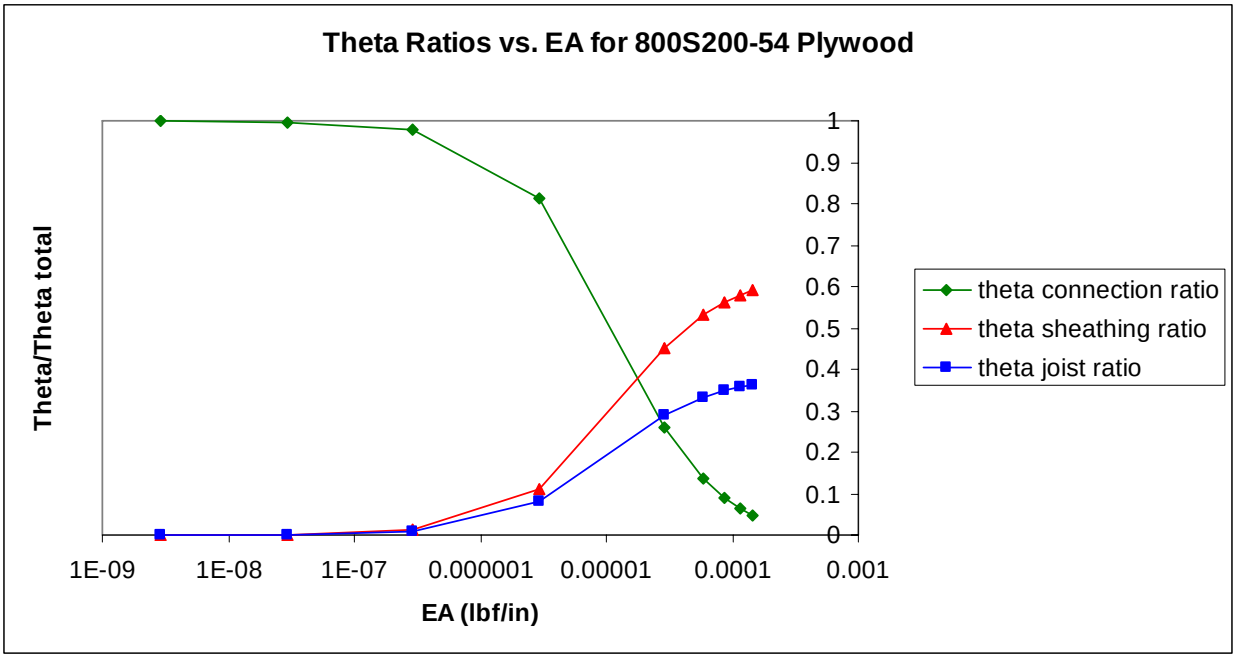

Figure 44 Plot of Mastan output of decomposed rotational contributions For a 800S200-54 Joist with Plywood Sheathing

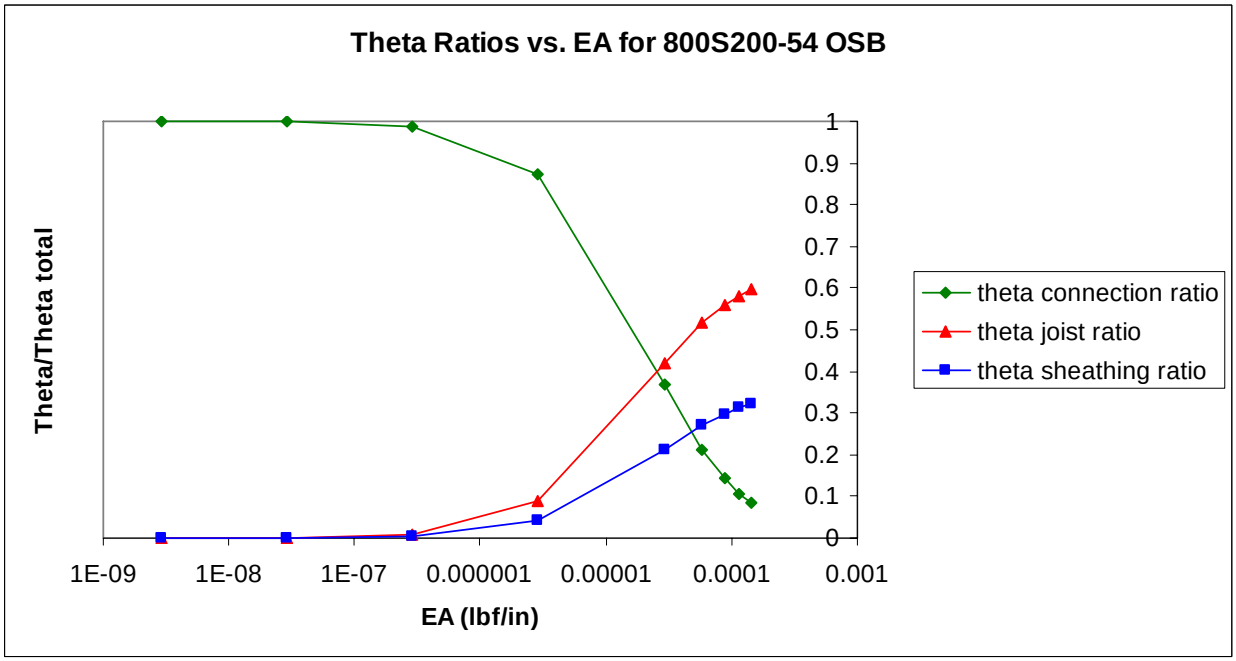

Figure 45 Plot of Mastan output of decomposed rotational contributions For a 800S200-54 Joist with OSB Sheathing

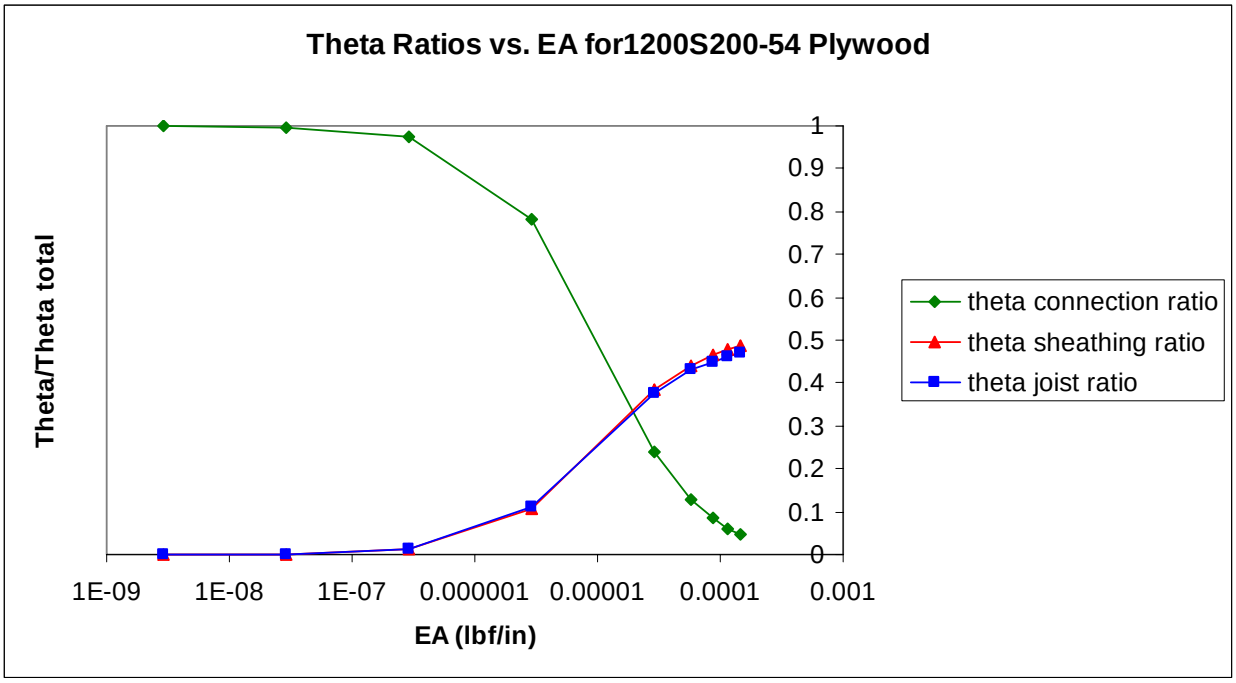

Figure 46 Plot of Mastan output of decomposed rotational contributions For a 1200S200-54 Joist with Plywood Sheathing

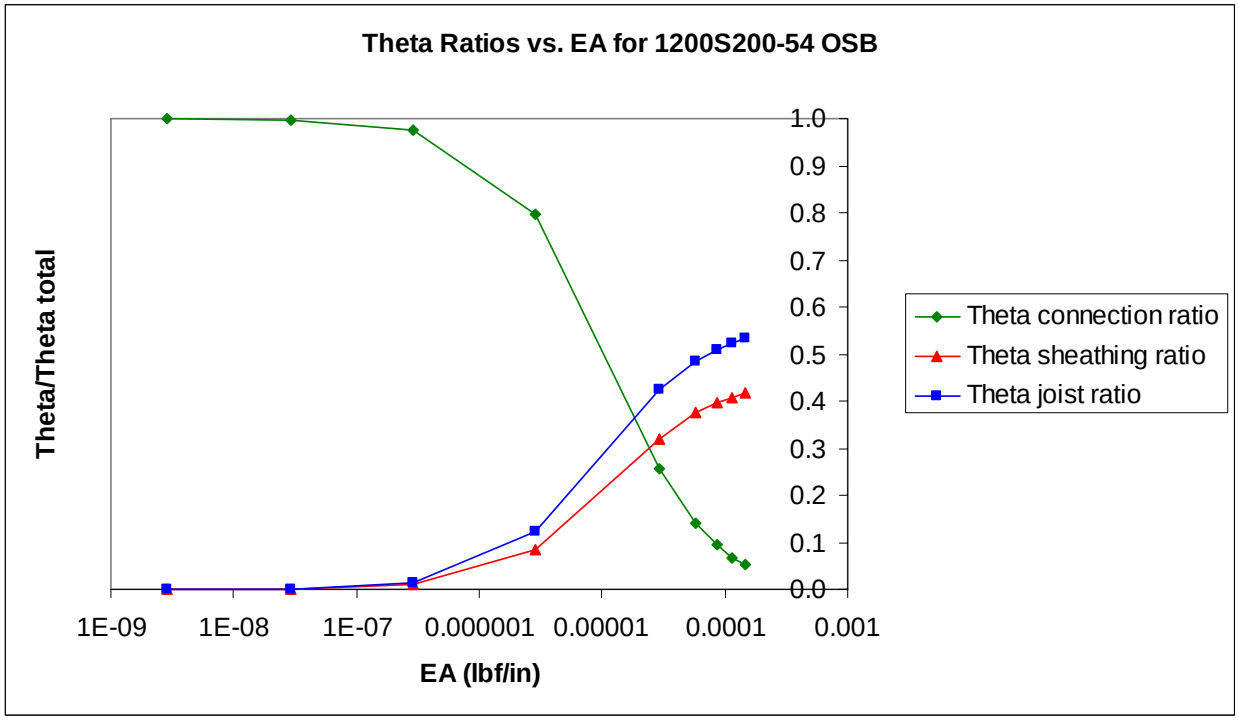

Figure 47 Plot of Mastan output of decomposed rotational contributions For a 1200S200-54 Joist with OSB Sheathing

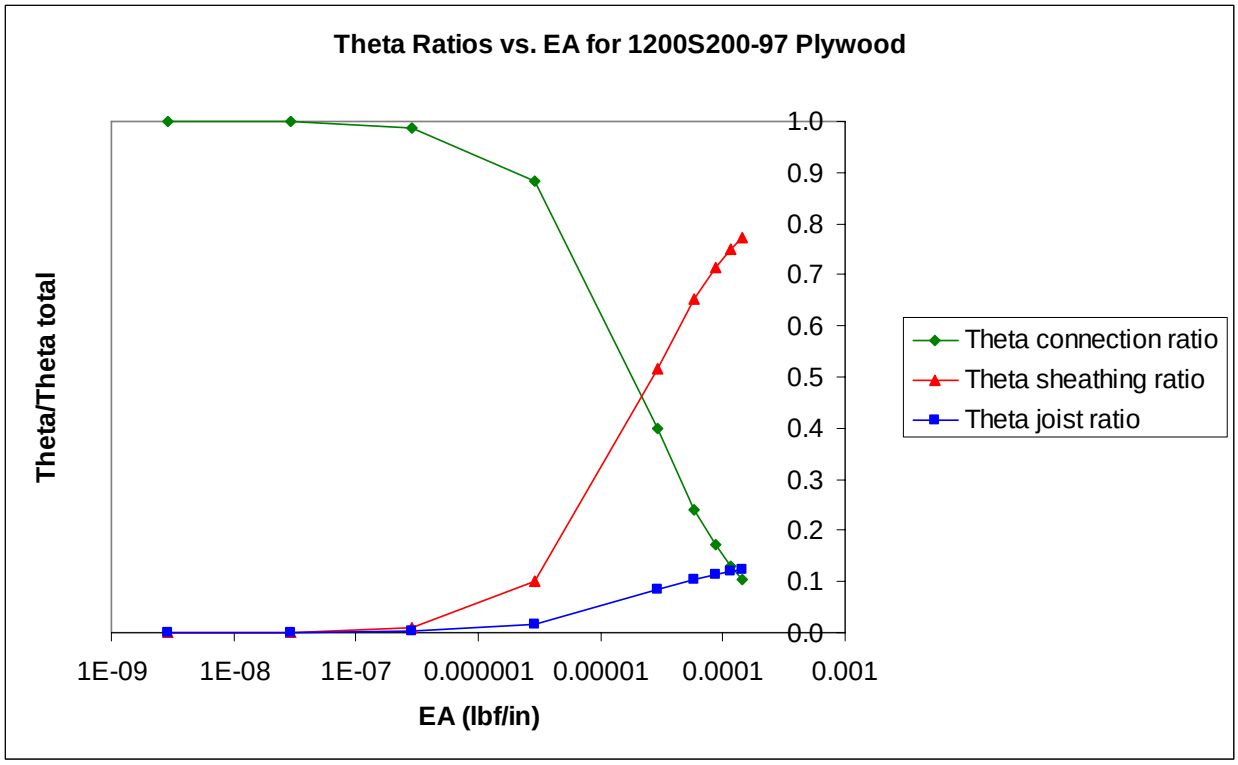

Figure 48 Plot of Mastan output of decomposed rotational contributions For a 1200S200-97 Joist with Plywood Sheathing

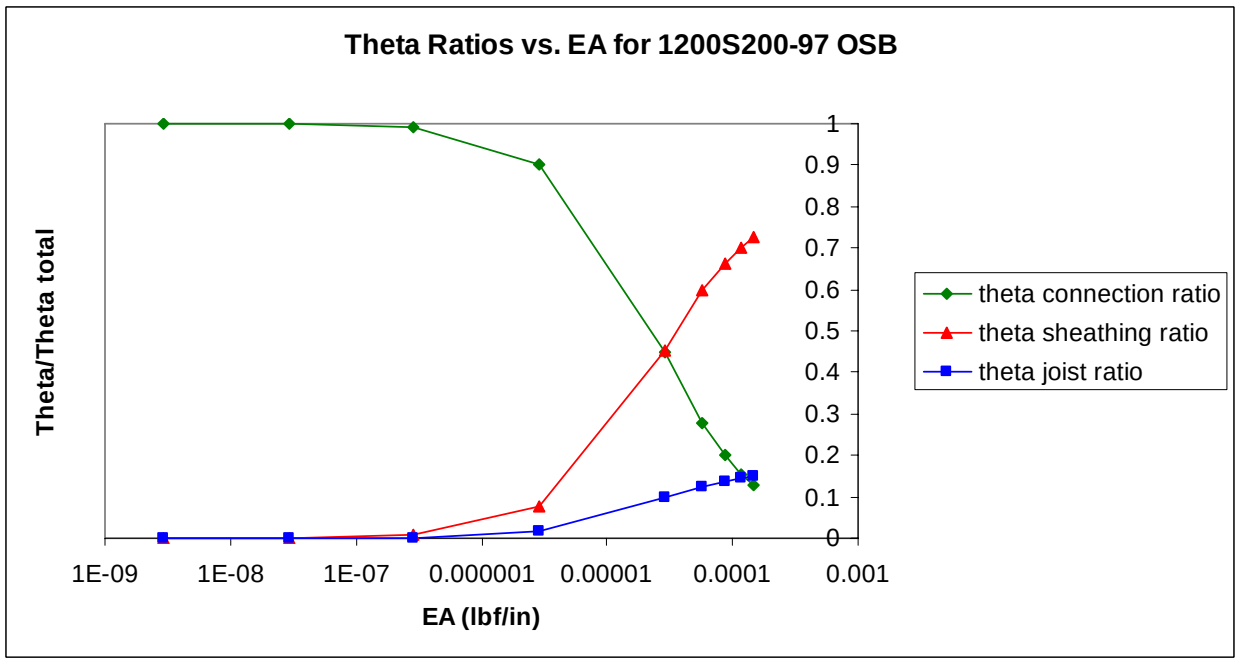

Figure 49 Plot of Mastan output of decomposed rotational contributions For a 1200S200-97 Joist with OSB Sheathing

Table 4 Summary of Rotational Stiffness Contributions with Flexible Fastener

Setup Modeled	Flexible Fastener Sheathing Ratio	Flexible Fastener Connection Ratio	Flexible Fastener Joist Ratio
362S162-33 Plywood	.36	.50	.14
362S162-33 OSB	.29	.44	.27
362S162-68 Plywood	.42	.57	.01
362S162-68 OSB	.41	.53	.06
1200S200-54 Plywood	.00	1.00	.00
1200S200-54 OSB	.00	1.00	.00
1200S200-97 Plywood	.00	1.00	.00
1200S200-97 OSB	.00	1.00	.00
800S200-54 Plywood	.00	1.00	.00
800S200-54 OSB	.00	1.00	.00

Table 5 Summary of Rotational Stiffness Contributions with Rigid Fastener

Setup Modeled	Rigid Fastener Sheathing Ratio	Rigid Fastener Connection Ratio	Rigid Fastener Joist Ratio
362S162-33 Plywood	.55	.01	.44
362S162-33 OSB	.37	.02	.61
362S162-68 Plywood	.84	.05	.11
362S162-68 OSB	.70	.14	.16
1200S200-54 Plywood	.49	.05	.46
1200S200-54 OSB	.42	.05	.53
1200S200-97 Plywood	.77	.11	.12
1200S200-97 OSB	.72	.13	.15
800S200-54 Plywood	.59	.05	.36
800S200-54 OSB	.32	.08	.60

From these plots, it is evident that joist bending effects are more significant than previously assumed. Examination of Figure 40 and Figure 41 for tests with a 362S162-33 joist indicate substantial permanent joist bending effects comprising 14 and 27% of total rotation exists even with a flexible fastener (as shown in Table 4). This may be attributed to 362S162-33 joists having the least resistance to joist bending among all joists tested by virtue of having the smallest moment of inertia. Figures Figure 46 and Figure 47 in conjunction with Table 5 show tests with 1200S200-54 joists have significant joist bending effects comprising 46 and 53% of total rotation with a rigid fastener. This is consistent with expectations accompanying a larger moment arm and a moderate moment of inertia resulting in greater web bending deformations.

These Mastan results further highlight the need to remove significant joist bending effects within reported $k_{\phi c2}$ values for more efficient design. However, while Mastan allows for a simple analysis of general joist bending significance within different sheathing and joist combinations, it cannot be used to quantify joist bending effects within individual tests which require modeling out of plane and fastener spacing effects. With this in mind, it is important to realize the plots display joist bending effects within a continuum as maximum joist bending effects within each plot assume a rigid fastener with infinite axial stiffness which is not the case within individual tests. The Mastan results instead support the need for the development of an approach in ABAQUS to quantify joist bending within individual tests as joist bending has the potential to be very depending on axial stiffness.

In order to quantify joist bending within individual tests, the experimental setup and fasteners are modeled in ABAQUS using the approach described in section 2.2.1. Each test has sheathing with unique properties, specific fastener spacing, and fasteners with individual axial stiffness values. Sheathing used in an experiment can be modeled by solving for the sheathing modulus of elasticity, E_w, by relating sheathing bending stiffness to rotational stiffness values through the equation, $E_w I_w / L = k_{\phi_w}$. Fastener behavior unique to each test is simulated in ABAQUS by calculating fastener axial spring stiffness inputs using experimental connection stiffness values, $k_{\phi c2}$, through a derived relationship shown in section 4.1.2.

With this approach, ABAQUS model connection stiffness values based on fastener rotation alone, $k_{\phi c}$, contains experimental joist bending effects, θ_s. Total rotation within ABAQUS therefore includes sheathing rotation, θ_w, isolated experimental connection rotation, θ_c, experimental joist bending, θ_s, and additional ABAQUS joist bending, θ_{s2}. ABAQUS Joist bending ratios for each individual test within these definitions are equivalent to θ_{s2}/θ_2, the fraction of total ABAQUS rotation composed of ABAQUS joist bending. Experimental joist bending can therefore be quantified as the product of ABAQUS joist bending ratio and experimental connection stiffness, or $\theta_s = \frac{\theta_{s2}\theta_{c2}}{\theta_2}$.

The only difficulty involved in calculating θ_s using ABAQUS output is the need for θ_{s2}, ABAQUS joist bending. ABAQUS joist bending using ABAQUS output can be decomposed however by removing sheathing rotation, θ_w, and ABAQUS connection rotation, $\theta_{c,abaqus}$ from total ABAQUS rotation, θ_2 leading to $\theta_{s2} = \theta_2 - \theta_{c,abaqus} - \theta_w$. Using ABAQUS nonlinear elastic analysis output, total rotation is still found using the expression $\theta_2 = \tan^{-1}(\Delta_v/h_o)$ while sheathing rotation is found using the expression $\theta_w = 2\Delta_h/L$, consistent with the approach used in the original AISI report. This is different from the Mastan approach in which nodal rotations are

used in rotation decomposition due to ABAQUS calculating rotational displacements using a local axis when global rotational displacements are needed.

Similarly, connection rotational stiffness within ABAQUS, $\theta_{c,abaqus}$, based on Figure 1 is derived as $\theta_{c,abaqus} = \Delta/.5b_o$ using spring elongation, Δ, within ABAQUS instead of using ABAQUS nodal rotations. This approach is used with the ABAQUS joist bending ratio, $\theta_{s2}/\ \theta_2$, to quantify experimental joist bending effects, and decompose experimental connection stiffness values, $k_{\phi c}$, for additional tests to explore the effects of fastener spacing on rotational stiffness as reported in section 5.2.

4 RELATIONSHIP BETWEEN FASTENER AXIAL STIFFNESS AND FASTENER ROTATIONAL STIFFNESS

It is known there is a positive correlation between axial stiffness and connection rotational stiffness. By deriving a relationship between fastener axial stiffness and connection rotational stiffness using moment equilibrium, fastener properties using fastener axial spring stiffness inputs within ABAQUS can be accurately modeled based on experimental connection rotational stiffness values. With an accurate quantification of fastener axial stiffness values, decomposition of experimental moment couple effects, accurate quantification of joist bending effects, and analysis of experimental failure modes observed can occur.

4.1 Attempts to quantify axial forces in fastener for failure mode prediction

As observed during experimental testing, axial pullout was one potential failure mode for fasteners. It can therefore be beneficial to designers to have a quantified value of the axial force necessary to induce axial pullout failure, or have some idea of fastener pullout deformation limits. By modeling the experimental setup in Mastan, generalized exploration of fastener axial stiffness in relation to fastener connection stiffness response is conducted. In doing so, it can be assessed whether a range of fastener axial spring stiffness values that can yield accurate experimental fastener stiffness response exists for sheathing and joists tested. An extension of this approach in ABAQUS can then be used for exploration of fastener axial stiffness and forces within individual tests by iteration of axial spring stiffness inputs until convergence of model rotational stiffness responses to individual experimental rotational stiffness responses.

4.1.1 Effects of varying axial stiffness on rotational stiffness in Mastan

The same truss based Mastan model depicted in Figure 3 and used to explore joist bending effects in Section 3.3 can be used to compare model rotational stiffness response to experimental rotational stiffness response. With the same nodal decomposition shown in Figure 4, connection and sheathing rotation can be taken from nodal rotation outputs after Mastan analysis. To form a basis of support for ABAQUS exploration, connection rotation within Mastan must be assumed to contain both experiment connection rotation and experiment joist bending effects as explained in section 3.3. Therefore convergence between Mastan model response and experimental model response can be judged as when the ratio of $k_{\phi c}/\ k_{\phi w}$ found using Mastan output is equivalent to the ratio of $k_{\phi c},/\ k_{\phi w}$ using experimental output. Values of $k_{\phi c}/\ k_{\phi w}$ within Mastan can be found by relating k_ϕ to beam mechanics using $k_\phi = M/\theta$.

With this relationship, $k_{\phi c}/\ k_{\phi w}$ found using Mastan output is simply the ratio of $\theta_w/\ \theta_c$ and can be calculated with Mastan output nodal rotations for θ_w and θ_c. By varying the area of the fasteners or

fastener axial stiffness as a result within these Mastan models and achieving convergence, this approach provides support that an equivalent axial stiffness in relation to experimental results can be found via modeling. Plots of these findings using models with joists coupled with OSB and plywood sheathing are shown in Figure 50.

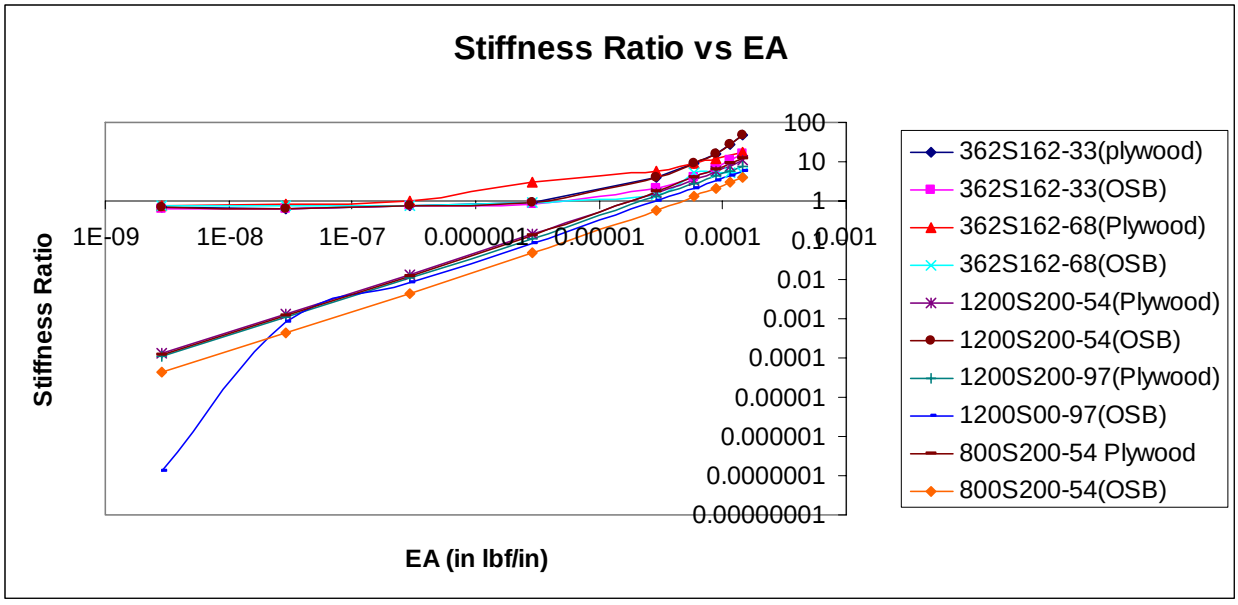

Figure 50 Plot of stiffness ratio: $k_{\phi c2}/ k_{\phi w}$ using Mastan Analysis

Table 6 Summary Table of Connection Rotational Stiffness To Sheathing Rotational Stiffness Ratios

$k_{\Phi c2}/k_{\Phi w}$ Ratios																
Sheathing -->	Plywood					OSB						Gypsum				
Cantilever (L) -->	12"				24"	12"				24"		12"		24"		
Fastener # -->	6		10		6	6				6	10	6	10	6	10	
Fastener Spacing -->	6"	12"	6"	12"	12"	3"	6"	12"	24"	12"	12"	12"	12"	12"	12"	
362S162-33		1.04										0.34				
362S162-68		1.41										0.45				
800S200-54	1.85	1.94		1.92	6.46					0.96	0.76	0.35	0.27	0.71	0.72	
800S250-54		1.19		1.89		*0.89*	*0.89*	*0.65*	*0.32*							
800S200-97			4.67	2.82							1.42		0.38			
1200S200-54		1.29								0.96						
1200S200-97				2.62							1.60					

By comparing the table of experimental $k_{\phi c}$,/ $k_{\phi w}$ output values presented in Table 6 and the plots presented in Figure 50, convergence of experimental $k_{\phi c}$,/ k_{ϕ} ratio values and Mastan $k_{\phi c}$/ $k_{\phi w}$ ratio values can be achieved for the joist and OSB or plywood sheathing combinations modeled in Mastan. Due to different joist bearing representation, out of plane effects, and fastener spacing effects however, it is not sufficient to equate and use Mastan axial stiffness values at convergence as fastener axial spring input values within ABAQUS. Rather, this approach using Mastan allows for a quick gauge of the likelihood of accurately modeling fastener behavior in ABAQUS while also yielding a potential range of axial stiffness values which may foster this result.

When this Mastan approach finds convergence for a given sheathing and fastener combination as it has in this case, it provides support for undertaking the longer iterative process necessary for testing individual axial stiffness value inputs within ABAQUS. Instead of using Mastan axial stiffness inputs corresponding to ratio convergence, ABAQUS axial stiffness inputs are predicted using moment equilibrium and experimental connection rotational stiffness values while tailored to individual experimental tests through tributary widths based on fastener spacing.

4.1.2 Effects of varying axial stiffness on rotational stiffness in ABAQUS

The key to accurately modeling experimental tests using ABAQUS models depicted within section 2.2.1 is the axial stiffness of the Spring2 elements representing fasteners. When the correct ABAQUS axial stiffness is chosen, connection rotational stiffness response within ABAQUS should mirror experimentally determined response. The difficulty therefore lies in determining the correct magnitude of fastener axial spring stiffness within ABAQUS.

The concept of modeling the fastener as a spring and joist bearing as a roller was presented in the original report and is reproduced in Figure 51. This approximation is what drove the use of ABAQUS Spring2 elements in modeling the fastener as it allows for calculation of fastener forces and connection rotation through analysis of spring deformation and spring stiffness alone. Contact modeling was similarly used due to the valid definition of contact between sheathing and joist as frictionless sliding, equivalent to a roller effect.

While this mechanics approximation supports the present modeling approach used in ABAQUS to simulate observed moment couple effects, it also proves useful in relating axial stiffness to experimental connection rotational stiffness values. Through using simple statics, it provides a way to calculate relatively accurate fastener axial spring stiffness values for Spring2 elements used in ABAQUS.

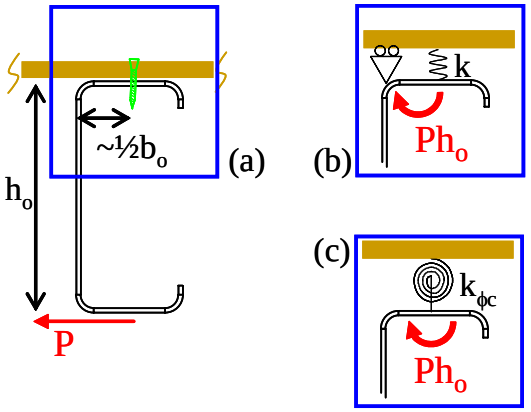

Figure 51 Mechanics approximation of fastener and joist bending effects
Source: Experiments on Rotational Restraint of Sheathing, 2007

By conducting moment equilibrium at the web flange intersection where joist bearing occurs, an expression for axial stiffness can be obtained by realizing axial spring deformation as $\Delta=.5\theta_c b_o$ and Moment at the fastener as $M=k_{axial}\,\Delta b_o/2$. By equating this Moment due to the fastener, $M=k_{axial}\,\Delta b_o/2$, to moment resulting from connection rotation, $M= k_{\phi c}\theta_c$, an expression for axial stiffness, k_{axial}, can be found as $k_{axial}=4\,k_{\phi c}/b_o^2$.

By using experimental connection rotational stiffness values, $k_{\phi c2}$, in place of $k_{\phi c}$, this expression can be used to calculate an initial input value for ABAQUS fastener axial spring stiffness. By using $k_{\phi c2}$ instead of of $k_{\phi c}$ within the expression however, experimental joist bending effects are included and must be taken into account as discussed in section 3.3. As a result, connection rotational stiffness within ABAQUS, $k_{\phi c,\ abaqus}$, should behave similarly to $k_{\phi c2}$ when k_{axial} is used.

With this acknowledgement, the ABAQUS models can be considered to be accurate in simulating experimental tests when $k_{\phi c,abaqus}$ calculated within the linear region using ABAQUS displacement output is equivalent to experimental $k_{\phi c2}$ values. The same linear regression methods used to extract $k_{\phi c2}$ are applied towards ABAQUS output to obtain $k_{\phi c,abaqus}$ by calculating moment at the fastener from ABAQUS output as $M=Ph_o$ within the linear regime.

Using spring element deformation and the Figure 51 delineation of moment couple effects, global connection rotation using small angle approximations is quantified as $\theta_c= 2\Delta/b_o$ and is used to decompose connection rotational stiffness in ABAQUS, $k_{\phi c,abaqus}=M/\theta_c$ for comparison to experimental $k_{\phi c2}$ values. This calculation of θ_c is what governs decomposition and quantification of joist bending effects as described in section 3.3.

As $k_{\phi c2}$ experimental values are calculated per unit width, axial spring stiffness input values are modified by a factor equivalent to fastener tributary width to further include fastener spacing effects. Through iteration, initial ABAQUS axial spring inputs calculated from the k_{axial} expression is refined until ABAQUS connection response exactly matches experimental connection response resulting in a correct axial spring stiffness value.

Through comparison of predicted k_{axial} from the expression and actual k_{axial} values after convergence for additional tests described in 5.2, the expression provides an extremely accurate prediction of k_{axial} values that is minimally conservative. Due to this, the expression is also accurate in estimating pull out failure axial forces within fasteners with the expression, $Force=2M/b_o$, by dividing moment at the fastener by the axial force moment arm, $b_o/2$.

While this approach can be used to estimate fastener axial forces at failure far into the nonlinear range due to the availability of experiment Moment values, it cannot be used to estimate fastener axial stiffness and fastener deformation limits at failure due to the lack of experimental $k_{\phi c}$ values at failure. However, an estimation of fastener axial stiffness at failure and corresponding fastener deformation can be made using ABAQUS by finding the combination of k_{axial} and Δ values based on ABAQUS output with a product magnitude that is equivalent to fastener axial force found using the expression $Force=2M/b_0$.

5 ADDITIONAL EXPERIMENTS

Seven new cantilevered sub-flooring models using the same procedure outlined in the original report (Schafer 2007) were created and tested in two separate series to measure any beneficial effects of reducing fastener spacing on $k_{\phi c2}$. All seven tests were conducted with 15/32 in. thick OSB sheathing at 12 in. cantilevered and 800S200-54 joists with 8 inch joist depth, .054 in. joist thickness, and 2 in. flange width. The seven tests were carried out with #6 fasteners at 3, 6, 12, and 24 in. o.c. fastener spacing respectively.

5.1 Failure modes observed

During testing, axial pull out failure shown in Figure 52 was observed at 6, 12, and 24 in. fastener o.c. spacing with increasing severity with greater fastener spacing. At 12 in. o.c. fastener spacing, there was complete axial pullout failure of all five fasteners, while at 6 in. and 24 in. fastener o.c. spacing, there was axial pullout failure observed at the right side. A new failure mode was also observed at 3 in. o.c. fastener spacing as OSB sheathing fracture as shown in Figure 53 was witnessed at the end of the test without axial pullout suggesting a decrease in fastener spacing may be beneficial in controlling for pullout failure.

Figure 52 Fastener Pullout Failure

Figure 53 Sheathing Fracture Failure

5.2 Measured and modeled effects of fastener spacing on fastener rotational stiffness

Based on reported $k_{\phi c2}$ values from the initial AISI report (Schafer 2007), there were ostensible benefits towards decreasing fastener spacing resulting in increases in $k_{\phi c2}$ although the relationship was not definite. From the first series of four additional tests shown in Table 7 and Table 8 including results from the first report, there is a sizable measured increase in $k_{\phi c2}$ due to decreased fastener spacing as $k_{\phi c2}$ increased from 99, to 182, to 275 lbf-in./in./rad when fastener spacing is decreased from 24 in., to 12 in., and 6 in. o.c. respectively.

The relationship between fastener spacing and $k_{\phi c2}$ for the first series of additional tests is unclear however as a decrease in fastener spacing to 3 in. o.c. leads to a decreased $k_{\phi c2}$ value of 209 lbf-in/in./rad. from 6 in. o.c. fastener spacing. Connection rotational stiffness values from this first series test with 3 in. o.c. fastener spacing seem suspect as the sheathing rotational stiffness value

of 235 lbf-in/in./rad. was significantly different from sheathing rotational stiffness values reported from the other three tests.

While the sheathing failure mode witnessed in this test should still be documented as a new possible failure mode associated with sub-flooring, failure mode axial forces cannot be calculated using the flawed data. It is believed displacement transducers low on voltage were used to measure sheathing displacement resulting in sheathing and connection rotational stiffness values that are inaccurate. A subsequent second series of tests was conducted as a follow up to further verify the relationship between connection rotational stiffness and fastener spacing.

Table 7 Summary of Experimental Connection Rotational Stiffness Results (numbers in italics indicate new tests conducted as part of this report)

$k_{\phi c2}$ (lbf-in./in./rad)															
Sheathing -->	Plywood					OSB						Gypsum			
Cantilever (L) -->	12"				24"	12"				24"		12"		24"	
Fastener # -->	6		10		6	6				6	10	6	10	6	10
Fastener Spacing -->	6"	12"	6"	12"	12"	3"	6"	12"	24"	12"	12"	12"	12"	12"	12"
362S162-33		81										100			
362S162-68		102										137			
800S200-54	116	109		97	137	*209*	*275*	*207*	*99*	113	77	103	77	91	99
800S200-54 Retest						*246*	*198*	*102*							
800S250-54		116		124											
800S200-97			269	167							159		144		
1200S200-54		78								85					
1200S200-97				215							195				

Table 8 Summary of Experimental Sheathing Connection Rotational Stiffness Results (numbers in italics indicate new tests conducted as part of this report)

$k_{\phi w}$ (lbf-in./in./rad)															
Sheathing -->	Plywood					OSB						Gypsum			
Cantilever (L) -->	12"				24"	12"				24"		12"		24"	
Fastener # -->	6		10		6	6				6	10	6	10	6	10
Fastener Spacing -->	6"	12"	6"	12"	12"	3"	6"	12"	24"	12"	12"	12"	12"	12"	12"
362S162-33		78										295			
362S162-68		72										300			
800S200-54	63	56		51	21	*235*	*310*	*309*	*307*	117	101	295	285	128	138
800S200-54 Retest						*342*	*336*	*358*							
800S250-54		98		66											
800S200-97			58	59							112		378		
1200S200-54		60								89					
1200S200-97				82							122				

With a constant power supply installed for the displacement transducers, the second series of additional tests with different OSB sheathing were performed for 6, 12, and 24 in. o.c. fastener spacing with results shown as retests in Table 7 and Table 8. These connection rotational stiffness values from the second series of additional testing in conjunction with the previous fastener spacing tests indicate a linear relationship is possible for fastener spacing as low as 6 inches. Connection rotational stiffness in the second series of additional tests nearly doubles from 102 to 198 lbf-in./in./rad when fastener spacing is halved from 12 inches to 6 inches o.c. (in contrast to

the first series of additional tests). At 3 inches, the beneficial linear relationship between tighter fastener spacing and increased connection rotational stiffness breaks down as connection rotational stiffness does not double but instead increases from 198 to 246 lbf-in./in./rad when fastener spacing is halved from 6 inches to 3 inches o.c.. It would seem that the stiffness derives from a tributary width of the joist and sheathing, and at 3 in. this tributary width begins to overlap.

Modeling the seven additional experimental tests after retesting with ABAQUS was done through iteration of k_{axial} fastener stiffness inputs until ABAQUS $k_{\phi c}$ response matched experimental $k_{\phi c2}$ response as shown from plots from Figure 54 to Figure 59. The ABAQUS results support the proposed beneficial relationship between closer fastener spacing with higher $k_{\phi c}$ values for tighter fastener spacing after removal of ABAQUS and experimental joist bending effects as summarized in Table 9 and Table 11 for series 1 and 2 tests respectively.

While connection rotational stiffness did not necessarily double for all fastener spacing tested, increases due to tighter fastener spacing are still significant. It is also interesting to observe the limit on linear connection rotational stiffness increase occurs at a fastener spacing of 6 inches which may be attributed to inhibitive fastener tributary width effects.

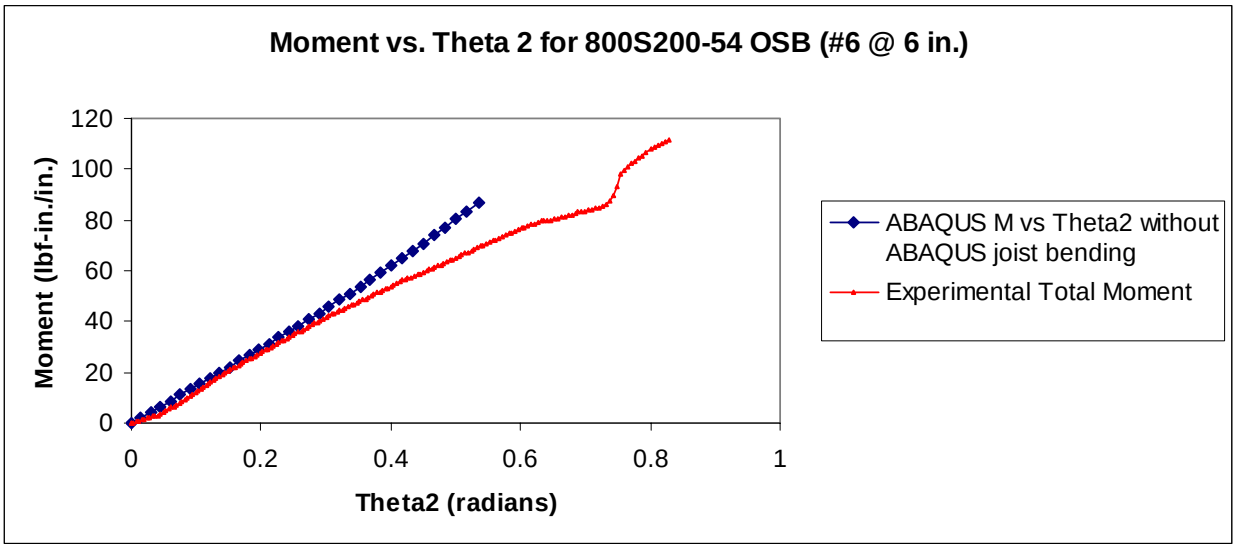

Figure 54 Series 1 Comparative Plot of ABAQUS and Experimental Moment vs. Theta response for 6 inch o.c. fastener spacing after decomposition and removal of ABAQUS joist bending

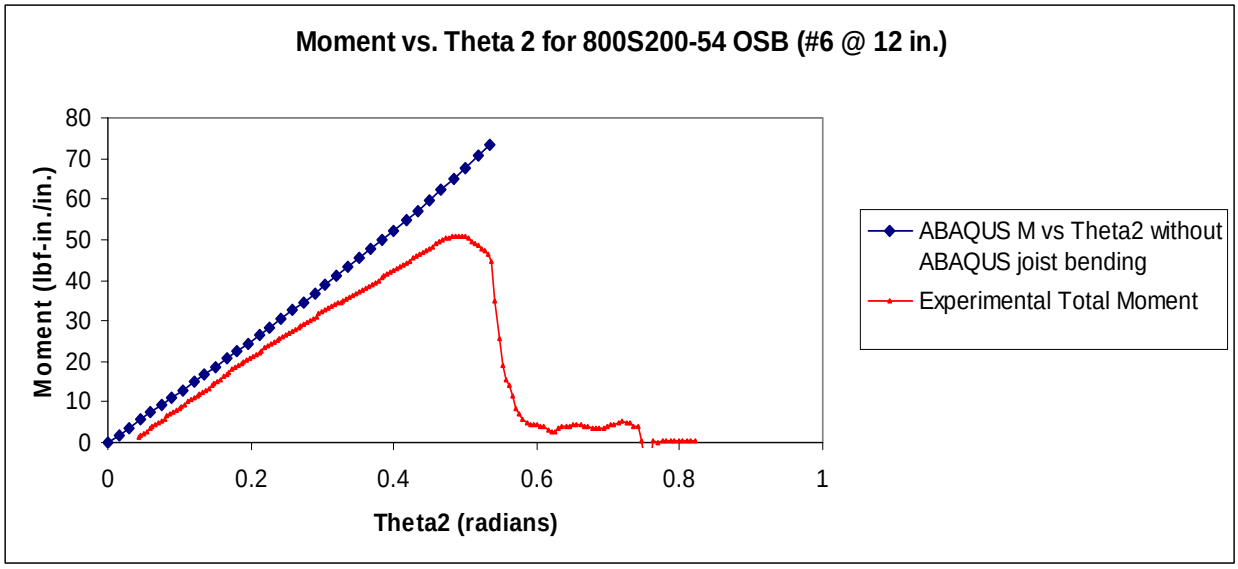

Figure 55 Series 1 Comparative Plot of ABAQUS and Experimental Moment vs. Theta response for 12 inch o.c. fastener spacing after decomposition and removal of ABAQUS joist bending

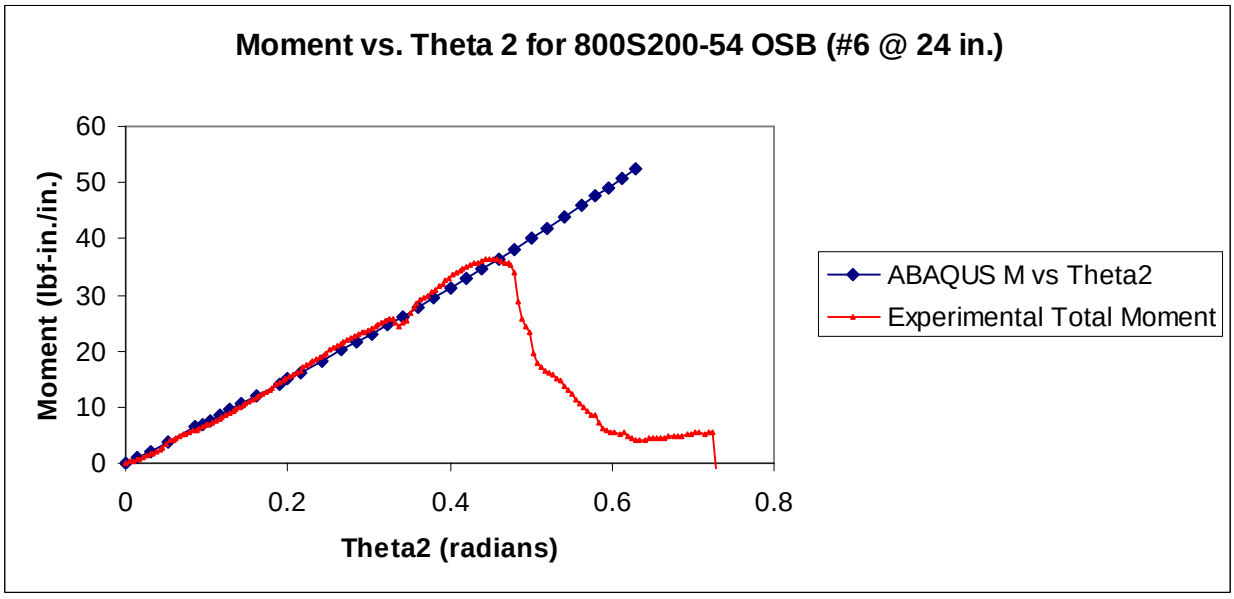

Figure 56 Series 1 Comparative Plot of ABAQUS and Experimental Moment vs. Theta response for 24 inch o.c. fastener spacing after decomposition and removal of ABAQUS joist bending

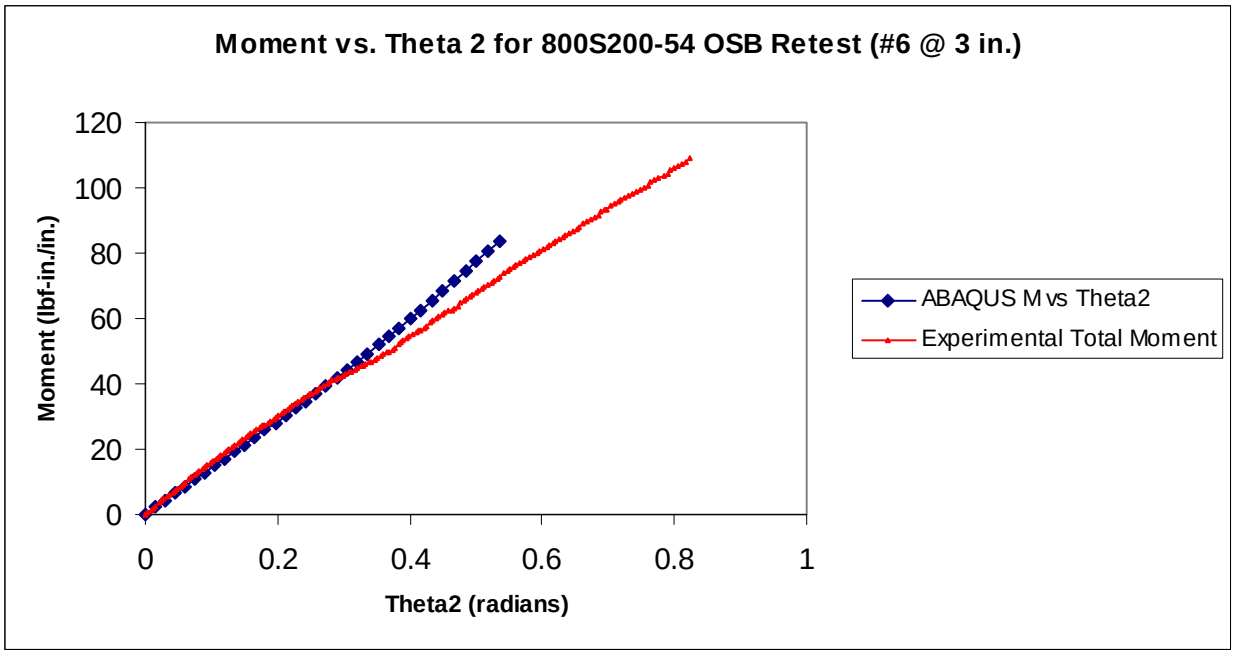

Figure 57 Series 2 Comparative Plot of ABAQUS and Experimental Moment vs. Theta response for 3 inch o.c. fastener spacing after decomposition and removal of ABAQUS joist bending

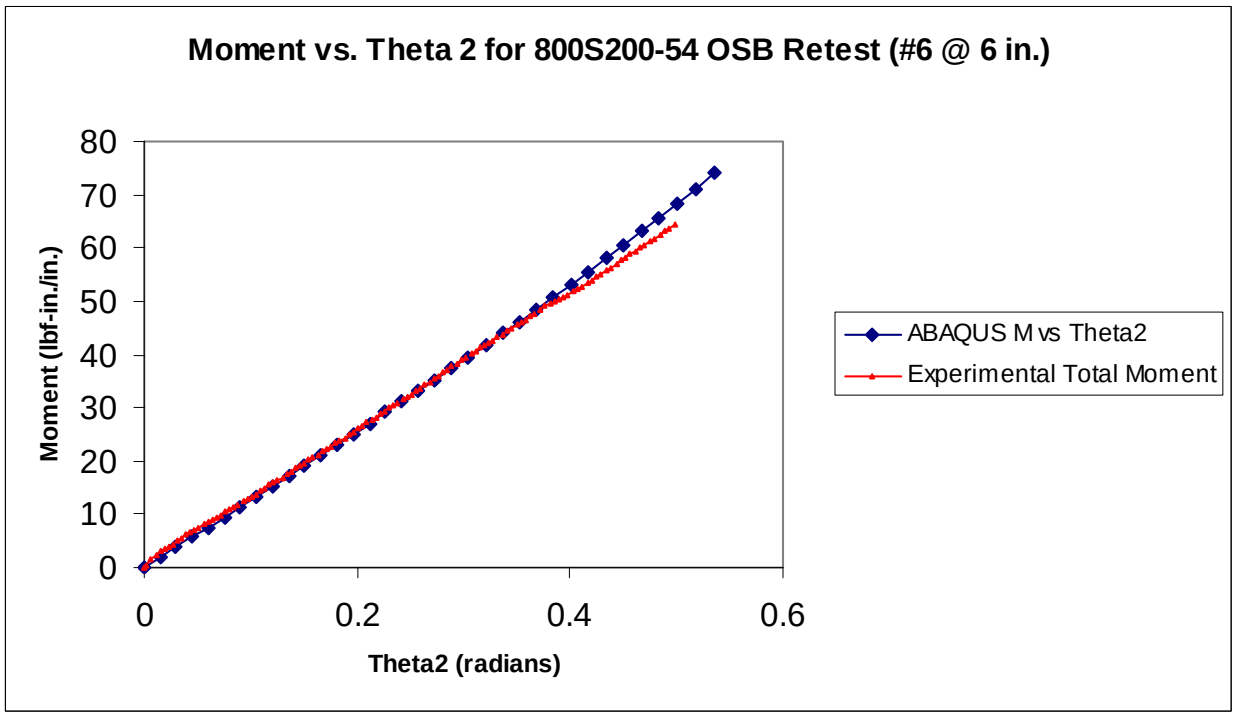

Figure 58 Series 2 Comparative Plot of ABAQUS and Experimental Moment vs. Theta response for 6 inch o.c. fastener spacing after decomposition and removal of ABAQUS joist bending

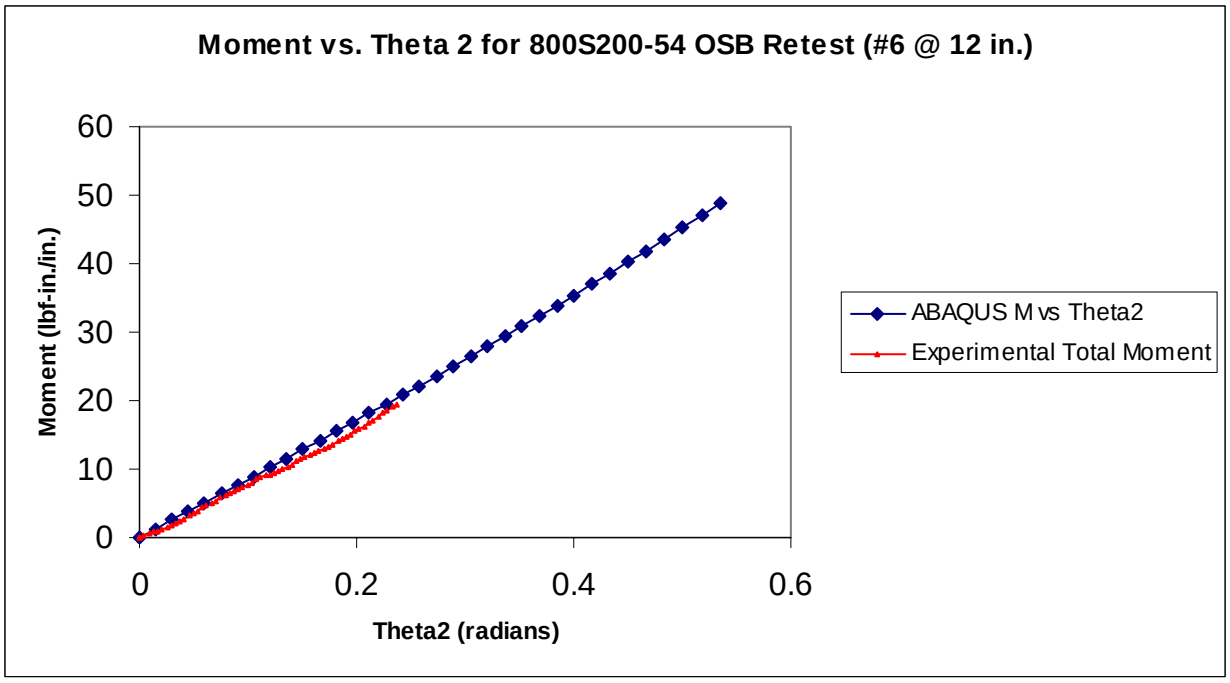

Figure 59 Series 2 Comparative Plot of ABAQUS and Experimental Moment vs. Theta response for 12 inch o.c. fastener spacing after decomposition and removal of ABAQUS joist bending

By removing sheathing and connection rotations approximated using sheathing deflection and axial spring elongation from total rotation in ABAQUS, joist bending effects due to ABAQUS are decomposed according to section 3.3 and shown in Table 9. These analysis results further support the reliability of the ABAQUS decomposition approach presented as the quantified joist bending effects are shown to be significant and in agreement with Mastan analysis of joist bending for an 800S200-54 joist with OSB sheathing from section 3.3. Due to the inclusion of these significant joist bending effects in experimental determinations of connection rotational stiffness, $k_{\phi c2}$, it is not surprising connection rotational stiffness values due to fastener rotation alone, $k_{\phi c}$, are substantially higher when added flexibility in connection stiffness calculations due to joist bending is removed.

With high agreement between calculated k_{axial} fastener axial stiffness inputs and refined k_{axial} values using iteration shown in Table 9 and Table 11, the validity of the mechanics approximation of moment couple effects in Figure 51, is supported by the ABAQUS decomposition analysis results. Keeping this in mind, a substantial increase in k_{axial} results from removing joist bending effects as expected due to the mechanics model showing k_{axial} to be directly proportional to $k_{\phi c}$. The same model can also be used to assess failure modes as failure moment can be decomposed into axial force using half the flange depth as the moment arm as reported in Table 10 and Table 12 for axial pullout failures for series 1 and 2 tests respectively,

Further decomposition of fastener axial pullout failure forces into axial stiffness and fastener deformation at failure using the mechanics model is difficult however as the model is used to derive k_{axial} in relation to $k_{\phi c}$ within the linear range while failure occurs in the nonlinear regime. ABAQUS can be used to decompose fastener axial pullout forces at failure, as reported in Table 10 and Table 12, by finding the product of k_{axial} and fastener deformation equivalent to the decomposed failure

pullout force using the mechanics model. However, as ABAQUS cannot be used to model fastener failure, this proves to be only an approximation of fastener behavior after nonlinear deformation.

ABAQUS analysis output of these additional tests promotes the use of tighter faster spacing up to between 6 and 3 inches o.c. before substantial benefits in connection rotational stiffness start decreasing. And while decomposed connection rotational stiffness values are less conservative than previously calculated values with joist bending effects, these new higher rotational stiffness values suggest there is substantial additional capacity within fastener connections available.

Table 9 Series 1 Testing ABAQUS Decomposition Summary

Fastener Spacing (in inches)	Calculated k_{axial} (in kips/in.)	k_{axial} through iteration per fastener (in kips/in.)	k_{axial} without joist bending per fastener (in kips/in.)	ABAQUS Joist Bending Ratio, θ_{s2}/θ_2	Experimental $k_{\phi c2}$ (in lbf-in./in./rad.)	Experimental $k_{\phi c}$ without joist bending (in lbf-in./in./rad.)
24	2.376	2.592	3.53	.414	99	147.10
12	2.484	2.94	4.43	.496	207	369.43
6	1.650	1.88	2.82	.492	275	469.56

Table 10 Series 1 Testing ABAQUS Fastener Axial Pullout Failure Decomposition

Fastener Spacing (in inches)	Axial Pullout Failure Moment (in lbf-inch/inch)	ABAQUS Predicted Failure k_{axial} per fastener (in kips/in.)	Spring Deformation At Axial Pullout, Δ (in inches)
24	36.31	3.94	.231
12	50.88	4.75	.137
6	111.57	3.67	.194

Table 11 Series 2 Testing ABAQUS Decomposition Summary

Fastener Spacing (in inches)	Calculated k_{axial} (in kips/in.)	k_{axial} through iteration per fastener (in kips/in.)	k_{axial} without joist bending per fastener (in kips/in.)	ABAQUS Joist Bending Ratio, θ_{s2}/θ_2	Experimental $k_{\phi c2}$ (in lbf-in./in./rad.)	Experimental $k_{\phi c}$ without joist bending (in lbf-in./in./rad.)
12	1.22	1.32	1.53	.341	102	127.71
6	1.19	1.23	1.71	.436	198	284.28
3	.74	.78	1.22	.469	246	406.2

Table 12 Series 2 Testing ABAQUS Fastener Axial Pullout Failure Decomposition

Fastener Spacing (in inches)	Axial Pullout Failure Moment (in lbf-inch/inch)	ABAQUS Predicted Failure k_{axial} per fastener (in kips/in.)	Spring Deformation At Axial Pullout, Δ (in inches)
12	19.49	1.59	.16
6	64.29	1.91	.21
3	108.89	4.52	.125

5.3 Summary sheets of additional experiments

The following summary sheets have been compiled for additional testing conducted to explore fastener spacing effects on connection rotational stiffness. Included is the flawed test with fasters at 3 inch o.c. spacing identified as 9-PL-12-6-03-01. While the sheathing deflection was incorrectly measured, a new sheathing fracture failure mode was exhibited during this test imparting some importance on the P-Δ curve presented. Summary sheets of the second series of additional tests to rectify flawed data in the first 3 inch o.c. fastener spacing test are also included with retest written in the notes section. The same procedure used to construct specimens and to analyze test data to extract connection rotational stiffness values in the first study is followed in this set of additional tests.

Test Date: 1/28/08 Initials: YG
Joist ID: 800S200-54
Assembly ID: 9-PL-12-6-03-01
Sheathing: OSB, L = 12 in.
Fastener: #6 @ 3 in.
datafile: 9-800S200_54_01

Notes:
.125” initial warp measured.
1 of 5 screws overdriven.
Failure of OSB sheathing observed towards end of test resulting in fracture of sheathing.

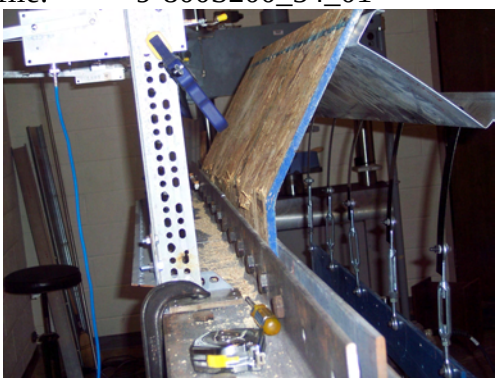

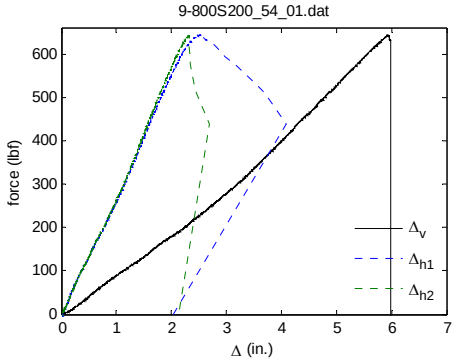

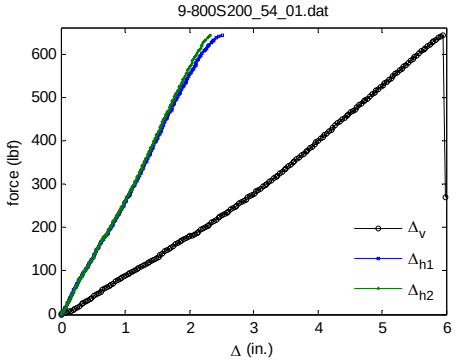

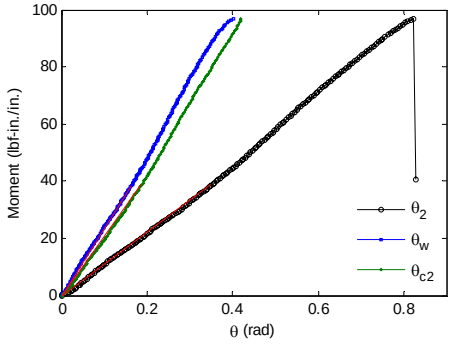

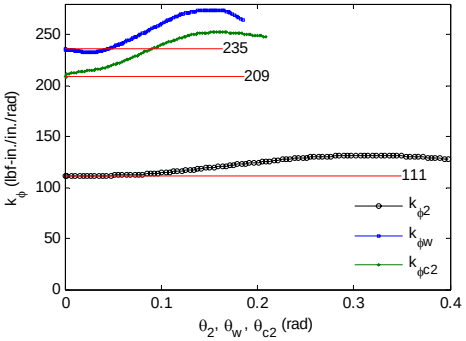

Test Date: 1/28/08 Initials: YG
Joist ID: 800S200-54
Assembly ID: 9-OSB-12-6-6-01
Sheathing: OSB, L = 12 in.
Fastener: #6 @ 6 in.
datafile: 9-800S200_54_02

Notes:
0" initial warp was measured.
0 of 5 screws overdriven.
Faster pullout emanating from right side occurred towards end of test.

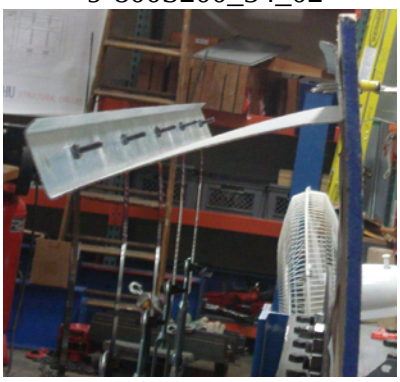

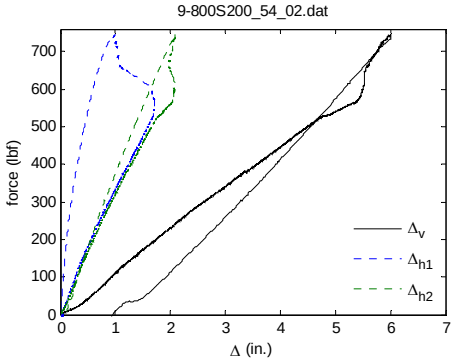

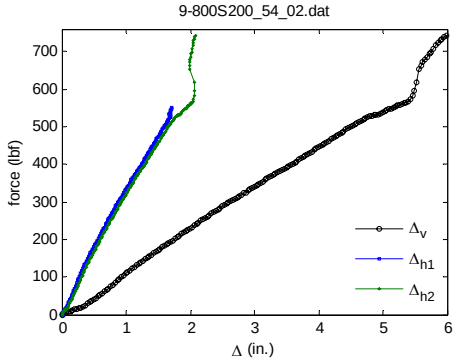

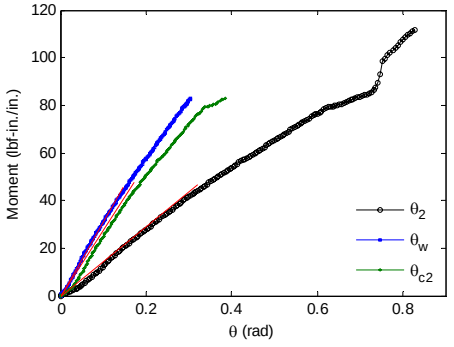

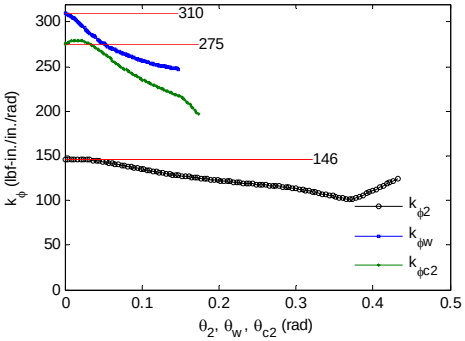

Test Date: 2/02/08 Initials: YG
Joist ID: 800S200-54
Assembly ID: 9-OSB-12-6-12-01
Sheathing: OSB, L = 12 in.
Fastener: #6 @ 12 in.
datafile: 9-800S200_54_03

Notes:
Initial warp was .125".
1 of 5 screws over driven.
Complete axial pullout of screws observed.

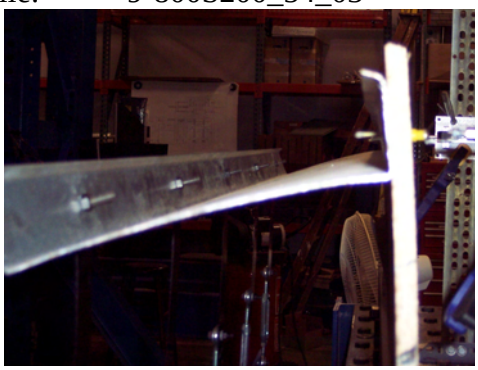

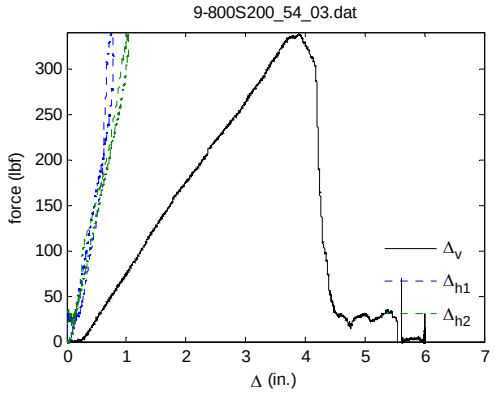

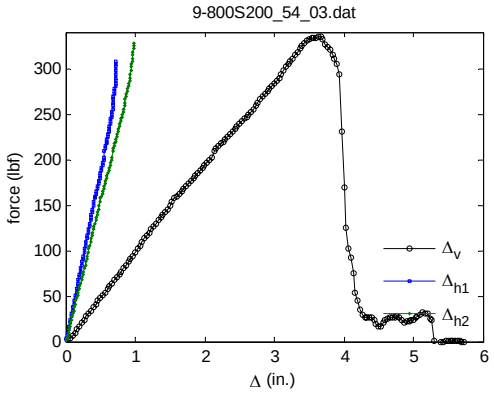

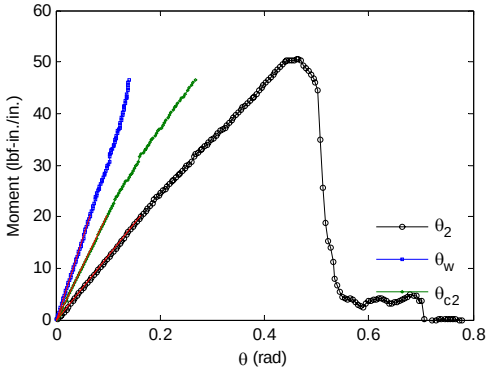

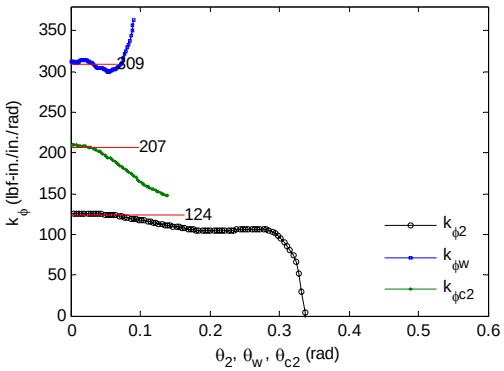

Test Date: 6/17/08 Initials: YG
Joist ID: 800S200-54
Assembly ID: 9-OSB-12-6-3-01
Sheathing: OSB, L = 12 in.
Fastener: #6 @ 3 in.
datafile: 9-800S200_54_01

Notes:
.125” initial warp measured.
1 of 5 screws overdriven.
Failure of OSB sheathing observed towards end of test resulting in fracture of sheathing.

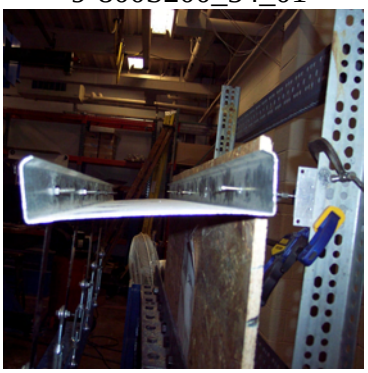

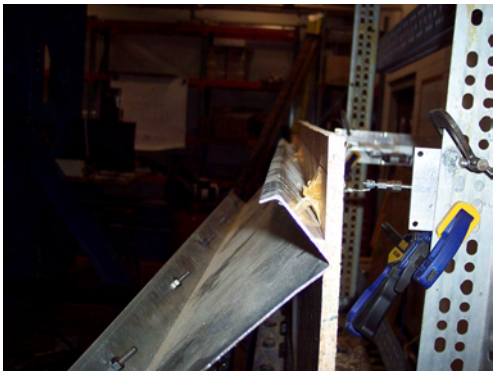

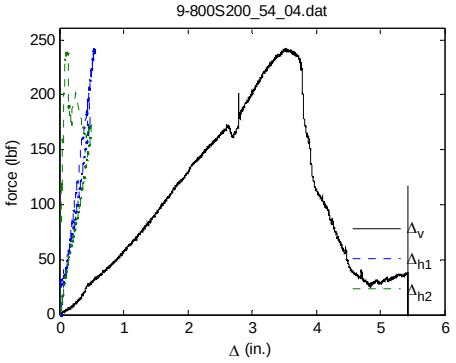

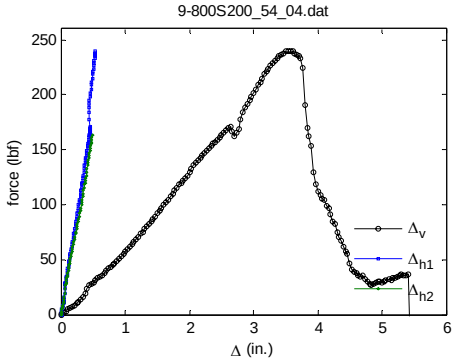

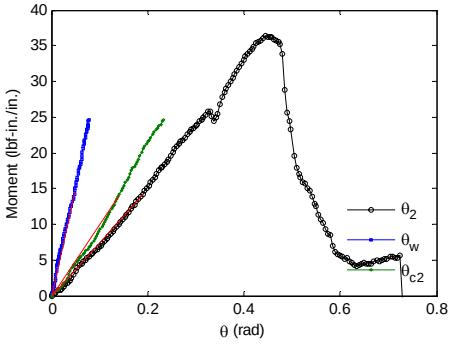

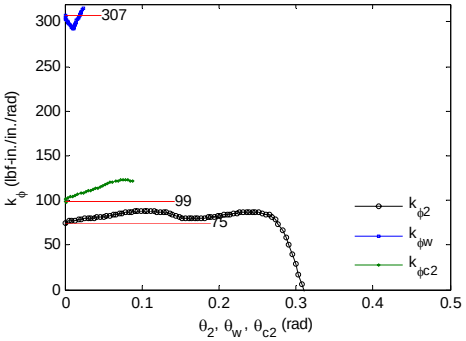

Test Date: 2/02/08 Initials: YG
Joist ID: 800S200-54
Assembly ID: 12-OSB-12-6-3-01
Sheathing: OSB, L = 12 in.
Fastener: #6 @ 3 in.
datafile: newtest3

Notes:
Retest of 3 inch o.c. fastener spacing
Initial warp was .125".
3 of 17 screws over driven.

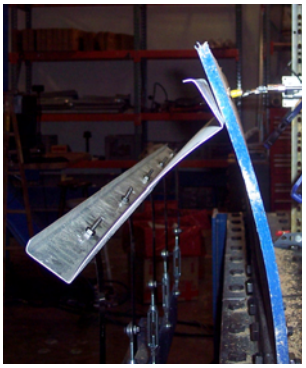

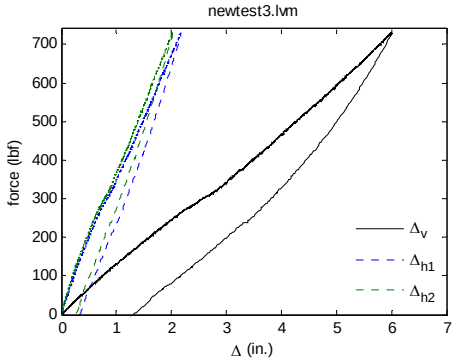

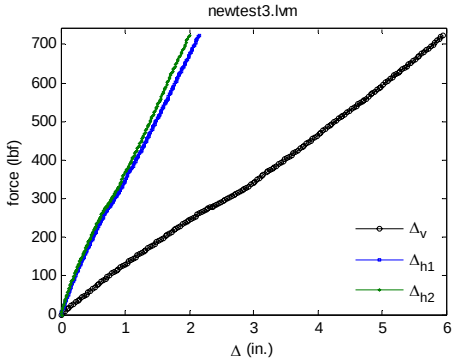

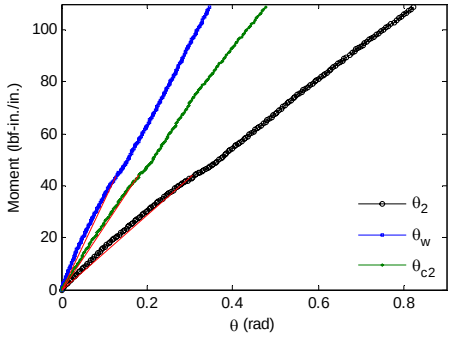

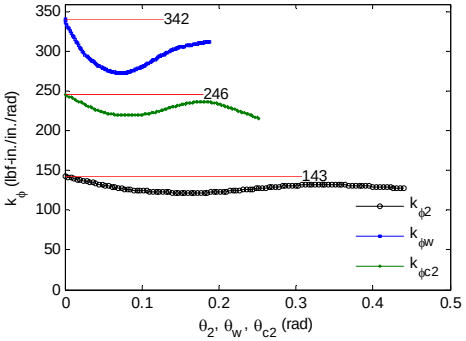

Test Date: 2/02/08 Initials: YG
Joist ID: 800S200-54
Assembly ID: 12-OSB-12-6-6-01
Sheathing: OSB, L = 12 in.
Fastener: #6 @ 6 in.
datafile: newtest6

Notes:
Retest of 6 inch o.c. fastener spacing
Initial warp was 0".
2 of 9 screws over driven.
Significant fastener axial pullout observed at 4 inches.

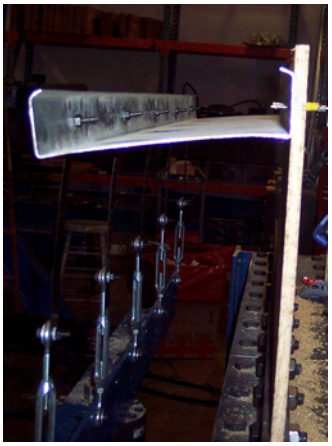

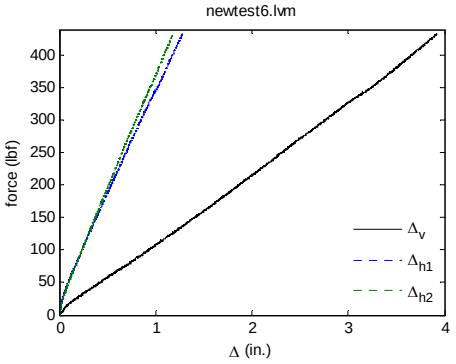

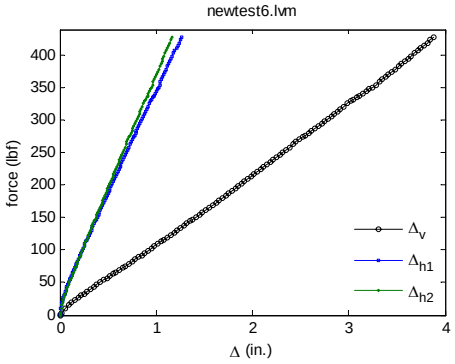

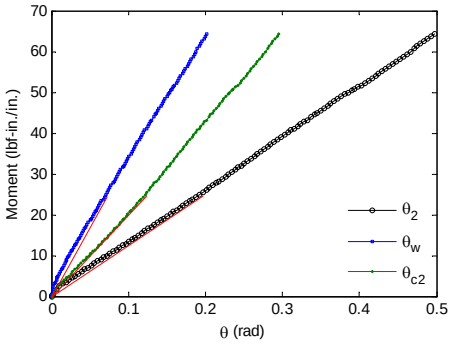

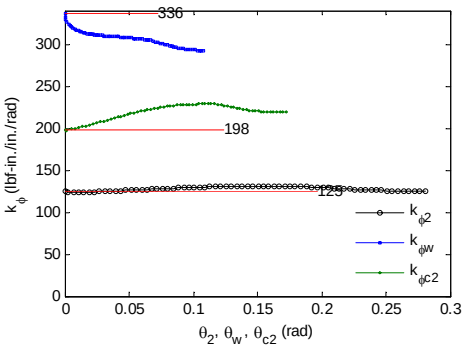

Test Date: 2/02/08 Initials: YG
Joist ID: 800S200-54
Assembly ID: 12-OSB-12-6-12-01
Sheathing: OSB, L = 12 in.
Fastener: #6 @ 12 in.
datafile: newtest12

Notes:
Retest of 12 inch o.c. fastener spacing
Initial warp was .125".
0 of 5 screws over driven.
Early fastener axial pullout observed at 2 inches.

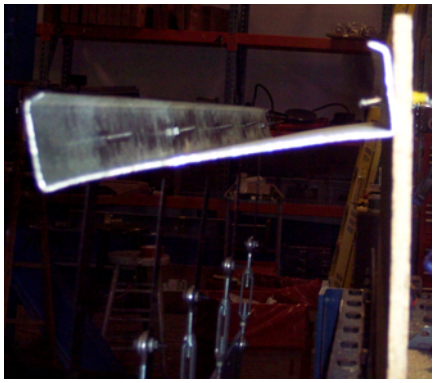

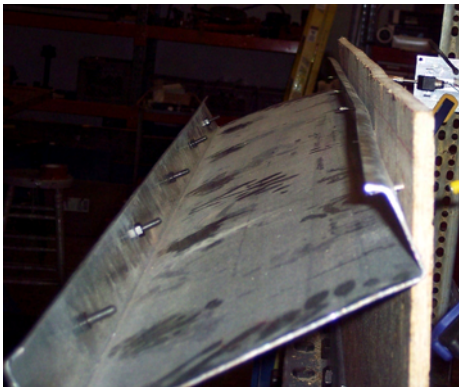

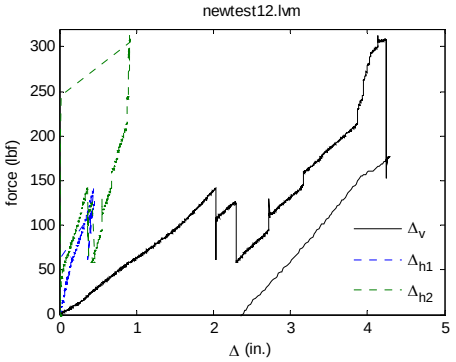

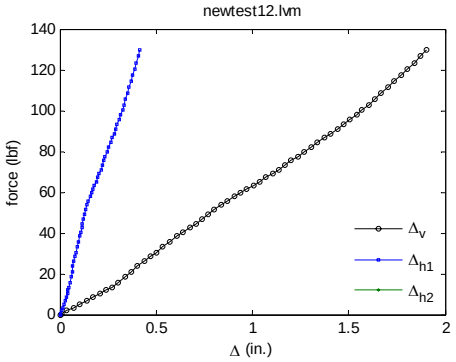

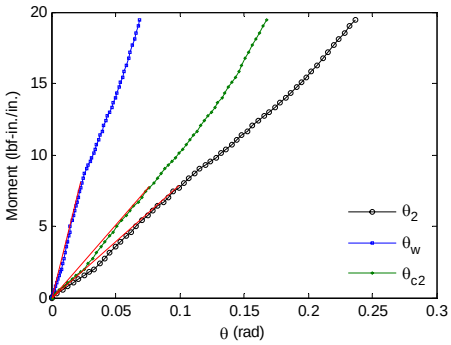

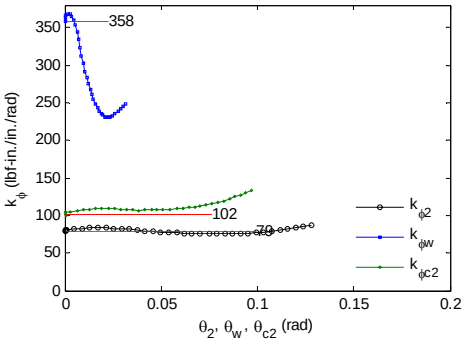

6 MODELING CONSTRUCTION FLAWS

A concern with the implementation of these connection stiffness values in design is the impact of construction flaws. Inherent during the construction and testing of specimens are the existence of two key flaws, overdriven and offset fasteners. By generating and deforming a mesh in ABAQUS shown in Figure 60with offsets and corresponding changes to fastener axial stiffness resulting from overdriven fasteners, the effects of flaws can be assessed as deviation from connection rotational stiffness values in idealized ABAQUS models with exact fastener spacing and no overdriven fasteners. The statistical study focuses on flaws involved in the construction of an 800S200-54 joist attached to OSB sheathing with 5 fasteners at 12 inch o.c. spacing.

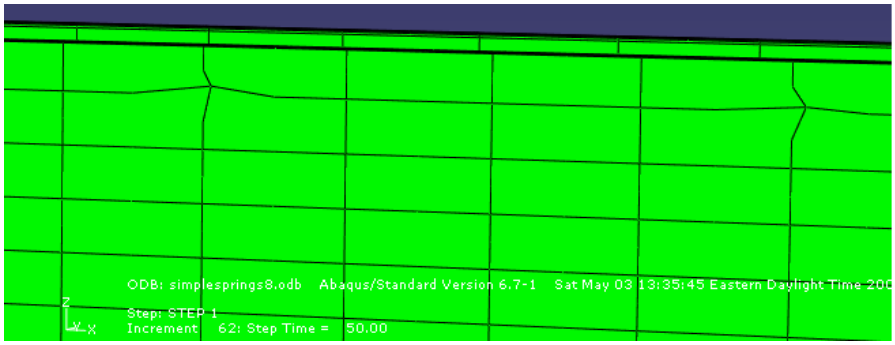

Figure 60 ABAQUS Mesh generated with offset fasteners

6.1 Background of study and construction flaws assessed

Among known construction flaws within a sub-flooring system, there is the potential for fastener offsets to occur resulting in differential spacing of fasteners from the center line along the length of each joist. There is also the potential for overdriven fasteners during construction rendering a reduction in the axial stiffness of fasteners. By conducting a parameter study using statistical analysis with ABAQUS models, resulting distribution properties of rotational stiffness as impacted by these construction flaws can be explored.

Due to the lack of a closed form solution for rotational stiffness, both a Monte Carlo and a Taylor series 2k+1 simulation approach is used to measure the distribution of rotational stiffness as a function of these construction flaws. Construction flaws are therefore applied to an idealized ABAQUS model of an 800S200-54 joist attached to OSB sheathing model with initially uniform 12 inch o.c. fastener spacing with fastener axial spring stiffness values calculated using the k_{axial} expression in section 4.1.2 based upon a $k_{\phi c}$ value from a previous experiment for the same setup.

For Monte Carlo simulation, random variables are generated in part using data from previous laboratory experiments and measurements. Offsets are applied to the initial ABAQUS model through using a polar coordinate approach with each fastener used as an origin as shown in Figure 61. An offset radius normal random variable is created for each fastener with a mean assumed to be 50% of the allowable radius and a standard deviation assumed to be 20% of the allowable radius. This allowable radius is determined as the lesser of half an S9R5 shell element length or width at the joist flange location to maintain aspect ratios and prevent excessive element deformation.

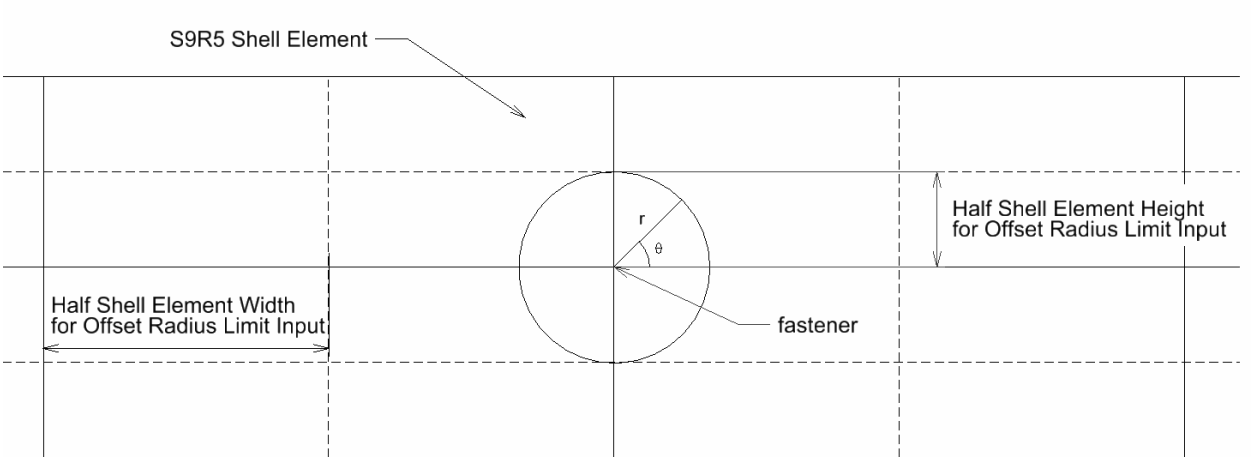

Figure 61 Local polar coordinate system at each fastener used to create offsets

An offset theta normal random variable between 0 and 2π is also generated with a mean of 45 degrees and a standard deviation of 30 degrees. The two random variables, offset radius and offset theta, are applied to each fastener's local polar coordinate system to create offsets if the fastener is simulated to be offset for Monte Carlo simulation.

A similar approach is also taken for Monte Carlo simulation of overdriven fasteners. A lognormal random variable R representing axial stiffness reduction will be generated for each fastener with a mean of 30% reduction and a standard deviation of 10%. At each fastener, the experimentally measured axial stiffness is thereby reduced by R if the fastener is simulated to be overdriven.

To simulate whether a fastener is offset or overdriven within Monte Carlo simulation, two standard normal variables labeled as offset marker and overdriven marker are generated and used as markers. When offset marker results in a value of .1 or less corresponding to a probability of 53.8% based on previous experimental measurements of fastener offset frequency, the fastener will experience no offset with the offset radius set to 0 as a result. Similarly, when overdriven marker results in values of -.47 or less corresponding to a probability of 32.4% based on previous experimental measurements of overdriven fastener frequency, R is set to 0 reflecting no reduction in axial stiffness due to overdriven fasteners.

2k+1 simulation differs from Monte Carlo simulation in that each fastener is both offset by a calculated offset length and offset angle while also overdriven resulting in fastener axial stiffness reduced by a set amount all without markers generated to determine if a fastener is offset or overdriven. The offset length, offset angle and axial stiffness random variable reduction quantities in 2k+1 simulation are calculated instead using Monte Carlo random variables.

Within 2k+1 simulation, or = offset marker*offset radius is used to define the offset length while the variable oθ = offset marker*offset theta is used to define the offset angle. Finally, a third variable RM = overdriven marker*R is defined as the amount of 2k+1 fastener axial stiffness reduction. Offsets are still applied with the polar coordinate approach in 2k+1 but with or and oθ and without markers.

However, certain ABAQUS model input variables inherent to the materials and experimental setup such as the modulus of elasticity of steel, sheathing, sheathing length, and joist cross sectional dimensions among others, are not interpreted as random variables. These variables are instead

assumed to be deterministic with values taken from the previous experimental test of an 800S200-54 joist with OSB sheathing.

Computationally intensive Monte Carlo simulation is performed with the generation of 100 ABAQUS models with construction flaws in place. After processing the models using a batched approach, distribution properties can be calculated through determination of the mean and standard deviation from the resulting output connection rotational stiffness values.

Less computationally intensive 2k+1 simulation is performed with the generation of 31 ABAQUS models with construction flaws. Through the same batched ABAQUS processing approach applied towards Monte Carlo simulation, output connection rotational stiffness values can be obtained and used to find distribution properties through calculation of the mean and standard deviation. Additionally, 2k+1 output is used to provide a Taylor series expansion of connection rotational stiffness providing a closed form solution to determine connection stiffness as a function of random variables used in 2k+1 simulation.

6.2 Results of parameter study and effects of flaws on design values.

Bias factors for Monte Carlo and 2k+1 simulation as reported in

Table 19 Monte Carlo Simulation Connection Rotational Stiffness Distribution Summary are calculated by dividing the mean value of connection rotational stiffness due to flaws by the connection stiffness value of an 800S20054 sub-flooring specimen with 12 in. o.c. fasteners without construction flaws. As both bias factors are close to 1, this suggests construction flaws due to overdriven and offset fasteners with distributions as assumed in this study have potentially small effects on connection rotational stiffness supporting the reliability of connection rotational stiffness values reported in the first study and this follow up study for use in design.

Also, as both the mean value yielded by Monte Carlo simulation and the one yielded by 2k+1 simulations are close; the less computationally intensive 2k+1 point estimate approach can be applied accurately in place of Monte Carlo simulations to continue exploration of the effects of connection rotational stiffness values due to construction flaws. The mean connection rotational stiffness yielded by the 2k+1 method, 63.569, is slightly lower than the initial connection rotational stiffness value without construction flaws, 66.02, resulting in sub-flooring designs that might be less conservative. However, it is unclear whether additional simulations using the Monte Carlo method would yield mean and standard deviation values of connection rotational stiffness that would converge towards the 2k+1 estimated values.

While no exact closed form solutions for connection rotational stiffness as a function of construction flaws exist, an approximate closed form solution provided using 2k+1 output is shown in the 2k+1 calculations summary section below. It is important to note however this approximation of connection rotational stiffness contains ABAQUS and experimental joist bending effects as do the mean connection rotational stiffness values reported using Monte Carlo and 2k+1 simulation for ease of reporting. Joist bending effects are not expected to vary significantly due to construction flaws however rendering the impact of construction flaws on connection rotational stiffness with joist bending effects removed as minimal.

It is acknowledged uncertainty exists regarding whether the 31 simulations performed in 2k+1 analysis are sufficient to decipher the true distribution properties of connection rotational stiffness as impacted by construction flaws. Regardless, the low coefficient of variance of .0538 for the study indicates repeated simulations of this study should yield close values supporting high reliability of

results. While uncommon, construction flaws do have the potential to be significant resulting in connection rotational stiffness values several standard deviations above or below the mean.

Table 13 Summary of Monte Carlo Random Variable Distribution Properties

Variable	Distribution Type	Mean	Standard Deviation
offset marker	Normal	0	1
offset radius	Normal	0.2429	0.0972
offset theta	Normal	0.785	0.524
overdriven marker	Normal	0	1
R	Lognormal	-1.2	0.325

Table 14 Summary of Random Variable Distribution Properties At Fastener 1 of 5

Variable	Mean	Standard Deviation
offset marker	.076	.919
offset radius	.146	.136
offset theta	.826	.454
Overdriven marker	.091	.90
R	.317	.121

Table 15 Summary of Random Variable Distribution Properties At Fastener 2 of 5

Variable	Mean	Standard Deviation
offset marker	-.034	1.047
offset radius	.112	.125
offset theta	.818	.434
Overdriven marker	-.187	.972
R	.319	.121

Table 16 Summary of Random Variable Distribution Properties At Fastener 3 of 5

Variable	Mean	Standard Deviation
offset marker	.063	1.011
offset radius	.106	.126
offset theta	.857	.476
Overdriven marker	-.033	1.073
R	.321	.121

Table 17 Summary of Random Variable Distribution Properties At Fastener 4 of 5

Variable	Mean	Standard Deviation
offset marker	.176	.902
offset radius	.150	.135
offset theta	.818	.519

Overdriven marker	.221	.953
R	.316	.110

Table 18 Summary of Random Variable Distribution Properties At Fastener 5 of 5

Variable	Mean	Standard Deviation
offset marker	-.044	1.035
offset radius	.110	.122
offset theta	.829	.434
Overdriven marker	.155	1.000
R	.307	.098

Table 19 Monte Carlo Simulation Connection Rotational Stiffness Distribution Summary

Variable	Mean Value from Simulations with flaws (in lbf-in./in./rad.)	Standard Deviation from Simulations with flaws (in lbf-in./in./rad.)	Initial value without offsets or overdriven fasteners from unaltered ABAQUS model (in lbf-in./in./rad.)	Bias Factor
Rotational Stiffness	65.970	4.703	66.020	.999

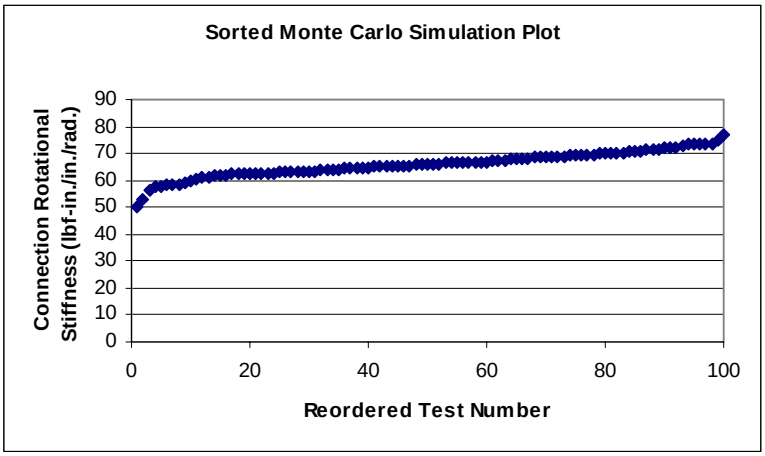

Figure 62 Sorted Plot of Monte Carlo Simulation Output

Table 20 2k+1 Variable Properties

Variable	Mean	Standard Deviation
RM	.1038	.1528
Or	.1308	.1312
oθ	.4565	.4909

2k+1 Summary Calculations:

Mean connection rotational stiffness = $\overline{Y} = y_o \prod_{i=1}^{K} (\frac{\overline{y}_i}{y_o}) = 64.5(.986) = 63.569$ lbf-in./in./rad.

Coefficient of variance = $V_y = \sqrt{\{\prod_{i=1}^{K} (1 + V_{y_i}{}^2)\} - 1} = .0538$

Standard deviation of performance function = $\sigma_Y = 3.419$ lbf-in./in./rad.

Theoretical rotational stiffness value from unaltered ABAQUS model = 66.020 lbf-in./in./rad.

Bias Factor = .963

Closed Form Approximation of Connection Rotational Stiffness Using 2k+1 output:

$$Y = f(RM_1, or_2, o\theta_3, RM_4, or_5, o\theta_6, RM_7, or_8, o\theta_9, RM_{10}, or_{11}, o\theta_{12}, RM_{13}, or_{14}, o\theta_{15})$$

$$\approx -6.87RM_1 - 7.49RM_4 - 7.33RM_7 - 6.87RM_{10} - 6.81RM_{13} - 3.81or_2 - 3.81or_5 - 3.81or_8 - 3.81or_{11} - 3.81or_{14} + 1.63o\theta_3 + 1.63o\theta_6 + .29o\theta_9 + 1.80o\theta_{12} + 1.71o\theta_{15} + 236.07$$

7 CONCLUSIONS

Two key effects: joist bearing and fastener axial pull out observed during experimental testing were modeled in Mastan and ABAQUS for this study. In Mastan frame analysis, sheathing rotation approximations found using beam mechanics are shown to be accurate even for plywood subject to large rotations, as shown in Figure 16Figure 17. Mastan models are also used to assess the impact of nonlinear P-Δ effects, existent within testing due to a changing moment arm and an eccentric axial load. The models show support for the present approach used in calculating moment using experimental data, i.e., $M=Ph_o$, in which P-Δ effects are de-emphasized and the moment arm is assumed to be a constant h_o, see Table 2 Summary of Moment Arm EffectsTable 3.

Experimental connection stiffness values include joist bending effects. Mastan is also used to explore the significance of joist bending as summarized in Table 5. The Mastan models show maximum joist bending contributions to rotation that are more significant than previously assumed, supporting the development of an approach for quantifying joist bending effects within individual tests using three dimensional models in ABAQUS.

Equivalent Spring2 elements and contact definition are used to facilitate fastener and joist bearing modeling within a shell element ABAQUS mesh. These ABAQUS models provide a novel approach towards rotational decomposition as connection rotation without joist bending, $k_{\phi c}$, can be isolated and quantified for individual tests as summarized in Table 9Table 11. The ABAQUS models also prove to be useful in assessing failure modes through quantification of axial stiffness and fastener deformation at failure as shown in Table 10 and Table 12.

Construction flaws and their impact on connection rotational stiffness were also considered and tested using Monte Carlo and 2k+1 simulation methods with the ABAQUS models. The results of the statistical parameter study carried out indicate the effects of construction flaws on reported connection rotational stiffness values are minor.

Additional experimentation was also carried out to verify if any beneficial effects of tighter fastener spacing on connection rotational stiffness existed. Results in Table 7 indicate a linear relationship may exist between connection rotational stiffness and fastener spacing up to 6 in. o.c. as observed in one case of an 8 in. deep joist with OSB sheathing.

Through the introduction of ABAQUS models which include out of plane and fastener spacing effects, this study suggests ABAQUS is a viable tool for accurately quantifying and removing joist bending effects for individual tests resulting in more efficient connection rotational stiffness values based on fastener rotation alone. This effectively bypasses the need for complex modifications to testing procedures including additional measurements taken at the fastener as suggested by the first report. By validating the mechanics approximation of moment couple effects, this study also presents a way to quantify axial forces at failure due to pull out in addition to k_{axial} and fastener deformation limits at failure which may prove to be beneficial for design.

Ultimately, the results of this follow-up study provide support for the reliability of connection rotational stiffness values reported in the first report through exploration of key assumptions made in calculating rotational stiffness values, and through a statistical analysis of construction flaw effects.

8 REFERENCES

Schafer, B.W., Sangree, R.H., Guan, Y. (2007). Experiments on Rotational Restraint of Sheathing: Final Report, American Iron and Steel Institute – Committee on Framing Standards, Washington, D.C.

American Iron and Steel Institute

1140 Connecticut Avenue, NW
Suite 705
Washington, DC 20036

www.steel.org

Steel Framing Alliance™
Steel. The Better Builder.

1201 15th Street, NW
Suite 320
Washington, DC 20005

www.steelframing.org

Research Report RP-08-2

The New Steel